A Hardware-in-the-Loop Test Platform for Planetary Rovers

by

Bonnie Yue

A thesis

presented to the University of Waterloo

in fulfillment of the

thesis requirement for the degree of

Master of Applied Science

in

Mechanical Engineering

Waterloo, Ontario, Canada, 2011

AUTHOR'S DECLARATION

I hereby declare that I am the sole author of this thesis. This is a true copy of the thesis, including any required final revisions, as accepted by my examiners.

I understand that my thesis may be made electronically available to the public.

Abstract

A Hardware-in-the-Loop (HIL) test platform for planetary rovers was designed, fabricated and tested in the present work. The ability for planetary rover designers and mission planners to estimate the rover's performance through software simulation is crucial. HIL testing can further the benefits of software simulations by allowing designers to incorporate hardware components within traditionally pure software simulations. This provides more accurate performance results without having access to all hardware components, as would be required for a full prototype testing.

The test platform is designed with complete modularity such that different types of tests can be performed for varying types of planetary rovers and in different environments. For demonstrating the operation of the test platform, however, the power system operation of a solar powered rover was examined. The system consists of solar panels, a solar charge controller, a battery, a DC/DC converter, a DC motor and a flywheel. In addition, a lighting system was designed to simulate the solar radiation conditions solar panels would experience throughout a typical day. On the software side, a library of component models was developed within MapleSim and model parameters were tuned to match the hardware on the test bench. A program was developed for real-time simulations within Labview allowing communication between hardware components and software models. This program consists of all the component models, hardware controls and data acquisitioning. The GUI of this program allows users to select which component is to be tested and which component is to be simulated, change model parameters as well as see real time sensor measurements for each component. A signal scaling technique based on non-dimensionalization is also presented, which can be used in an HIL application for obtain scaling factors to ensure dynamic similarity between two systems.

A demonstration of power estimation was performed using the pure software model simulations as well as the pure hardware testing. Hardware components were then added into the software simulation progressively with results showing better accuracy as hardware is added. The rover's power flow was also estimated under different load conditions and seasonal variation. These simulations clearly demonstrate the effectiveness of an HIL platform for testing a rover's hardware performance.

Acknowledgements

Firstly, I would like to thank my supervisor, Dr. Amir Khajepour for his guidance, motivation and patience right from the start of my graduate studies. This thesis would not have been possible without his continuous support and for that I will always be grateful. The research for this thesis was supported financially by NSERC and the Canadian Space Agency. In addition, I would like to acknowledge Maplesoft for their financial and technical support.

To my colleague and friend Brian Fan, thanks for all the help with the test setup as well as providing suggestions and motivation throughout my research. I would also like to thank John Boldt, Andy Barber and Niel Griffett for their advice and assistance in the hardware fabrication and setup process.

Finally, I would like to thank my friends here at the University of Waterloo for the great memories and to my family for all their support and encouragement throughout my entire university career.

Table of Contents

List of Figures

List of Tables

Nomenclature

a	Diode ideality constant
al	Surface albedo
A	Angular acceleration [rad/s^2]
C	Battery capacity [A s]
C_1	Battery capacitance [farads]
C_θ	Battery thermal capacitance [J/°C]
E_m	Battery open circuit voltage [V]
E_{m0}	Battery open circuit voltage at full charge [V]
G	Irradiation on solar cell surface [W/m^2]
G_{bh}	Direct beam irradiance on a horizontal surface in Mars [W/ m^2]
G_{bt}	Beam irradiance on a tilted surface in Mars [W/ m^2]
G_{dh}	Diffuse irradiance on a horizontal surface in Mars [W/ m^2]
G_{dt}	Diffuse irradiance on a tilted surface in Mars [W/ m^2]
G_h	Total irradiance on a horizontal surface in Mars [W/ m^2]
$G_{incident}$	Incident Irradiation on solar cell surface [W/m^2]
G_n	Nominal irradiation [W/ m^2]
G_{ob}	Direct beam radiation at top of Martian atmosphere [W/ m^2]
G_{obh}	Beam irradiance at the top of Mars atmosphere on a horizontal surface[W/ m^2]
G_{rt}	Reflected irradiance on a tilted surface in Mars [W/ m^2]
G_t	Total irradiance on a tilted surface in Mars [W/ m^2]
I	Rotational inertia [kg m^2]
I_a	Motor armature current [A]
I_d	Current through diode [A]
I_f	Motor field current [A]
I_m	Battery equivalent model main branch current [A]
I_o	Diode saturation current
I_p	Battery equivalent model parasitic current [A]
I_{pv}	Current generated by incident light to solar cell [A]

$I_{pv,n}$	Current generated at nominal condition [A]
$I_{sc,n}$	Nominal short circuit current
k	Boltzmann constant
K_I	Short circuit current temperature coefficient [%/°C]
k_m	Motor transformation coefficient [Nm/A]
K_v	Open circuit voltage temperature coefficient [%/°C]
L_a	Motor armature inductance [H]
L_f	Motor field inductance [H]
L_s	Areocentric longitude [°]
m	Number of fundamental dimensions
n	Number of system parameters
q	Electron charge
Q_e	Battery extracted charge [A s]
Q_{e_init}	Battery initial extracted charge [A s]
Q_{pi}	Number of Pi groups
$R_{0,00,1,10,2,20}$	Battery resistances [ohm] 0,00,1,10,2,20
R_a	Motor armature resistance [ohm]
R_b	Ratio of the beam irradiation on a tilted surface to that on a horizontal surface
R_f	Motor field resistance [ohm]
R_s	Solar cell series resistance [ohm]
R_{sh}	Solar cell parallel resistance [ohm]
R_θ	Battery thermal resistance [°C/W]
SOC	Battery state of charge
T	Ambience temperature [K]
T_n	Nominal temperature [K]
$V_{oc,n}$	Nominal open circuit voltage
V_{PN}	Battery equivalent model parasitic branch voltage [V]
z	Zenith angle [rad]
α_{cell}	Absorbtivity of solar cell

β	Angle of the tilted surface to the horizontal [rad]
δ_o	Mars obliquity of rotation [rad]
Θ_f	Battery electrolyte freezing temperature [°C]
T	Optical depth
τ_{glass}	Transmissivity of solar cell cover/glass
τ_p	Battery equivalent model parasitic branch time constant [sec]
τ_1	Battery equivalent model main branch time constant [sec]
φ	Latitude [°]
ω_s	Sunset hour angle [rad]
S	Solar constant at the mean Sun-Mars distance [W/ m^2]
e	Mar's eccentricity
r	Instantaneous Sun Mars distance in astronomical units (AU)
w	Hour angle measured from the true noon westward [rad]
γ	Surface azimuth angle [rad]
δ	Declination angle [rad]
θ	Battery electrolyte temperature [°C]
$\theta_{incident}$	Angle of Incident [rad]
ω	Motor rotational speed [rad/s]

Chapter 1
Introduction

1.1 Project Background

Space exploration has long been the subject of human fascination. With significant advances in technology, planetary rovers have been able to demonstrate their effectiveness for explorations on Mars and on the moon with successful rovers including the Soviet Union's Lunokhod (1970), and NASA's Sojourner (1996), Spirit (2003) and Opportunity (2003). In the coming decades, more difficult terrains will be explored and path planning and power management will continue to play a primary role in the success of rover missions.

A flexible and modular power management and path planning platform for planetary rovers is being developed at the University of Waterloo for the Canadian Space Agency. This platform will provide support to mission planners and designers by: 1) optimizing the trajectory based on the mission's goal; 2) providing efficient and effective power management using multidisciplinary optimization; 3) providing a dynamic model of a rover to predict kinematic validity and energy usage; 4) providing hardware-in-the-loop (HIL) testing; and 5) providing embedded simulation and animation capabilities.

The path planning optimization module generates an optimal path based on the mission's goal (minimal energy, minimal risk, minimal time, etc). The rover model can then capture the kinematics of the rover traveling through this path by providing information regarding the vehicle's position, orientation, tilt and speed. This information can be used as input to the HIL test platform since it directly affects the rover's energy generation and consumption. HIL testing can provide insight on component and powertrain system performance, as well as serve as a validation tool for the path planning and power management optimization modules. While each section of this project was developed individually, their interconnectedness is evident.

In the present work, the development of a hardware-in-the-loop test platform consisting of the main powertrain components on a planetary rover is described.

1.2 Problem Statement

The ability to estimate a rover's powertrain performance using computer generated models is invaluable. Software models allow for different design configurations to be compared by simply changing model connections and/or parameters. As well, the system's performance can be examined over a range of conditions by simulating various environments. However, depending on the novelty or complexity of the component, the difference between the model results and the actual hardware's performance can be significant, and thus full prototype testing is always required. Unfortunately, this requires a completed powertrain design, a rover prototype with all the powertrain components, as well as a test sandbox to simulate different terrain conditions. Thus, this is usually performed later in the testing phase. A novel approach is required to bridge the gap between the design and testing phase such that designers can quickly make reasonable predictions regarding the power generation/storage/consumption capabilities of a rover, while having only some of the components required for a full prototype testing.

1.3 Objectives

The objective of this thesis is to design an HIL test platform that will allow designers to estimate the performance of hardware on a planetary rover throughout a mission day, before all hardware components are available. To demonstrate the concept, a test bench consisting of powertrain components loosely based on NASA's Mars Exploration Rovers was developed. Concerning software, a library of mathematical models will be created consisting of the main powertrain components of a rover. The models will include the components' interaction with its operating environment such as seasonal fluctuations of temperature and solar intensity, and the rover's location, orientation, and tilt. This HIL test platform will allow for hardware to be added progressively into the simulation loop, with the idea that power flow estimation will become more accurate as more hardware components replace simplistic models in the simulation loop. A method for signal scaling must also be investigated to allow prototype components of different sizes to be tested. The rover model will be completely modular such that component parameters can be modified or component models can be replaced entirely to allow for design comparisons.

Chapter 2
Background/Literature Review

2.1 The Mars Exploration Rover Mission

NASA's Mars Global Surveyor was launched in November 1996 with the main goal of gathering observations of Mars over the course of one Martian year. While no evidence was found of liquid water on the surface, images taken from this orbiter provided clear signs that Mars had a wet past. So the question became whether or not a habitat suitable for life could have existed there.

In an attempt to answer this question, NASA launched two spacecrafts in 2003, as a part of the Mars Exploration Rover (MER) mission, targeting sites on opposite sides of Mars that appeared to have been affected by liquid water in the past. After traveling over 300 million miles, the first spacecraft, carrying the rover "Spirit", landed successfully on Jan 4, 2004. Twenty-one days later, the second spacecraft with the rover "Opportunity", also landed successfully [1]. Spirit and Opportunity were the most recent rovers to successfully land on Mars and will be the rovers that the simulations for the present work will be loosely based.

The primary objective of the rover missions was to characterize a wide range of rocks and soils to better understand past environmental conditions The two rovers were each designed to conduct geologic and atmospheric investigations for at least 90 Sols (93 earth days), and were expected to traverse a total distance of at least 600m [1].

Both rovers are of similar construction. Each has six wheels, each with an independently controlled motor, connected to a rocker bogie suspension. Instead of the typical spring suspension, the rocker bogie system uses two types of linkages, the "rocker" link and the "bogie" link. On each rover, there are two rockers connected to each other through a differential. When one rocker goes up the other goes down and the body maintains the average pitch angle of the two rockers. One end of a rocker is connected to a wheel and the other end is pivoted to a bogie link. The two bogie links have a wheel at each end. The rocker bogie suspension system has been the favored design for planetary rover due to its superior vehicle stability and obstacle climbing capability while providing high ground clearance. It has been used for both the Mars Pathfinder and Mars Exploration Rover missions. A computer generated model of the rover is shown in Figure 2-1. The rovers have a maximum speed of 50mm/s and an average speed of 10mm/s.

Each weighs 180 kg, and is 1.5m high, 2.3 m wide and 1.6 m long. The rovers are solar powered and use triple junction gallium arsenide solar cells which provide a maximum of 140W on Mars [2].

A shell, lander and rover are contained in each spacecraft. The shell is a protective cover that is used to protect the lander and rover inside it from the intense heat as it travels to Mars. The lander is a tetrahedron shape shell, whose sides open like petals. Together with airbags, it protects the rover from the forces of impact as it makes contacts with the ground.

Each spacecraft has three different batteries; primary, thermal and rechargeable. The primary and thermal batteries are located in the shell and lander. These are used to support the entry; descent and landing operations. The rechargeable battery is located in the rover and will aid in the launch, correct anomalies for cruise and support surface operations once it reaches Mars. Once Martian grounds are reached, the role of the rechargeable lithium-ion batteries is solely to support surface operations. The rechargeable battery has been designed to be a 30V, 600Wh system, with two parallel batteries (for a certain degree of redundancy), each of eight 10Ah cell in series. In order to maintain the rechargeable battery at moderate temperatures (-20 to 30 C), the battery is housed in a warm electronics box.

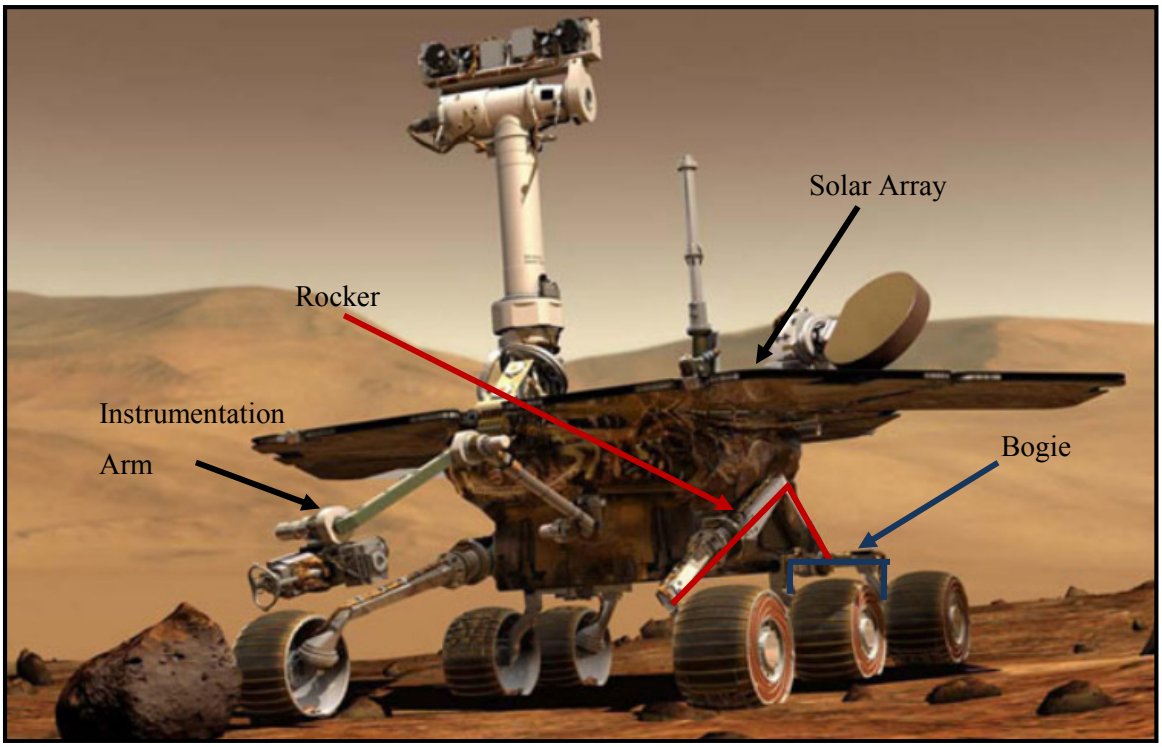

Figure 2-1 NASA's Mars Exploration Rover [2]

To explain the surface operations of these rovers, a typical day on Mars will be described. Since the rover is solar powered, it "sleeps" when the sun is not available. Even though there are batteries on the rover, the batteries were not designed to provide power for full operation of the rover throughout the night. It does however; provide power during the night to crucial components such as heaters to ensure that all instruments and components are within their operating temperature range. The batteries also provide power during the day when the power demand exceed the power generation due to sudden high load (e.g. obstacle climbing, instrumentation, etc) or a sudden decrease in the incoming solar energy caused by a cloud, dust storms or other events.

The rover begins each day by being "awakened" by an onboard alarm clock, and completes unfinished chores from the previous day's instructions. Communication with Earth is limited to twice a day for about one to two hours each because it uses the Deep Space Network, which is shared with other users. The first communication occurs when the Earth emerges above the Martian horizon. At this time, the rover receives a new set of commands for the day ahead with tasks such as crossing Martian terrain, approaching a rock, examining a rock target, taking images of surroundings, etc. While the rover is working, it records the data to be sent back. Not all information is sent directly to the Earth. Information can be sent to orbiters circling Mars, which in turn, directs the information back. As previously mentioned, when solar radiation is no longer available, main operations of the rover are stopped. However, performance of minor nighttime operations, such as transferring data to orbiters, continues. Back on Earth, scientists and engineers analyze the new information and formulate a new list of commands for the next Martian morning.

Understanding a rover's power usage is crucial to support surface operations in mobility, communication, and the various other instruments including a panoramic camera, two remote sensing instruments (a mini-thermal emission spectrometer and a mid-IR point spectrometer), and a number of in-situ pay-load elements (a Mossbauer spectrometer, an alpha-particle X-ray spectrometer, a microscopic imager, and a rock-abrasion tool) located at the end of a 5 degree of freedom arm [3]. Table 2-1 summarizes the power utilization for surface operations of the MER rovers on Mars [3].

Table 2-1 MER Rover Power Utilization

Activity		Power (W)
Orbiter Communication	CPU & I/O	19
	transmission	55
Lander relay communication	CPU & I/O	19
	transmission	10
Drilling	CPU & I/O	19
	peak motor	33
Imaging	CPU & I/O	23
	cameras	6
Raman Spectrometer		11
APXS (Alpha- Proton- X-Ray Spectrometer)		1.4
nightime spectrometer		2.3
daily housekeeping engineering (Whr)		141
nighttime operations (Whr)		75

2.2 The Planet Mars

Mars is unique as it is the only other planet in our solar system where surface-based meteorological stations can survive. Mars is also the only other planet where humans might be able to survive [4].

Mars is often described as "the Red Planet" due to the iron oxide on its surface which gives it its reddish appearance. Mars has surface features similar to Earth with volcanoes, valleys, deserts and polar ice caps. Because it has a comparable rotational axis tilt to Earth, Mars also experiences seasonal temperature changes. However, since it takes Mars almost twice as long to orbit the Sun, its seasons last longer. Additionally, with greater distance from the Sun, the average seasonal temperatures are significantly colder on Mars than on Earth. On a warm summer afternoon near the Martian equator, where the two MER rovers landed, the surface temperature can occasionally climb to 65° F (18°C). At the same location, the temperature at sunset will have dropped to below freezing and during the night can plunge to more

than 100 degrees below zero F(-73°C)[5]. These large diurnal temperature variations are common on Mars due to the low thermal inertia of the surface and the atmosphere.

Compared to the Earth, Mars' upper atmosphere receives much lower solar intensity due to its greater distance (1.5 times greater) from the Sun. In difference to Earth, however, the atmosphere of Mars is quite thin, leading to a much lower reduction in solar irradiation at the Martian surface caused by the absorption and scattering of the direct solar beam by molecules in the atmosphere. This leads to an overall lower but comparable amount of solar radiation on Mars in comparison to Earth.

A Mars solar day has a mean period of 24 hours 39 minutes 35.244 seconds. Following the long-standing practice originally adopted in 1976 by the Viking Lander missions, the daily variation of Mars solar time is reckoned in terms of a "24-hour" clock, representing a 24-part division of the planet's solar day[6]. The surface gravity on Mars is 3.71 m/s^2 [7], accordingly the power usage due to mobility is lower on Mars in comparison to Earth.

Mar's orbital eccentricity (0.09) is more pronounced in comparison to that of Earth's (0.016). Thus, a seasonal index called the areocentric longitude of the sun, Ls, is commonly used to measure the apparent seasonal advance of the Sun at Mars. In the northern hemisphere, an Ls value of 0°-90°, 90°-180°, 180°-270°,270°-360° corresponds to the seasons spring, summer, fall and winter respectively[6]. Seasons in Mars are on average about twice as long as on Earth (corresponding to the greater length of the Martian year). Table 2-2 summarizes the seasonal duration on Mars.

Table 2-2 Mars Seasonal Duration

Areocentric Longitude of the Sun (Ls in deg)	Season		Duration of the season	
	Northern Hemisphere	Southern hemisphere	Martian days	Terrestrial days
0 - 90	Spring	Autumn	194	199
90 - 180	Summer	Winter	178	183
180-270	Autumn	Spring	143	147
270-360	Winter	Summer	154	158

2.3 Hardware-in-the-Loop Background

With the mission's objectives in mind, engineers design the rover configuration and size the components with the help of simulation tools. Standard component testing then takes place which is useful to ensure that the components meet specific requirements. This step is crucial in determining its feasibility. For example, the Mars Exploration Rovers' (MER) rechargeable battery must provide sufficient cycle life of at least 90 sols on the surface of Mars, because the rovers were designed to operate for 90 sols. They must also operate over a wide temperature range, withstand long storage periods, operate in an inverted orientation and support high current pulses [8]. As previously mentioned, the battery not only provides power for surface operations but also assists in the launch. Thus, the ability to operate in an inverted orientation and support high current pulses for firing pyro events during launch are necessary. Component testing ensures its operation, but provides little information regarding the performance of a rover's powertrain system as a whole, or its interaction between components and the environment. Accordingly, the components are put on a test bench or a rover prototype for system level testing.

At the Computer History Museum, Pete Theisinger, the manager of the Mars Exploration Rover Project, gave a lecture outlining the design and testing process as well as the challenges faced in developing the twin rovers [9]. One of the challenges he explained was that during the system testing phase, it was discovered that the power needed, as predicted by computer simulations, was less than the actual power requirement, and that a larger solar array area was needed. A structural redesign at this stage would delay the project, and so hinges were added to the solar arrays on the MER allowing the extra area to fold up to fit sizing requirements.

Computer simulation is an attractive option in lieu of having all rover hardware available. However, the results can be made more accurate if hardware can be added to the simulation loop as it becomes available. Hardware in the Loop (HIL) simulation is a form of real-time simulation. Unlike pure software simulations however; it enables the interaction of virtual computer-based simulation models of a system with actual components of the system in real time. This method is being used in numerous disciplines because it permits the inclusion of components that are either not yet available or for which accurate computer models do not yet exist. HIL systems have been employed for decades by designers and test engineers to evaluate novel hardware or software within a system during development of new systems. Some of the industries currently using HIL systems include automotive, aerospace, aviation, robotics and power electronics [10][11][12][13][14].

Instead of testing hardware components in a complete system setup after all the parts are designed and prototypes are built, the physical component being tested are connected to software models that simulate the rest of the plant, and responds to the simulated signals as though they were operating in the real system, essentially creating a virtual reality for the component under test. In this manner, designers will be able to validate system performance with a virtual test vehicle, "driving" it through extensive simulated test terrains without leaving the lab. In addition, testing and simulation with the actual rover hardware in a simulation loop would be an effective way to detect and prevent unnecessary malfunctions of hardware. The ability to design and test power components of a rover in parallel with the development of the rest of the rover is a major advantage.

Traditional software-only simulation contains modeling errors. Construction of a rover prototype is costly, time-consuming and most importantly, cannot be done at the design stage. HIL testing is a method to bridge the gap between simulation and final system construction. It increases the realism of the simulation and provides access to hardware features currently not available in the software-only simulation.

Chapter 3
Hardware-in-the-Loop Test Platform

The proposed test platform allows for the incorporation of a planetary rover's hardware components within a software simulation. The platform is completely modular such that it can be used for a variety of testing. For example, one can use HIL testing to estimate the power of a rover throughout a mission day, before all the hardware components are available by using the associated software models to substitute the components which are not yet available. In addition to power level estimation, the HIL testing can be used to validate the power management optimization algorithm by comparing the energy usage throughout a given drive cycle for various powertrain configurations or designs. As well, it can be used as an extension to the path planning optimization module by determining the feasibility of a rover traversing through the optimal path generated by the optimization algorithm. Lastly, component testing can be performed on this platform.

To design such a testing platform, a library of mathematical models of powertrain components is required and a physical test bench with the hardware components must be designed. Users should be able to select which components are to be tested from the library and which are to be simulated. Sensors are required to evaluate hardware performance and a method must be established to ensure real time simulation. Also, a graphical user interface is needed to allow users to modify model parameters, select test hardware and view real time response of each component. The remainder of this chapter describes the hardware components that are on the test bench.

The test bench is made up of the main powertrain components: solar arrays, solar charge controller, DC DC converter, batteries and an electric motor. In addition to the main power components in a space rover, the setup consists of a lighting system to simulate solar input to the solar panels, a flywheel to simulate the rover's inertia as well as a load simulator which acts as a sink to simulate the power consumed by auxiliary components on the rover (e.g. scientific instrumentation, communication, onboard heaters etc). Figure 3-1 shows a schematic of the setup.

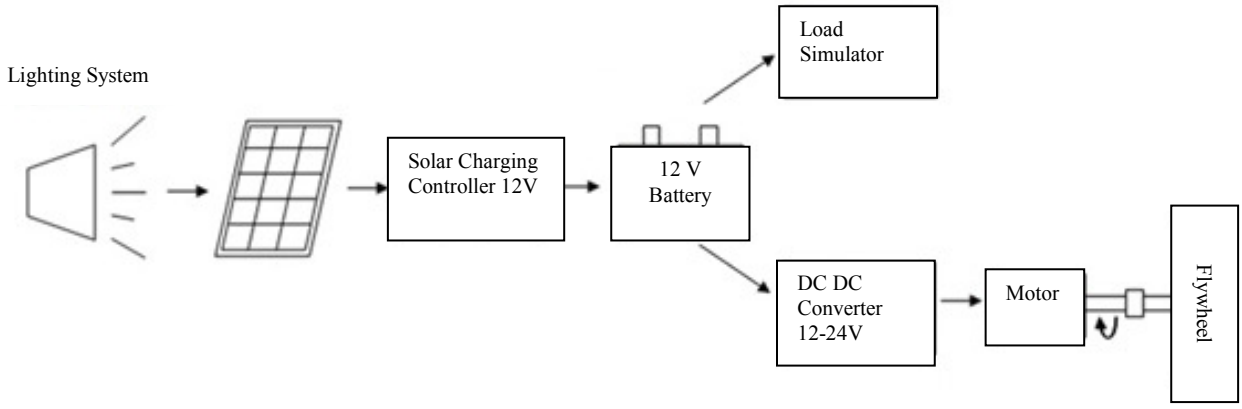

Figure 3-1 Schematic Diagram of Hardware

Note: These main power components are presented to demonstrate how hardware components can be added to a software simulation loop for rover performance testing and do not reflect actual hardware used in a rover.

3.1 Solar Arrays

The solar arrays used on Spirit and Opportunity were triple-junction solar arrays. The use of these specialized high efficient solar cells was crucial to the mission due to the rovers' weight and dimensional constraints. Fortunately, such constraints are not important for the test bench. Thus, single junction solar panels are selected as opposed to triple junction solar panels. Two single-junction solar panels are connected in parallel and used in this test bench. Each panel consists of 36 polycrystalline silicon cells connected in series and has a maximum rated power of 80W. The technical specifications for this device can be found in Appendix A.

3.2 Lighting System

Due to variations in solar radiation, an indoor lighting system will be used to energize the solar panels. This will result in highly reproducible conditions and results as well as a significant reduction in test time. An irradiation model (which will be discussed in Chapter 4) was used to predict a maximum irradiation level of 545W/m^2 on Martian surface at the location Opportunity landed. At the time of design, it was determined that the power required to match the energy output of lamps to that of the Sun would be remarkably high (~11kW). It was thus decided that the irradiation profile generated by the model will be scaled down for testing. The power generated will be reduced accordingly, however, the lighting system

should still provide a good conceptual representation of diurnal and seasonal effects on the power generated.

Twelve halogen lamps of 500W each were used for a distribution of light (to prevent hot/cold spots on the solar panel) while providing a reasonable amount of energy to power the solar panels. To simulate the effect of the varying irradiation levels on the surface of the solar panels throughout the day, the solar panels can be mounted on a tilt table to replicate the rover's motion as it is traversing through a path and the lamps can be mounted on a sliding railing to replicate the change in the sun's position throughout a day. Alternatively, the solar panels can be mounted on the wall and the lamps can be positioned to face the panels, as shown in Figure 3-2.

An irradiation model can be used to estimate the amount of irradiation a tilted surface would experience given the tilt, orientation and time of day. The intensity of the halogen lamps can then be controlled to track the output of the irradiation model. For example, if the rover is tilted away from the sun or when the sun is setting, the intensity of the light will be lowered accordingly. This avoids the complicated and expensive mechanical setup described above. However, this setup neglects the solar cells' directional response characteristics. The effects that the angle of incident of irradiation has on solar cells will be modeled theoretically in Chapter 4.

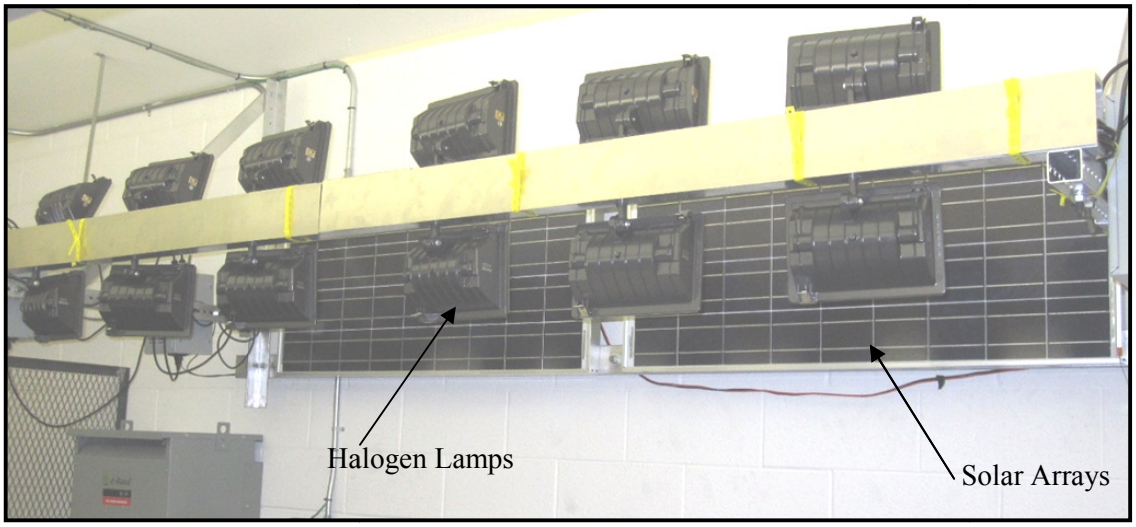

Figure 3-2 Solar Arrays and Lighting System

Pulse width modulation is a technique for controlling analog circuits with a processor's digital outputs. Essentially, the pulse width of a square wave, or the duty cycle, is varied to alter the average power of the

signal. For example, if a PWM signal has a 10 ms period and its pulses are 4 ms long, that signal is said to have a 40 percent duty cycle. In this case, a supply of 12V will result in a 4.8V output. By modifying the duty cycle of the PWM, the output of the lighting system can be controlled. A National Instrument multifunction data acquisition card was used to generate the PWM signals. See Appendix A for the circuit diagram of the control box.

Once the lighting system was set up, the irradiation levels were measured using a pyranometer (See Section 3.6). By varying the duty cycle, ten different light intensity levels were produced and their irradiation levels were recorded. This process was repeated four times with the location of the pyranometer being varied each time. The pyranometer was placed at the center and top left corner of the first solar panel, as well as the center and bottom right corner of the second solar panel. This was done to ensure that a similar level of light was received at different locations of the panels. The results at the four locations were averaged and a relationship between the duty cycle and irradiation level was developed (Figure 3-3). The relationship

$$x = .0024y + .086 \quad \textbf{(3-1)}$$

where x is the duty cycle and y is the irradiation level, was then used to determine the duty cycle for the PWM lighting control. In addition, from Figure 3-3, it can be seen that the maximum irradiation that the lighting system can provide is 370W/m^2. The irradiation profile generated by the model will thus be scaled down by 30%.

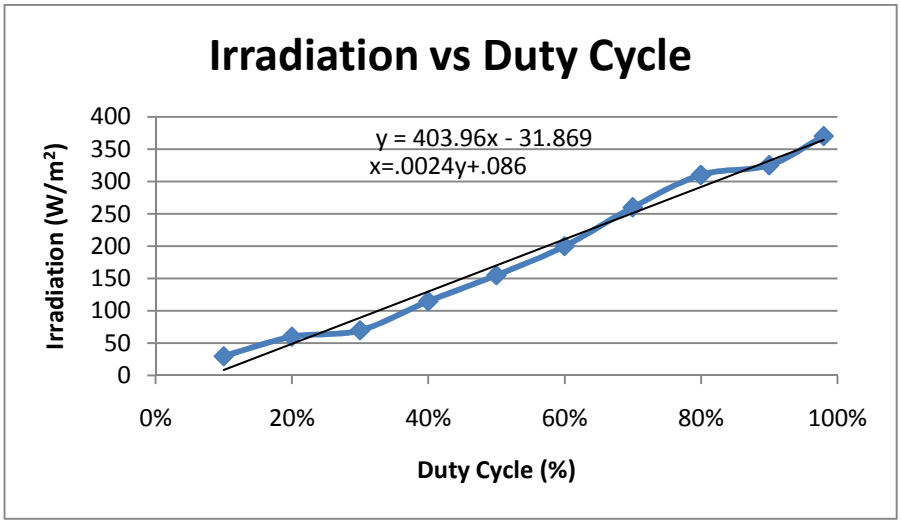

Figure 3-3 PWM Lighting Control Calibration

3.3 Battery

As previously mentioned, three types of batteries were used for the MER missions. In this work, only the rechargeable batteries will be considered since it is the sole battery supporting surface operations once it reaches Martian grounds.

Spirit and Opportunity each utilized Li ion rechargeable batteries. These cells were chosen as the energy storage device based on their high specific energy, excellent performance characteristics at low temperatures, high discharge rate capability, long life cycle, good storage characteristics and good pulse capability.

For the purpose of demonstrating the hardware in the loop test platform, an off-the-shelf MotoMaster rechargeable lead acid battery was used in the test bench. The battery operates at 12 volts with a capacity of 10 amp hours (See Appendix A for specifications). It is connected to the solar array through a 12V 30A solar charge controller (See Appendix A for specifications) to prevent the batteries from being overcharged by the solar array as well as to prevent the reverse flow of current back into the solar array.

3.4 Motor and Flywheel

The MER rovers each employ six traction motors. However, for demonstration purposes, this test bench will only consist of one motor driving a flywheel to simulate the rover's inertia. This setup will provide a good conceptual and visual representation of the load required to move a rover of a certain mass. A 24 V,

5HP DC shunt wound drive motor was used on this test bench (See Appendix A for specifications) to drive a flywheel with an inertia of 3.994 kg m^2. A TSX controller was used to provide speed control for the motor (See Appendix A for specifications). Figure 3-4 shows the battery, controllers, motor and flywheel setup in the lab

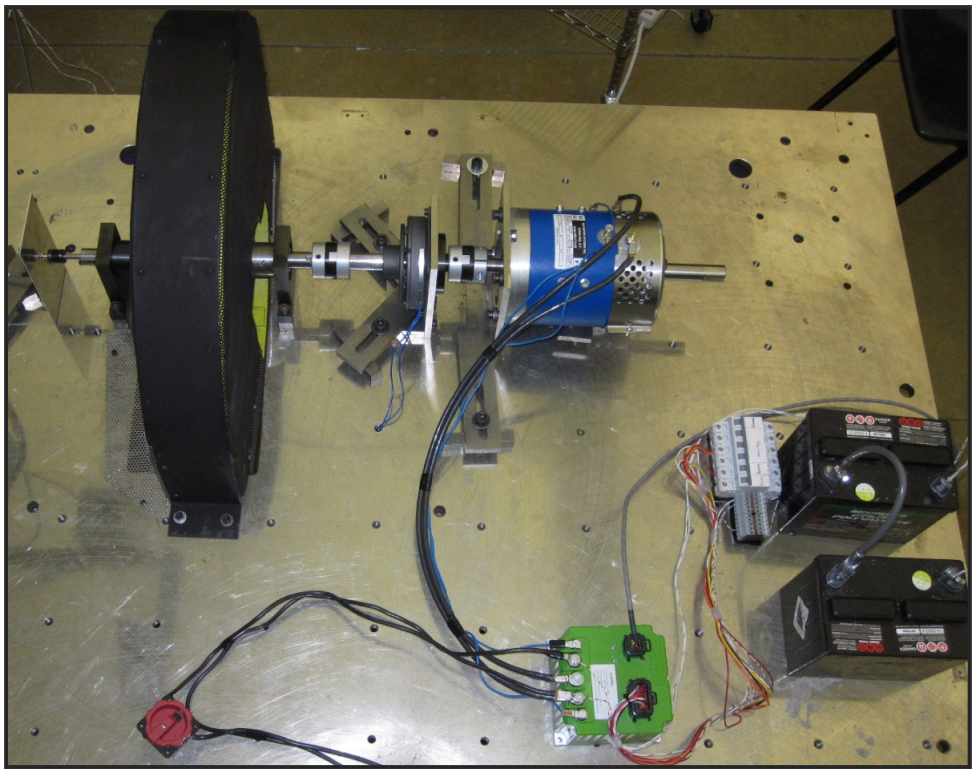

Figure 3-4 Battery, Controllers, Motor, Flywheel Setup

This representation does not account for the extra power consumed to overcome rolling resistance generated at the tire-soil interface or elevation changes. In order to include these effects, the dynamic model of a planetary rover, created by Dr. Orang Vahid [15], can be used. The model was created for a six wheeled rover with a rocker bogie suspension, like Spirit and Opportunity. A terrain was modeled including features such as hills and soil materials. The terrain was developed by interpolation of some randomly chosen waypoints. For the simulations, the surface gravity of Mars ($3.71 m/s^2$) was used. In this model, the normal and shear stress distribution in the wheel-soil contact area was calculated based on the wheel sinkage and slip ratio using the Bekker Formula. The forces acting on each wheel as well as its

torque and speed was then calculated. The power consumption of the rover as it traverses through a selected path can then be determined knowing the wheel speed and required torque. Refer to [15] for details of the dynamic model.

An additional motor can be added to the end of the flywheel (opposite the traction motor) to simulate this extra resistance due to the soil property and elevation changes. However, at the time of experimentation, an additional motor was not available. As an alternative, the power consumption calculated by the dynamic model can be lumped with the auxiliary power and simulated as an electronic load using the load simulator.

3.5 Load Simulator/ National Instrument PXI

An 1800W Sorensen load simulator will be used to simulate the electronic load of instrumentation and communication on a rover. When the motor-flywheel assembly is not used, the load simulator will also be utilized to simulate the power consumption related to the mobility of the rover. In the DC mode, the load simulator provides a range of 0-9A with 2.25mA resolution and an accuracy of ±0.5%. Connectivity is made with National Instruments hardware via a GPIB cable. See Appendix A for specifications of load simulator.

The data acquisition system (DAQ) utilized National Instruments hardware and software (LabVIEW version 2009 and LabVIEW RealTime). Real-time programs were developed in LabVIEW Real-Time on a host computer (Windows XP, 2 GHz). At runtime, the programs are sent over Ethernet to run on a hardware target which is an embedded computer (NI 8187, 2.5 GHz, LabVIEW RT booting). While the program runs, interaction with the front panel controls and indicators is available. The embedded computer and various interface cards (PXI 6229 and 6259) were installed in a NI PXI 1010 chassis. All outputs were interfaced with the embedded computer using NI hardware. The individual sensors (mV and V signals) were converted to engineering units using calibration factors input into the LabVIEW program and this data was recorded onto the embedded computer hardrive. The raw data was recovered from the DAQ computer back to the host computer for analysis. Figure 3-5 shows the NI PXI, load simulator and host computer setup in the lab. A pinout diagram describing the channels used for each input and output on this test bench is provided in Appendix D.

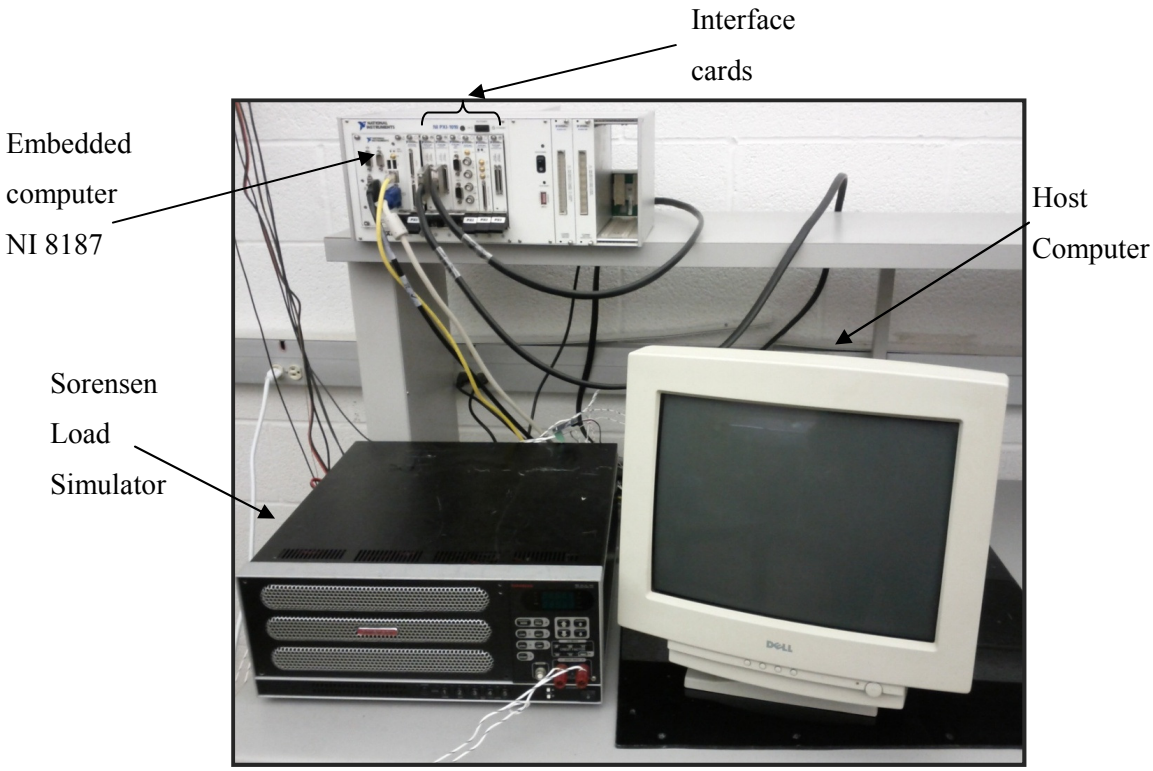

Figure 3-5 NI PXI, Load Simulator and Host Computer Setup

3.6 Sensors

A key factor of a HIL test platform is the ability to monitor the performance of the hardware components which can be achieved using sensors. The parameters of interest in this report include the irradiation, temperature, current, voltage and motor speed. A brief description of the sensors used on this test bench is provided below:

Pyranometer

To measure the input of the solar panels (light source), irradiance must be measured. Solar irradiance measurements were made using a silicon-cell pyranometer sensor manufactured by Apogee Instruments, SP-110.

The pyranometer was calibrated by the manufacturer to measure total shortwave radiation. It has a narrower response range in comparison to pyranometers designed to measure solar intensity and more closely mimics the response range of PV cells. Thus, they were a suitable choice for this application. The

spectral response of the selected pyranometer is shown in Figure 3-6. The pyranometer was calibrated to 5.00 W m^{-2} per mV. The accuracy of the irradiance data from the sensor was estimated by the manufacturer to be ±5%. See Appendix A for specifications. Real time data is recorded using this sensor for each test to verify the irradiation level that the solar panels are experiencing.

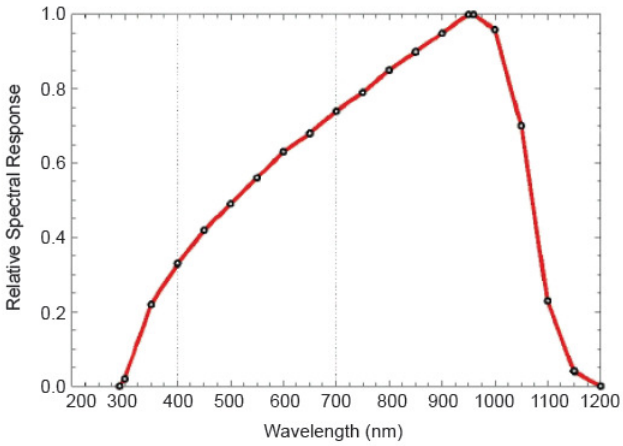

Figure 3-6 Spectral Response of Apogee Pyranometer [16]

Thermocouple

The test setup does not incorporate temperature control; however temperature readings were taken at the beginning of each test. This is important to ensure that tests were performed on days with similar temperatures so that comparisons can be made between different tests. Two K type thermocouples were used; one was placed between the two solar panels while another was placed away from the test setup for ambient temperature readings. See Appendix A for specifications.

Voltage and Current Sensor

Voltage and current sensors were used at different parts of the system; after the solar panels, charge controller, DC DC converter and the battery. The voltage sensor measures voltage from -30V to +30V and has a reported maximum error of ±2%. The following formula as provided by the manufacturer was used to translate the sensor value into a differential voltage.

$$V_{differential} = (SensorValue - 2.5)/0.069 \quad \textbf{(3-2)}$$

The current sensor measures DC from -30A to +30A and has a reported maximum output error of ±5%. The following formula as provided by the manufacturer was used to translate the sensor value into current is

$$Current = \left(\frac{SensorValue}{15.1515}\right) - 37.3087 \quad \textbf{(3-3)}$$

Eqn. (3-2) and Eqn.(3-3) were used within the LabVIEW program (described in Chapter 5). See Appendix A for specifications of sensors.

Encoder

An optical incremental shaft encoder was used to measure the shaft angular position and speed. The encoder had a resolution of 2000 counts per revolution. It is mounted on the shaft of the flywheel. See Appendix A for the encoder specifications and pin-out.

Chapter 4
Modeling

A library of mathematical models for powertrain components and the environment was created for the HIL test platform. The models described in this chapter reflect the hardware components found on the test bench. As more components are added to the library, different rovers can be simulated (e.g. a rover powered by radioisotope thermoelectric generators (RTGs) instead of solar panels).

4.1 Environment

Planetary environments impose significant constraints on the design and operability of an autonomous rover. One of the main constraints for a solar powered planetary rover is solar radiation. Data on solar radiation is not readily available and thus will be estimated based on planetary ephemeris as well as optical depth data collected by NASA's Viking Lander 1 and 2.

4.1.1 Irradiation

For solar powered rovers, the output of the solar arrays is the main operational constraint on the amount of power available for science operations throughout the day. A solar powered rover must evaluate the energy cost of its operating path and determine the effect of the time of travel on the orientation of its solar array relative to the sun in the sky. Several factors need to be considered: the visibility and strength of sunlight, the solar panel configuration, and the changing orientation of those panels with respect to the sun. The apparent motion of the sun over time in a particular location combined with terrain maps will indicate whether or not the sun will be visible at a given location, and at which angle the sunlight will be incident on the panels. A procedure was presented by J.Appelbaum[17] to calculate the diurnal and daily variation of solar radiation on Mars. The described method was used for the design of the Pathfinder's photovoltaic arrays. This method was implemented within MapleSim to estimate the available solar radiation experienced by a tilted surface on Mars.

Solar Irradiance at top of Mars Atmosphere

Solar radiation at the top of the Martian atmosphere varies by the location of Mars in its orbit and is composed entirely of direct beam radiation. The beam irradiance is given by the inverse square law

$$G_{ob} = \frac{S}{r^2} \quad \textbf{(4-1)}$$

where S is the solar constant at the mean Sun-Mars distance, S=590 W/m^2 and r is the instantaneous Sun-Mars distance in astronomical units (AU) (1 AU is 1 Astronomical unit = mean Sun-Earth distance =1.496 x 10^8 km)

$$r = \frac{(1 - e^2)}{1 + ecos\theta} \quad \textbf{(4-2)}$$

Where e is Mar's orbital eccentricity e=0.093377 and θ=L_s-248° where L_s is the areocentric longitude.

From Eqn. (4-1) and Eqn. (4-2), the instantaneous beam irradiance can be expressed as

$$G_{ob} = 590\frac{[1 + ecos(L_s - 248°)]^2}{(1 - e^2)^2} \quad \textbf{(4-3)}$$

Irradiance at top of Mars Atmosphere on a Horizontal Surface

The beam irradiance on a horizontal surface is

$$G_{obh} = G_{ob}\cos(z) \quad \textbf{(4-4)}$$

where z is the zenith angle of the incident solar radiation given by

$$\cos(z) = \sin(\emptyset)\sin(\delta) + \cos(\emptyset)\cos(\delta)\cos(w) \quad \textbf{(4-5)}$$

where

$\emptyset$ = latitude, δ = declination angle, w = hour angle measured from the true noon westward

The solar declination angle is given by

$$\sin(\delta) = \sin(\delta_o)\sin(L_s) \quad \textbf{(4-6)}$$

where $\delta_o = 24.936$ is the Mars obliquity of rotation axis.

The hour angle can then be calculated by $w = 15T - 180$ where T is defined as the Mars solar time T (a 24-part division of the planet's solar day). For a given latitude, G_{obh} is a function of L_s (daily variation) and T (diurnal variation)

Solar Irradiation on a Horizontal Surface in Mars

Solar radiation reaches the Mar's surface either by being transmitted directly through the atmosphere ("direct solar radiation"), or by being scattered to the surface ("diffuse sky radiation"). The solar irradiance components on a horizontal surface can be described by

$$G_h = G_{bh} + G_{dh} \quad \textbf{(4-7)}$$

where G_h is the total irradiance on a horizontal surface, G_{bh} is the direct beam irradiance on a horizontal surface and G_{dh} is the diffuse irradiance on a horizontal surface.

In addition to the Mars-Sun distance and solar zenith angle, the opacity (optical depth) and surface albedo of the Martian atmosphere must also be factored in to obtain the irradiance on the surface of Mars.

Optical Depth τ

Optical depth is a measure of the visual or optical thickness the atmosphere (dust, smoke layers etc) or the reduction of light/ energy transmitted through the atmosphere due to interactions with particles. It is an important factor to the variation of the solar radiation on the Martian surface and is non-dimensional. Large values of opacity correspond to global storms. When no dust storms are present, optical depth is typically about 0.5[17]. NASA's VL1 and 2 collected daily opacity levels for one Martian year (Appendix B) and this data will be used for the model. Note: Opacity is assumed to remain constant throughout the day.

Surface Albedo

Surface albedo is a measure of how strongly solar radiation is reflected by the surface. Measured from space, it gives an indication of a planet's surface and atmospheric reflection and absorption. For this model, the albedo behavior of Mars as measured by the Viking IRTM instruments will be used and are presented in Appendix B. The measured albedo ranges from 0.15 to 0.425 and has a mean of about 0.27[17].

Calculations were done by Pollock [18] to determine the net solar flux at varying optical depth, solar zenith angle and surface albedo (Appendix B). For surface albedo values between 0.1 and 0.4, interpolation was used. The global irradiance G_h on a horizontal surface can be determined using the normalized net solar flux function *f(z,τ, al)* in the following equation

$$G_h = G_{ob}\cos(z)\frac{f(z,\tau,al)}{1-al} \quad \textbf{(4-8)}$$

where *al* is the albedo.

The direct beam irradiance on a surface normal to the solar rays can be calculated using Beer's law which relates G_b to the optical depth of the intervening atmospheric haze.

$$G_b = G_{ob}\exp\left[-\tau m(z)\right] \quad \textbf{(4-9)}$$

where *m(z)* is the air mass determined by the zenith angle z and can be approximated for zenith angles up to about 80 degrees by

$$m(z) \cong \frac{1}{\cos(z)} \quad \textbf{(4-10)}$$

The direct beam irradiance on a horizontal surface can then be approximated as

$$G_{bh} = G_{ob}\cos(z)\exp\left[-\frac{\tau}{\cos(z)}\right] \quad \textbf{(4-11)}$$

The diffuse sky irradiation on a horizontal surface can then be back calculated

$$G_{dh} = G_h - G_{bh} \quad \textbf{(4-12)}$$

Solar Irradiation on a Tilted Surface in Mars

If the terrain of Mars was perfectly flat the above formulae could be used. However, sloped terrain, rocks and ditches are common on Mars and thus equations for a tilted surface must be used. Instead of just direct solar radiation and diffuse sky radiation, the radiation reflected off the ground must also be accounted for to obtain the total solar irradiation on a tilted surface (Figure 4-1). The total solar irradiance on a tilted surface can be described by

$$G_t = G_{bt} + G_{dt} + G_{rt} \quad \textbf{(4-13)}$$

where G_t is the total irradiance on a tilted surface, G_{bt} is the beam irradiance on a tilted surface, G_{dt} is the diffuse irradiance on a tilted surface and G_{rt} is the reflected irradiance on a tilted surface.

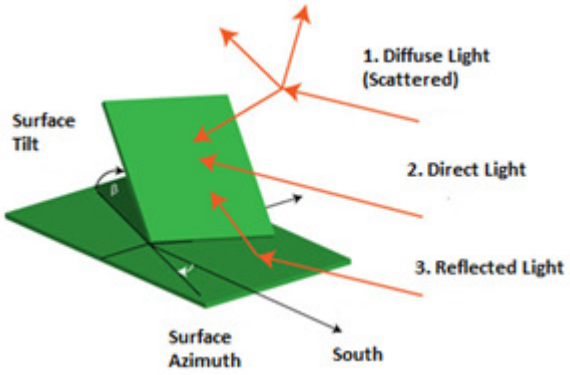

Figure 4-1 Solar Irradiation for a Tilted Surface [19]

Shape Factor

The shape factor for the tilted surface with respect to the sky and surrounding ground is $\frac{1+\cos(\beta)}{2}$ and $\frac{1-\cos(\beta)}{2}$ respectively, where β is the angle of the tilted surface to the horizontal.

Assuming isotropic distribution of diffuse radiation over the sky, the diffuse and reflected components can be described as

$$G_{dt} = G_d \frac{1+\cos(\beta)}{2}, G_{rt} = \rho(G_{bh} + G_{dh}) \frac{1-\cos(\beta)}{2} \quad \textbf{(4-14)}$$

In reality, the distribution of diffuse radiation is anisotropic. However, for most engineering calculations, it is acceptable to consider the distribution of the diffuse radiation to be isotropic [20].

The direct beam irradiation on a tilted surface can be calculated by

$$G_{bt} = G_b R_b \quad \textbf{(4-15)}$$

where R_b is the ratio of the beam irradiation on a tilted surface to that on a horizontal surface.

For a tilted surface facing south ($\gamma = 0°$),

$$R_b = \frac{\sin(\delta)\sin(\emptyset - \beta) + \cos(\delta)\cos(\omega_s{}')\cos(\emptyset - \beta)}{\sin(\emptyset)\sin(\delta) + \cos(\emptyset)cos(\delta)cos(\omega_s{}')} \quad \textbf{(4-16)}$$

where γ is the horizontal angle between south and the direction the tilted surface is facing (surface azimuth angle) and $\omega_s{}'$ is the sunset hour angle for a tilted surface which is given by

$$\omega_s' = min[\omega_s, \cos^{-1}(-\tan(\emptyset - \beta)\tan(\delta)] \quad \textbf{(4-17)}$$

For tilted surfaces facing any other direction,

$$R_b = \left[\frac{\cos(\beta)\sin(\delta)\sin(\emptyset)\,\pi}{180}(\omega_{ss} - \omega_{sr}) - \frac{\sin(\delta)\cos(\emptyset)\sin(\beta)\cos(\gamma)\,\pi}{180}(\omega_{ss} - \omega_{sr}) \right. \quad \textbf{(4-18)}$$
$$+ \cos(\delta)\cos(\gamma)\sin(\emptyset)\sin(\beta)\,(\sin(\omega_{ss}) - \sin(\omega_{sr}))$$
$$\left. + \cos(\delta)\sin(\beta)\sin(\gamma)(\cos(\omega_{ss}) - \cos(\omega_{sr}))\right]$$
$$/\left\{2\cos(\emptyset)\cos(\delta)\sin(\omega_s) + \frac{\pi}{180}\omega_s \sin(\emptyset)\sin(\delta)\right\}$$

If $\gamma<0$,

$$\omega_{sr} = -min\left\{\omega_s, cos^{-1}\left[\frac{(AB + \sqrt{A^2 - B^2 + 1})}{A^2 + 1}\right]\right\} \quad \textbf{(4-19)}$$
$$\omega_{ss} = min\left\{\omega_s, cos^{-1}\left[\frac{(AB - \sqrt{A^2 - B^2 + 1})}{A^2 + 1}\right]\right\}$$

If $\gamma>0$,

$$\omega_{sr} = -min\left\{\omega_s, cos^{-1}\left[\frac{(AB - \sqrt{A^2 - B^2 + 1})}{A^2 + 1}\right]\right\} \quad \textbf{(4-20)}$$
$$\omega_{ss} = min\left\{\omega_s, cos^{-1}\left[\frac{(AB + \sqrt{A^2 - B^2 + 1})}{A^2 + 1}\right]\right\}$$

where

$$A = \frac{\cos(\emptyset)}{\sin(\gamma)\tan(\beta)} + \frac{\sin(\emptyset)}{\tan(\gamma)}, \quad B = \tan(\delta)\left|\frac{\cos(\emptyset)}{\tan(\gamma)} - \frac{\sin(\emptyset)}{\sin(\gamma)\tan(\beta)}\right|, \quad \omega_s = cos^{-1}(-\tan(\emptyset)\tan(\delta))$$

Clearly, both the orientation γ and tilt β of the rover affect the irradiation experienced by solar panels on a rover. These values would be generated by simulating a dynamic model of a rover traversing through a path. However, a dynamic rover model is outside the scope of this thesis and thus reasonable values will be generated and used for simulation purposes.

It should be noted that the calculated solar irradiation using this model is based on data from less than two Martian years, and thus corresponds to short-term data. Also, opacity data were obtained from two locations (VL1 is located at 22.3°N and 47.9°W, VL2 is located at 47.7°N and 225.7°W). As such, the calculated data may be representative only of latitudes close to the landers' sites.

MapleSim Model

Given a specific latitude and L_s, the model which was implemented in MapleSim 4 (See Appendix C for full model) will output the diurnal variation in solar irradiation. This output is used in two scenarios. If solar panels are available for the HIL simulation, this output will be used to control the intensity of the halogen lamps. Otherwise, it is used as the input to the solar panel model described in the next section to predict the power generation.

Using this model, the diurnal variation was generated for a latitude of 22.3deg on a clear day and various key factors were varied to show their effects on the irradiation profile. As expected, the solar panels would experience less irradiation during the winter months both in intensity as well as duration (Figure 4-2).

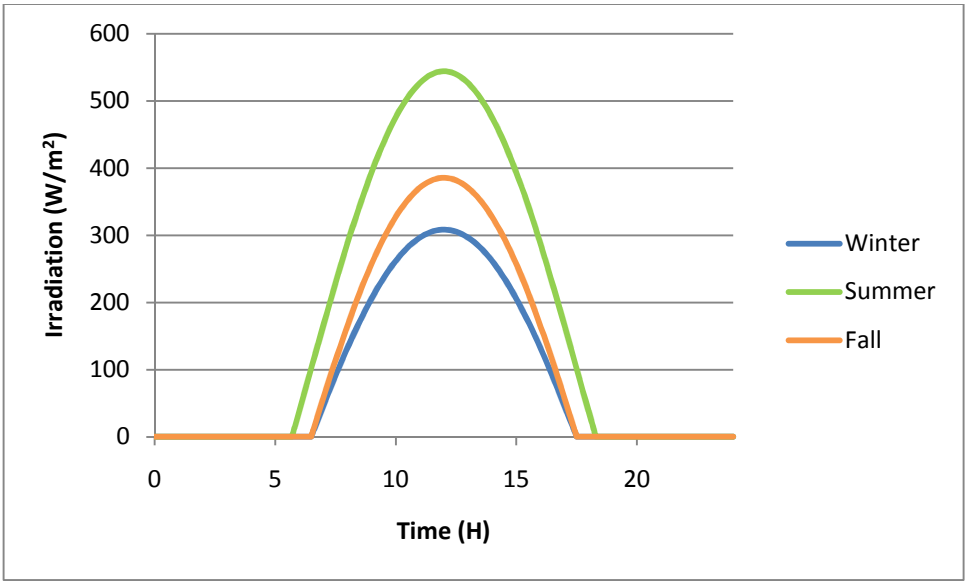

Figure 4-2 Seasonal Effect on Diurnal Irradiation Profile

Note that from Chapter 3, the maximum irradiation that our lighting system can provide is 370W/m^2. However, this irradiation model predicts a maximum irradiation level of 545W/m^2 during a summer day

on Mars. Therefore, the irradiation profiles generated by the model will be scaled down by 30% for testing.

Figure 4-3 shows the effects on the irradiation profile as the vehicle undergoes a linear orientation change throughout the day while on a tilt. Note that when the vehicle has no tilt, the orientation has no effect on the irradiation profile.

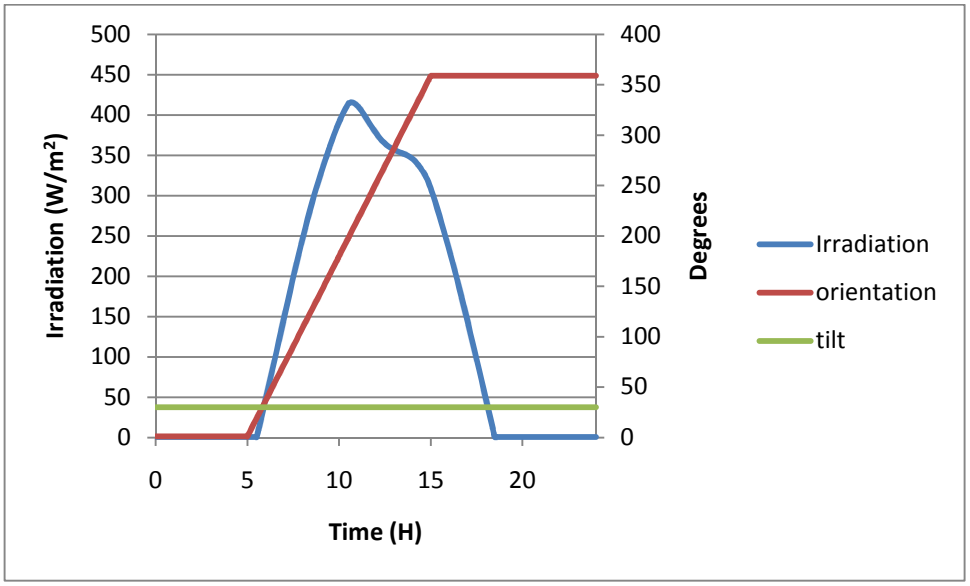

Figure 4-3 Effects of Vehicle Orientation on Irradiation Profile

Figure 4-4 shows the effect on the irradiation profile as the vehicle undergoes tilting motion in a sinusoidal pattern.

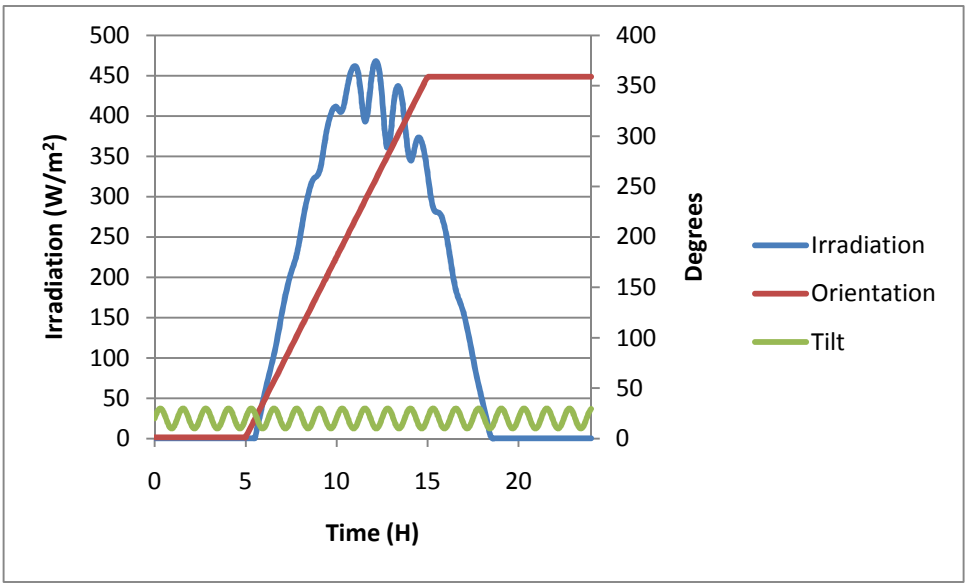

Figure 4-4 Effect of Vehicle Tilt on Irradiation Profile

4.1.2 Temperature

As mentioned in Chapter 2, large temperature variations are common on Mars, with an average diurnal range of approximately 50 K. This large diurnal temperature variation affects the operation and performance of the powertrain components and will thus be considered in the modeling. To date, the results from the Viking experiments provide a most complete view of temperature on Mars and are presented in Appendix B.

4.2 Solar Array

4.2.1 Model

For the test setup, single junction cells were used since we were not concerned with weight and panel dimensional sizing. Accordingly, a single junction solar panel was modeled. An ideal PV cell can be modeled by a current source I_{pv} in parallel with a diode I_d [21].

$$I_{ideal} = I_{PV} - I_d \quad \textbf{(4-21)}$$

I_{pv} is the current generated by the incident light. It varies with the solar irradiation and is also influenced by the temperature as described in the following equation.

$$I_{PV} = (I_{PV,n} + K_I(T - T_n))\frac{G}{G_n} \quad \textbf{(4-22)}$$

where G (watts/m^2) is the irradiation on the device surface, G_n is the nominal irradiation, $I_{pv,n}$ (amperes) is the light generated current at the nominal condition (usually 298K and 1000W/m2), K_I is the short circuit current temperature coefficient, T is the temperature in K of the p-n junction, and T_n is the nominal temperature in K.

Using the nominal short circuit current $I_{sc,n}$ provided by manufacturer datasheets, $I_{pv,n}$ can be obtained by $I_{pv,n} = \frac{(R_S+R_p)}{Rp} I_{scn}$. The assumption $I_{sc} \approx I_{pv}$ is generally used in the modeling of PV devices since in practical devices the series resistance is low and the parallel resistance is high[21].

Since the angle of incident of irradiation varies throughout the day, the solar cell's directional response characteristics are important in determining the cell's performance. A simplistic approach can be used to estimate the effects that the angle of incident irradiance has on solar cells by considering the solar rays penetrating the transparent cover of the cell and the percentage being absorbed by the cell itself. This can be represented by the following formula

$$G = G_{incident} * \cos(\theta_{incident}) \times \tau_{glass}(\theta_{incident}) \times \alpha_{cell}(\theta_{incident}) \quad \textbf{(4-23)}$$

Where $G_{incident}$ is the incident irradiance in W/m^2, $\theta_{incident}$ is the angle of incidence in radians, τ is the transmissivity of the glass and α is the absorbtivity of the solar cell.

From Eqn. (4-23), it can be seen that both the transmissivity and absorbtivity is a function of the incident angle. Transmissivity of a glass (with a refractive index of 1.5) of a solar array as a function of angle of incidence was calculated by Shurcliff [22]. It was shown that for angles 0°-20°, the transmissivity is essentially constant, from 20°-56°, the transmissivity decreases at a rate of approximiately 0.0015/°. For larger angles, the transmissivity is decreased significantly, reaching a value of 0 at 90°. Absorptivity of a silicon solar cell was determined as a function of the angle of incidence by Santbergen [23]. In his work, it was found that for angles of incidence between 0° to 60°, the absorptivity is more or less constant. For

larger values of angle of incidence however, the absorptivity of the cell decreases significantly, to a value of 0 at 90°.

Using Eqn. (4-23), this model is capable of estimating the PV cell's directional response characteristics. However, since the lamps on the test bench were in fixed positions, constant values of $\theta_{incident}$, $\tau_{glass}$and α_{cell} were used in the simulations so that results from the hardware testing can be compared to the simulation results.

I_d is the current through the diode and can be found using the Shockley diode equation

$$I_d = I_o[exp\left(\frac{qV}{akT}\right) - 1] \quad \textbf{(4-24)}$$

where q is the electron charge = 1.60217646 x 10^{-19} C, k is the Boltzmann constant = 1.3806503 x 10^{-23} J/K), and a is the diode ideality constant.

I_o is the diode saturation current and can be described by

$$\mathrm{I_o} = \frac{\mathrm{I_{sc,n}} + \mathrm{K_I}\Delta\mathrm{T}}{\exp\left(\frac{\mathrm{V_{oc,n}} + \mathrm{K_V}\Delta\mathrm{T}}{\mathrm{aV_t}}\right) - 1} \quad \textbf{(4-25)}$$

where $I_{sc,n}$ is the nominal short circuit current, $V_{oc,n}$ is the nominal open circuit voltage, K_v is the open-circuit voltage temperature coefficient, and $\mathrm{V_t} = \frac{\mathrm{N_s kT}}{\mathrm{q}}$ and $\Delta\mathrm{T} = \mathrm{T} - \mathrm{T_n}$.

When charged by the sun, a solar cell only generates a small voltage. To produce useful DC voltages, the cells are connected together in series. Practical PV panels are composed of an array of several connected PV cells. Cells connected in series provide greater output voltages while cells connected in parallel increase the current. If the array is composed of N_s cells connected in series and N_p cells connected in parallel, Eqn. (4-21) becomes:

$$\mathrm{I_{ideal,}} = \mathrm{N_p I_{PV}} - \mathrm{N_p I_o}[\exp\left(\frac{\mathrm{qV}}{\mathrm{akTN_s}}\right) - 1] \quad \textbf{(4-26)}$$

In real cells, power is dissipated through the resistance of the contacts and through leakage currents around the sides of the device. These effects are equivalent electrically to two parasitic resistances in series R_s and in parallel R_{sh} with the cell (Figure 4-5). R_s depends on the contact resistance of the metal base with the p-type layer, the resistances of the p and n bodies, the contact resistance of the n layer with

the top metal grid and the resistance of the grid. Series resistance is a particular problem at high current densities, for instance under concentrated light. The R_{sh} resistance exists mainly due to the leakage current of the p-n junction and depends on the fabrication method of the PV cell. For an efficient cell, it is desirable for R_s to be as small as possible and R_{sh} to be as large as possible [24].

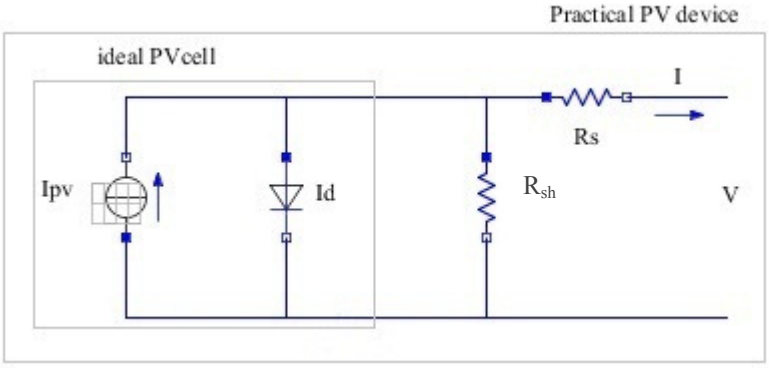

Figure 4-5 Equivalent Circuit of PV cell using Single Diode Model

PV array datasheets provide the following information:

$V_{oc,n}$, $I_{sc,n}$,K_v, K_I, P_{max}

This leaves three parameters unknown: *a, R_s and R_{sh}*. The value of the diode constant *a* expresses the degree of ideality of the diode and is entirely empirical with values ranging typically from 1-1.5[21]. An initial value between 1-1.5 can be chosen and this can be later modified to improve the model fitting of the I-V curve. The two remaining parameters R_s and R_{sh}, are also to be determined experimentally. Using the single diode model, a PV model was created in MapleSim (Figure 4-6). On the left are all the inputs for the model. The block 'Current' is used to generate the current I_{pv} as calculated by Eqn. (4-22) and Eqn.(4-23). The custom component 'D_1' represents the diode which is in parallel to the current source I_{pv}. The current through the diode is calculated using Eqn. (4-24) and Eqn. (4-25). Resistances R_{sh} and R_s were added in the manner depicted in Figure 4-5. To produce an IV curve, a ramp voltage was used at the terminal. In addition, the power output is obtained by taking a product of the output from the current and voltage sensor blocks.

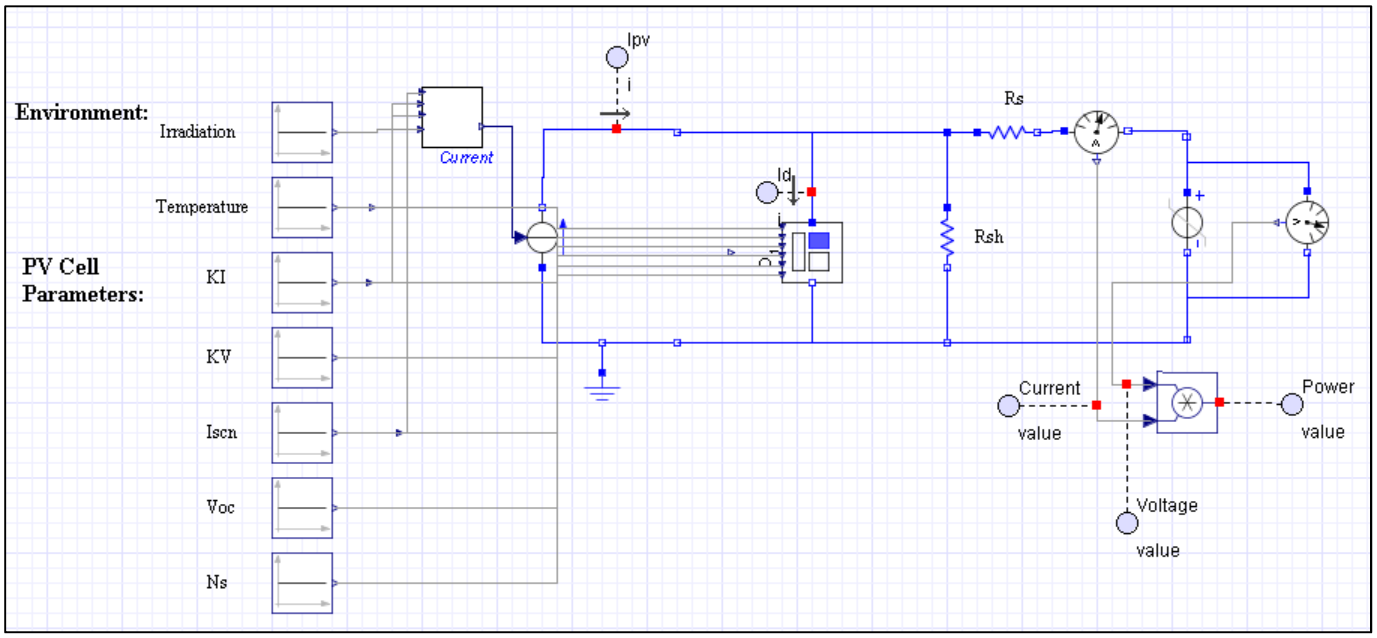

Figure 4-6 MapleSim Model of Single Junction Photovoltaic Cell

4.2.2 Parameterization

I-V Curve

The I-V curve of an illuminated PV cell, as shown in Figure 4-7, provides many performance parameters such as the maximum power (P_{max}), current and voltage at P_{max} (I_{mp} and V_{mp}), fill factor and maximum efficiency. As a result, tests to obtain IV curves are commonly performed during research and validation of solar panel performance.

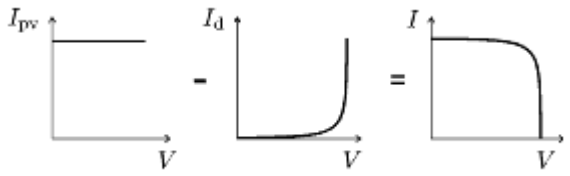

Figure 4-7 I-V characteristic of a PV cell [21]

Test Setup

A load simulator was used to sweep the current and measure the voltage from the panel at three different irradiation levels. Many of the aforementioned parameters are affected by ambient conditions such as temperature and the intensity and spectrum of the light source. It was therefore necessary to test PV cells using similar lighting and temperature conditions for each test. A pyranometer was used to measure the irradiance of the incident light and a thermocouple was used to measure the temperature at which the test was conducted. NI PXI and Labview were used to acquire, analyze and display the results of the I-V characterization tests.

When there is no light source to generate current, the solar cells behave like a diode. As the light intensity increases, current is generated. Figure 4-8 shows the qualitative effect of the light intensity on the IV curve.

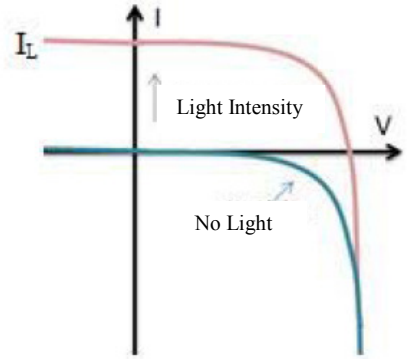

Figure 4-8 Effect of Light Intensity on IV curve of Solar Cell [25]

Series resistance in solar cells represents the contact resistance between the metal contact and silicon as well as the resistance of the top and rear metal contacts. Figure 4-9 shows the effect of the series resistance on the IV curve. Shunt resistance exists mainly due to leakage current of the p-n junction and depends on the fabrication method of the photovoltaic cell. The amount of current flowing through the solar p-n junction is reduced due to the leakage current and leads to power losses. Figure 4-10 shows the effect of the shunt resistance on the IV curve. In an ideal cell, shunt resistance would be infinite, removing the alternate path for current to flow, while series resistance would be zero. Parameters (a, R_s, R_{sh}) were experimentally determined through comparing the software vs hardware IV curves. Figure 4-11 shows the IV curve of the tuned model vs. the hardware at three different irradiations. At each irradiation level, two

tests were run and the results were averaged. The system will be regulated around 12V and from Figure 4-12, the percent error between the model and hardware is less than 2% for voltages below 17V.

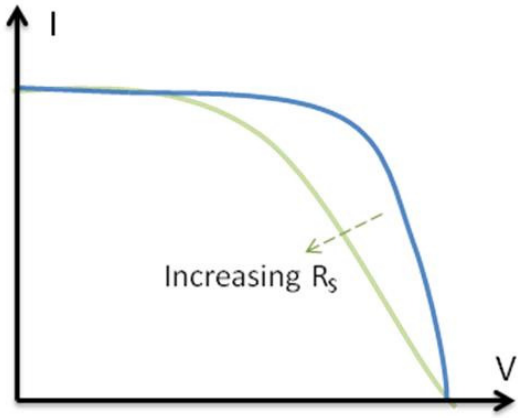

Figure 4-9 Effect of R_s on IV curve of solar cell [25]

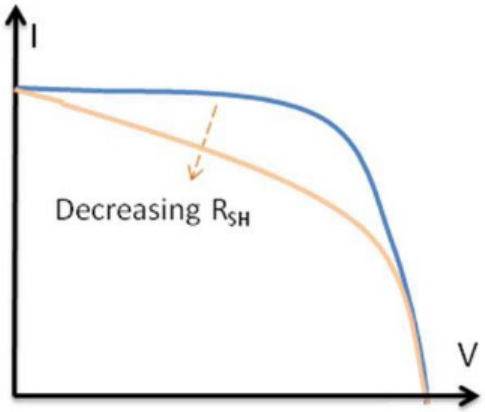

Figure 4-10 Effects of R_{sh} on IV curve of solar cell[25]

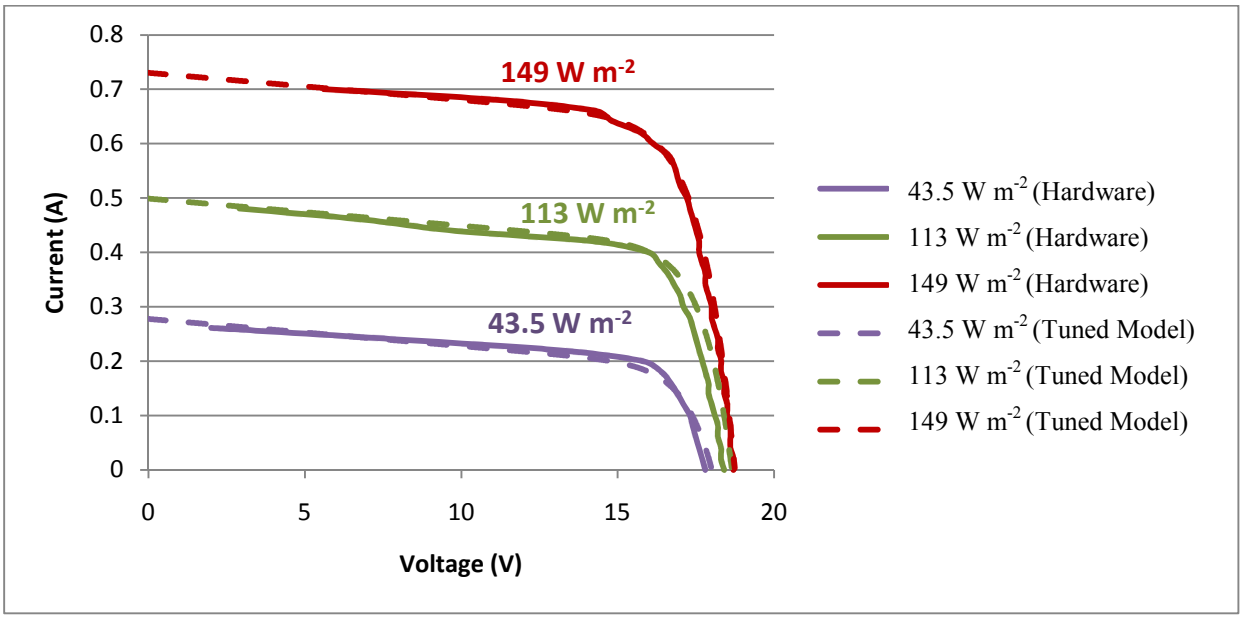

Figure 4-11 Hardware vs. Model IV curve

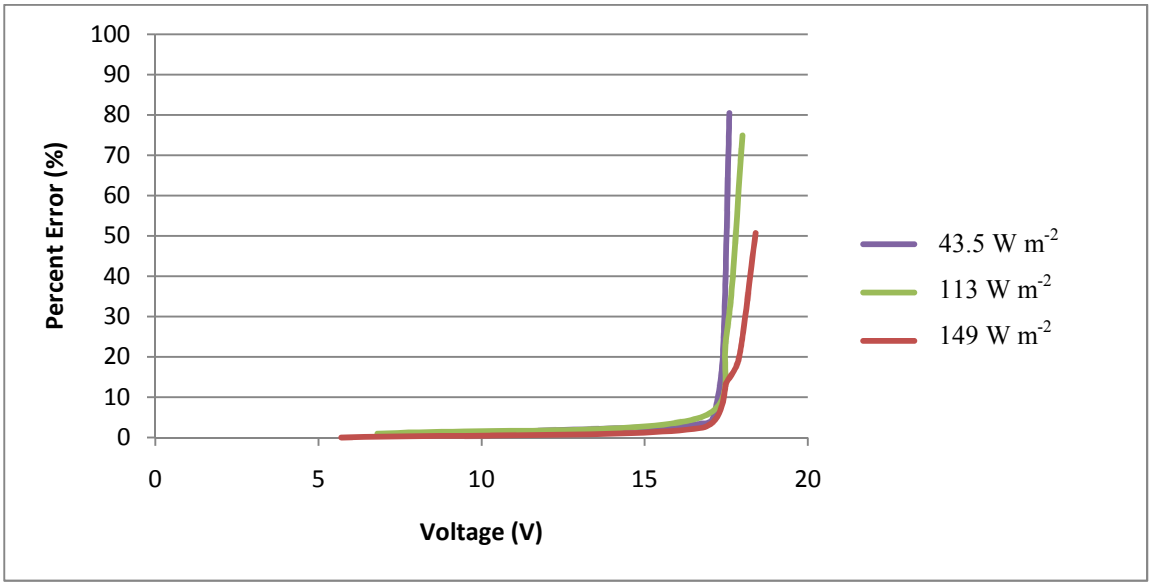

Figure 4-12 Percent Error between Solar Array and Model

4.3 Lead Acid Battery

4.3.1 Model

For the test bench, a lead acid battery was used. As such, lead acid batteries will be modeled. The battery is recognized as one of the most complex component to model in an electrical system simulation of vehicles [26]. For this thesis, a simple yet effective model developed by R.A.Jackey [26] will be implemented in MapleSim 4. This battery model contains three major parts: an equivalent circuit model, a thermal model and a state of charge model. The input of the model is the current and ambient temperature while the outputs are voltage, State of Charge (*SOC*) and electrolyte temperature.

Equivalent Circuit

Figure 4-13 shows the equivalent circuit model used. This equivalent circuit empirically approximates the behaviour seen at battery terminals and does not model the internal chemistry of the lead-acid battery directly. The main branch approximates the battery dynamics and a parasitic branch accounts for the battery behaviour at the end of a charge.

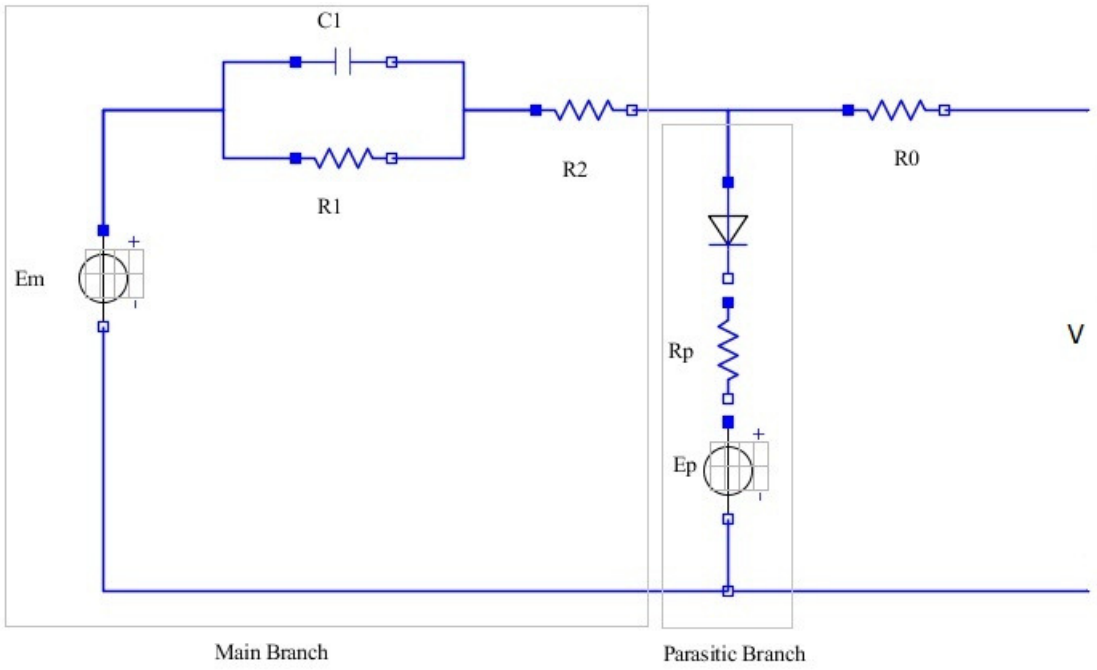

Figure 4-13 Lead Acid Battery Equivalent Circuit Diagram

The equations for each equivalent circuit element are presented as follows:

The internal electromotive force (E_m) or open-circuit voltage of one cell is modeled as

$$E_m = E_{m0} - K_E(273 + \theta)(1 - SOC) \quad \textbf{(4-27)}$$

where $E_{m0}$is the open circuit voltage at full charge in volts, K_E is a constant in volts/°C, θ is the electrolyte temperature in °C, *SOC* is battery state of charge.

The resistance (R_0) seen at the battery terminals was assumed to be independent of temperatures but varies with *SOC* and is approximated as

$$R_0 = R_{00}[1 + A_0(1 - SOC)] \quad \textbf{(4-28)}$$

where $R_0$is resistance in ohms, R_{00} is R_0at *SOC*=1 in ohms, A_0 is a constant.

A resistance (R_1) in the main branch of the battery is approximated by Eqn. (4-29) to vary with the battery's state of charge

$$R_1 = -R_{10}\ln(SOC) \quad \textbf{(4-29)}$$

where R_1 is the main branch resistance in ohms, R_{10} is a constant in ohms

The main branch capacitance (C_1) is approximated to vary with R_1 and a time constant τ_1 which models a voltage delay when battery current changed.

$$C_1 = \frac{\tau_1}{R_1} \quad \textbf{(4-30)}$$

where C_1 is main branch capacitance in Farads and τ_1 is main branch time constant in seconds

A main branch resistance (R_2) varies with the current flowing through the main branch and increased exponentially as the battery *SOC* increased.

$$R_2 = R_{20}\frac{\exp\left[A_{21}(1-SOC)\right]}{1+\exp\left(A_{22}\frac{I_m}{I^*}\right)} \quad \textbf{(4-31)}$$

R_{20} is a constant in Ohms, A_{21} is a constant, A_{22} is a constant, *SOC* is the battery state of charge, I_m is the main branch current in Amps, I^* is the nominal battery current in Amps.

The parasitic current (I_p) is dependent on the electrolyte temperature and the voltage at the parasitic branch. It is modeled as

$$I_p = V_{PN}G_{p0}\exp\left(\frac{V_{PN}/(\tau_p s+1)}{V_{P0}} + A_p\left(1-\frac{\theta}{\theta_f}\right)\right) \quad \textbf{(4-32)}$$

where V_{PN} is the voltage at the parasitic branch in volts, G_{p0} is a constant in seconds, τ_p is a parasitic branch time constant in seconds, V_{P0} is a constant in volts, A_p is a constant, θ is the electrolyte temperature in °C, θ_f is electrolyte freezing temperature in °C.

Thermal Model

The thermal model estimates the battery's electrolyte temperature. Ambient temperature and internal resistive losses both affect the change in electrolyte temperature. The electrolyte temperature is approximated as

$$\theta(t) = \theta_{init} + \int_0^t \frac{(P_s - \frac{(\theta - \theta_a)}{R_\theta})}{C_\theta} d\tau \quad \textbf{(4-33)}$$

where θ_a is ambient temperature in °C, θ_{init} is the battery's initial temperature, P_s is the power loss in watts, R_θ is the thermal resistance in °C/Watts, C_θ was the thermal capacitance in Joules/°C, t is simulation time in seconds.

State of Charge (SOC) Model

Lastly, the state of charge subsystem is used to track the battery's state of charge. To track the amount of charge was extracted from the battery; an integration of the current through the main branch was performed. The extracted charge is described as

$$Q_e(t) = Q_{e\_init} + \int_0^t -I_m(\tau) d\tau \quad \textbf{(4-34)}$$

where Q_{e_init} was the initial extracted charge in Amp-seconds, I_m was the main branch current in Amps, τ was the integration time variable, t was the simulation time in seconds.

The battery's state of charge measures the fraction of charge remaining in the battery. Thus, the state of charge was calculated as

$$SOC = 1 - \frac{Q_e}{C} \quad \textbf{(4-35)}$$

where C was the battery's capacity in Amp-seconds. This value was assumed to be constant.

This lead acid model was implemented in MapleSim and is shown in Figure 4-14. On the top left of the figure are the model's two inputs, current and ambient temperature. The custom component 'Thermal' was created to calculate the electrolyte temperature using Eqn. (4-33). The main branch current I_m, is used as an input to the block 'SOC' to calculate the batteries state of charge according to Eqn. (4-34) and Eqn. (4-35). The six custom component blocks labelled 'computeXXX' were used to calculate each of

the equivalent circuit elements using Eqns. (4-27) - (4-32). These were then used as inputs for the block 'Equivalent Circuit'. This block consists of the battery's equivalent circuit as depicted in Figure 4-13. The parasitic branch is however replaced by block 'I_p' which calculates the parasitic branch current according to Eqn. (4-32). The components 'CS_1' and 'VS_1' are current and voltage sensors respectively.

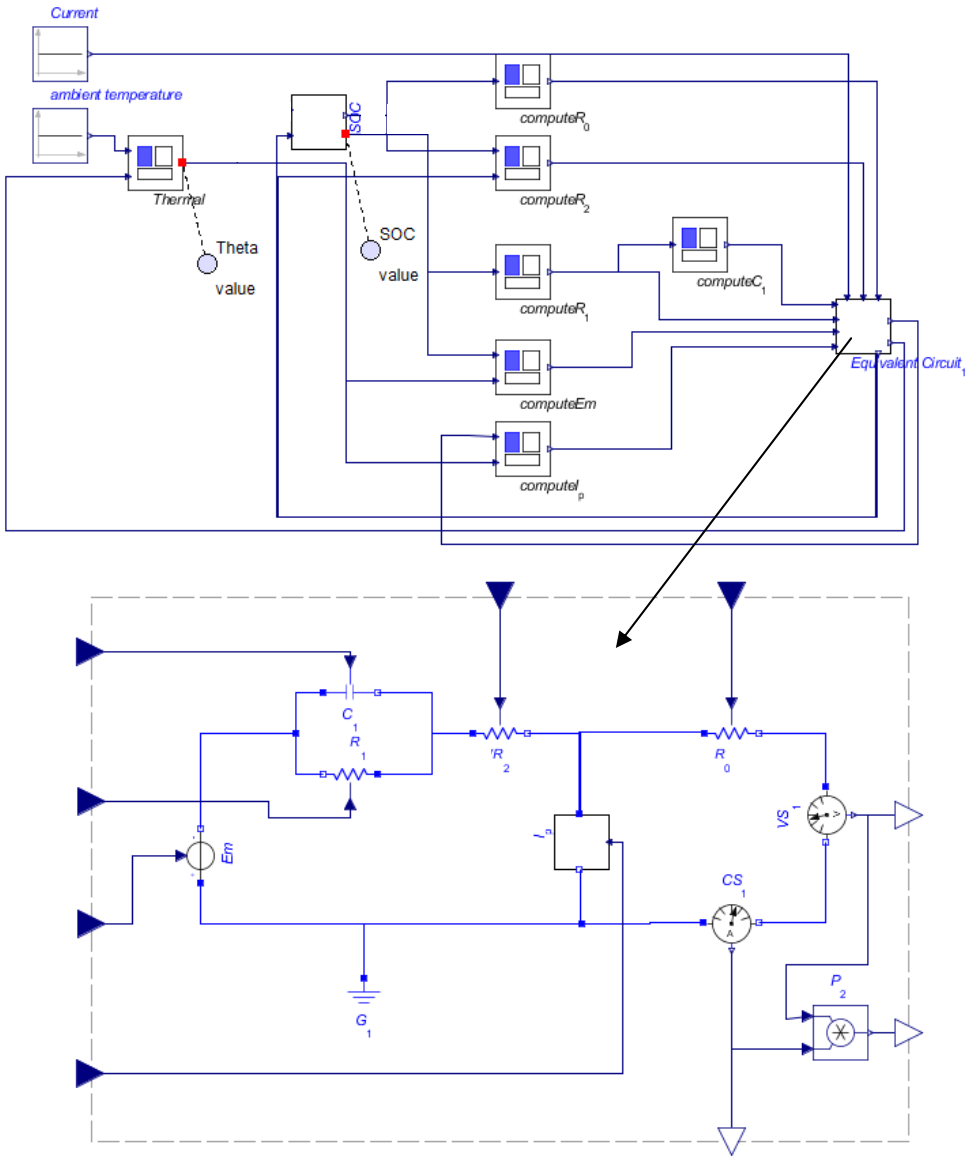

Figure 4-14 MapleSim Model of Lead Acid Battery

4.3.2 Parameterization

Charge/Discharge Curve

The charge/discharge curve of a battery is used to show voltage as a function of time under a variety of different loading conditions. These curves can reveal characteristics of a battery such as battery life, voltage levels and number of usable charge cycles. As a result, charge cycle tests are commonly performed to validate the performance of a battery.

Test Setup

To perform the charge cycle testing, the load simulator will once again be used. The battery was charged with a 6/2A 12V manual battery charger before each test. The load simulator was configured to limit the current to the desired rate of charge. Since a charged battery had a higher voltage than the voltage set point on the load simulator, the current limit was immediately enforced and the load simulator voltage increased to equal the voltage of the battery. In this instance, the battery will discharge and the voltage on both the battery and the load simulator will decrease until the desired un-charged voltage level is reached. The discharge cycle test was performed at three different discharge rates.

Parameters were tuned so that the discharge curve of the model was comparable to that of the batteries on the test bench. Figure 4-15 shows the discharge curve of the tuned model vs. the hardware at three different discharge rates.

Two tests were run at each discharge rate and their results were averaged. It can be seen that for about 70% of each discharge, the results of model and actual battery almost overlap. The majority of the error arises near the end of the discharge, where the physical battery reports a quicker discharge compared to the model. This may be due to the deterioration of the battery's health. It should be noted that since the test setup does not have temperature control, it was not possible to tune the thermal aspects of the model.

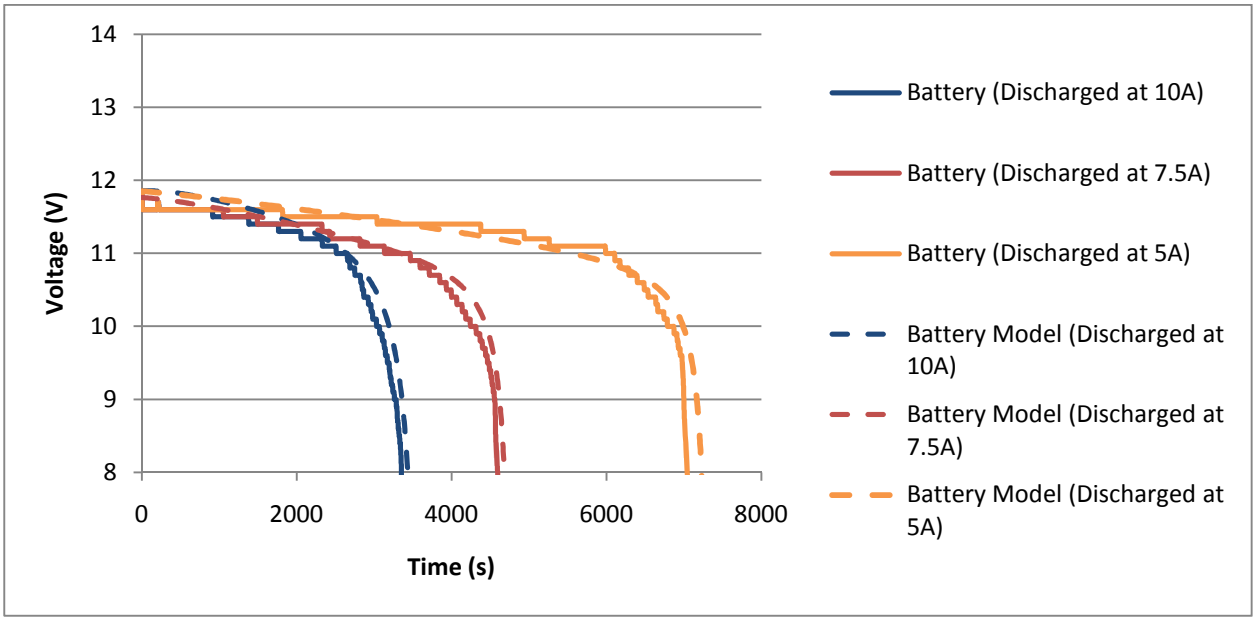

Figure 4-15 Lead Acid Battery Discharge Curve (Hardware Vs Software)

4.4 Motor and Flywheel

4.4.1 Model

For mobility, Spirit and Opportunity each used six Maxon RE0-20 brush motors [2]. However on the test bench, one DC shunt motor was used to represent the energy required to move the entire rover. Accordingly, a DC shunt motor was modeled. It should be noted that the motor used on the test bench does not represent any single wheel motor on a rover. Figure 4-16 shows the equivalent circuit of a DC shunt motor.

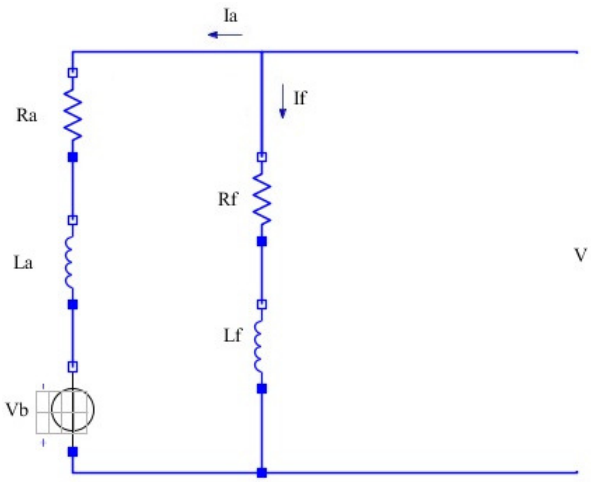

Figure 4-16 DC Shunt Motor Equivalent Circuit

This was used to create a model within MapleSim (Figure 4-17). The input of this model is the applied voltage which is represented by component 'V_b', R_a represents the total resistance of the armature winding, R_f represents the total resistance of the field winding, L_a is the armature inductance and L_f is the field inductance. The component 'Rotational EMF' was connected to the equivalent circuit to transform electrical energy to rotational mechanical energy. The equations for the rotational EMF component are

$$v_{emf} = k_m \cdot \omega \quad \textbf{(4-36)}$$

$$\tau = -k_m \cdot i \quad \textbf{(4-37)}$$

where k is the transformation coefficient in (Nm/A)

The 'Bearing Friction' component represents the total bearing friction in the motor-flywheel assembly. The bearing friction torque τ_{bf} is a function of shaft speed, bearing load, bearing temperature, bearing construction and lubrication used. An assumption has been made in this model that the bearing friction is a function of only the shaft speed. This assumption is acceptable as the bearing load is usually constant and independent of the load torque and all other factors are relatively constant for certain operation conditions. This relationship is defined by a lookup table and can be obtained experimentally.

The 'Rotational Inertia' component was used to represent the inertia of the flywheel. The equation for the rotational inertia component is

$$\tau = I \cdot \alpha \quad \textbf{(4-38)}$$

Where I is the inertia of the flywheel in kgm^2 and α is the angular acceleration in rad/s^2.

The outputs of this model are input current, input voltage, torque and speed. This model is used within a speed controlled feedback loop. Since this is a shunt motor, the field winding is connected in parallel with the armature. Small gauge wires are used for the shunt windings which allows for a higher number of turns. Since the electromotive force is proportional to the number of turns in the coil, a very strong magnetic field can be produced.

The power supplied to the motor can be described by

$$P_{in} = I \times V \quad \textbf{(4-39)}$$

The mechanical power P_{out} is the power reacted by the back emf and can be described by

$$P_{out} = v_{emf} i_a = \tau \times \omega \quad \textbf{(4-40)}$$

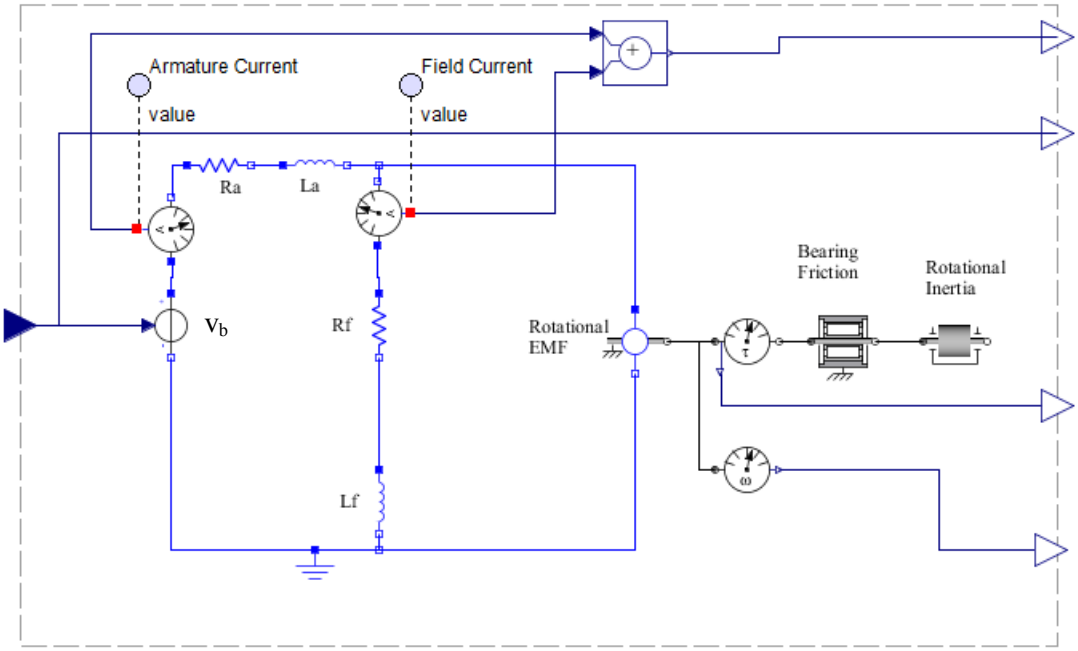

Figure 4-17 MapleSim Model of Motor/Flywheel

4.4.2 Parameterization

With R_a, R_f, L_a *and* L_f being given by the motor's manufacturer, the remaining parameters to be determined are friction losses and k which will be determined experimentally. The power to run the motor at a constant speed (Torque=0) is the motor's power loss. Thus, to characterize the motor-flywheel assembly, the motor was run with the flywheel at 10 different speeds, and parameters were tuned such that power loss vs. speed curve was comparable between the hardware and the model (Figure 4-18). Once again, two sets of data were obtained for each speed and averaged. Figure 4-19 shows the percent error of the model with respect to the experimental data.

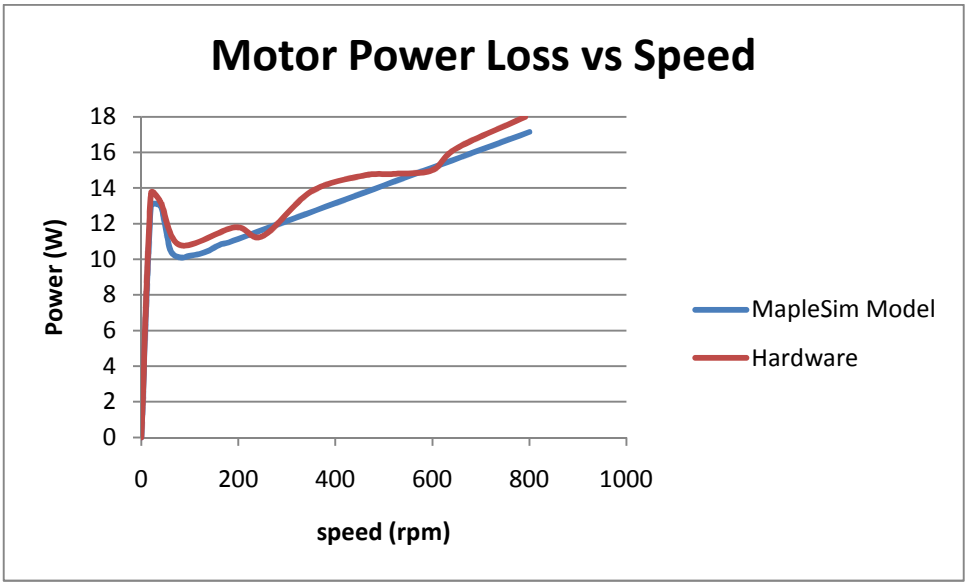

Figure 4-18 Motor/Flywheel Power Loss vs. Speed

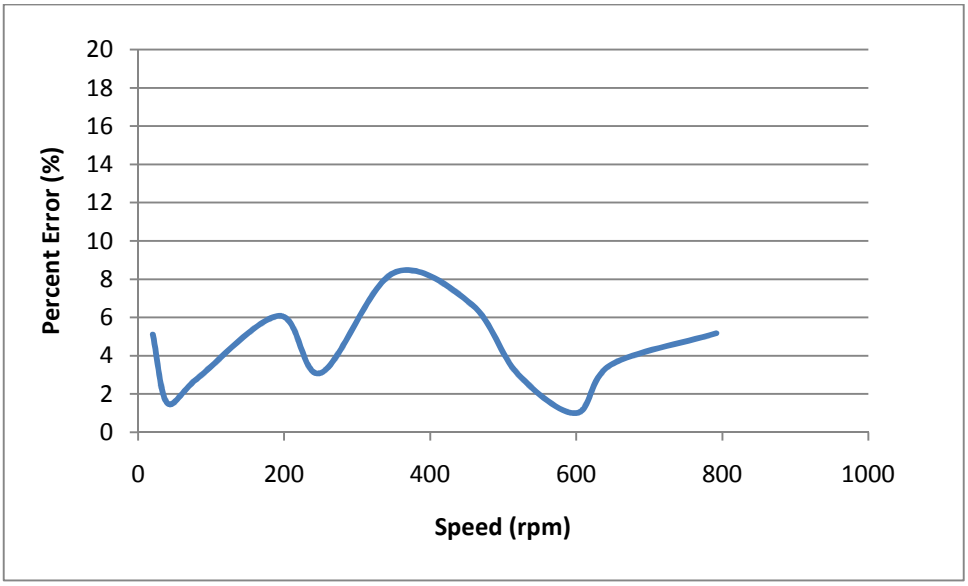

Figure 4-19 Percent Error between Motor and Model

4.5 Auxiliary Power

The primary purpose of the rovers was to search for and characterize a wide range of rocks and soils that hold clues to past water activity on Mars. Hence, the use of science instruments is equally important as enabling technologies like mobility. Power consumption of scientific instruments and communication devices vary throughout its operation. In this work, models were not created to predict the power consumption of the auxiliary devices. Instead, the average power utilization of the devices, as provided in Table 2-1, were applied and assumed to be constant while in operation. This was done with the assumption that as the software library expands, more accurate load profiles of these devices will become available, improving the accuracy of the test platform. Although constant loads were used, the modularity of the test bench allows for any load profile to be utilized.

Attempting to closely mirror possible surface operations, two possible load cycles were created. Figure 4-20 shows a Gantt chart of a possible surface operation schedule for a full activity day and Figure 4-21 shows the day's corresponding power utilization. During the winter months, there are fewer hours in a day with sunlight and the solar intensity is reduced significantly. Thus, typically mission planners reduce the amount of tasks to be completed for these months. Figure 4-22 shows a Gantt chart of a possible surface operation schedule for a reduced activity day and Figure 4-23 shows the day's corresponding power utilization.

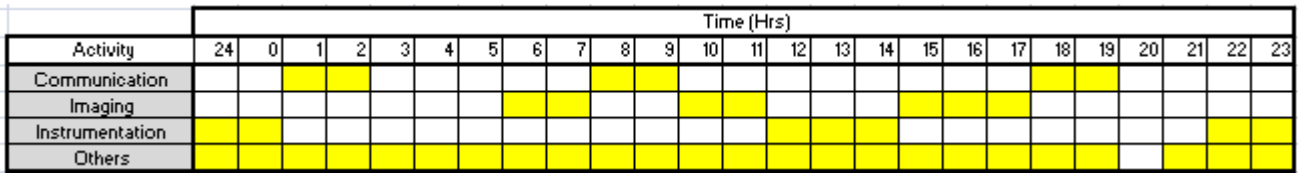

Figure 4-20 Summer - Full Activity Surface Operation Gantt Chart

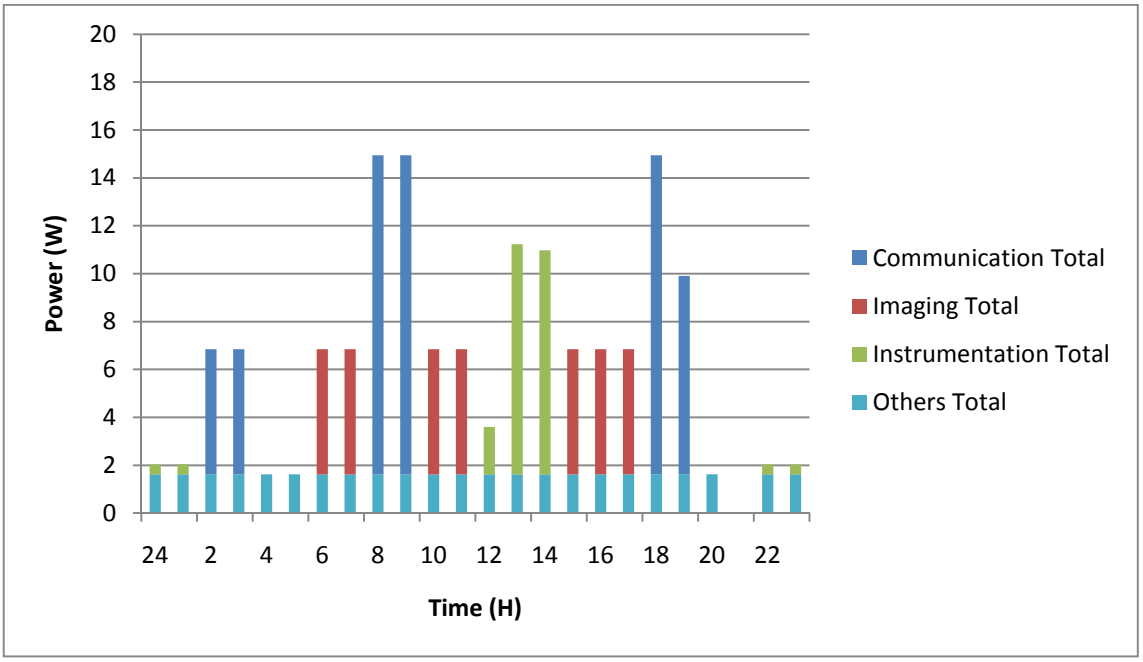

Figure 4-21 Summer - Full Activity Power Utilization Graph

	Time (Hrs)																								
Activity	24	0	1	2	3	4	5	6	7	8	9	10	11	12	13	14	15	16	17	18	19	20	21	22	23
Communication																									
Imaging																									
Instrumentation																									
Others																									

Figure 4-22 Winter -Reduced Activity Surface Operation Gantt Chart

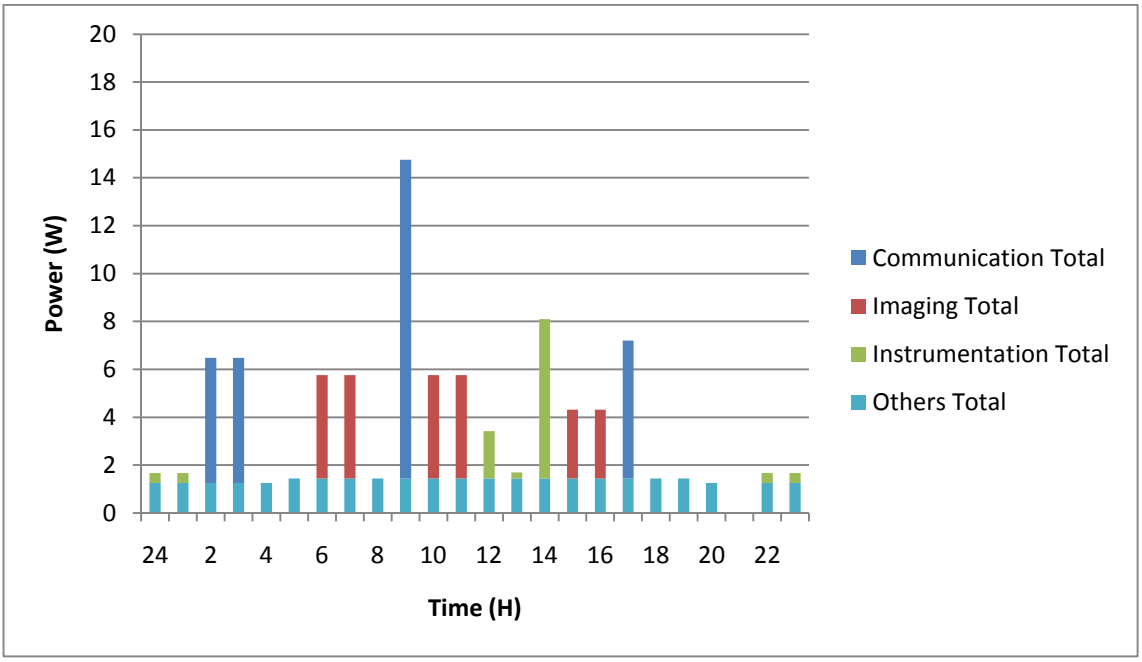

Figure 4-23 Winter - Reduced Activity Power Utilization Graph

Note: The DC-DC Converter and Solar Charge Controller were simply modeled as constant power loss based on their efficiency from their specification sheets (see Appendix A).

A library was created within MapleSim consisting of all the models discussed in this chapter. Users can select different components to be used for their model by simply dragging and dropping the component from the library to the workspace. As the number of components modeled within this library grows, varying types of rovers in different environments can be simulated, providing great flexibility. With all the components modeled, a full vehicle model can be built. The next chapter will discuss how these models were implemented within Labview to work together with the hardware discussed in Chapter 3 for HIL testing.

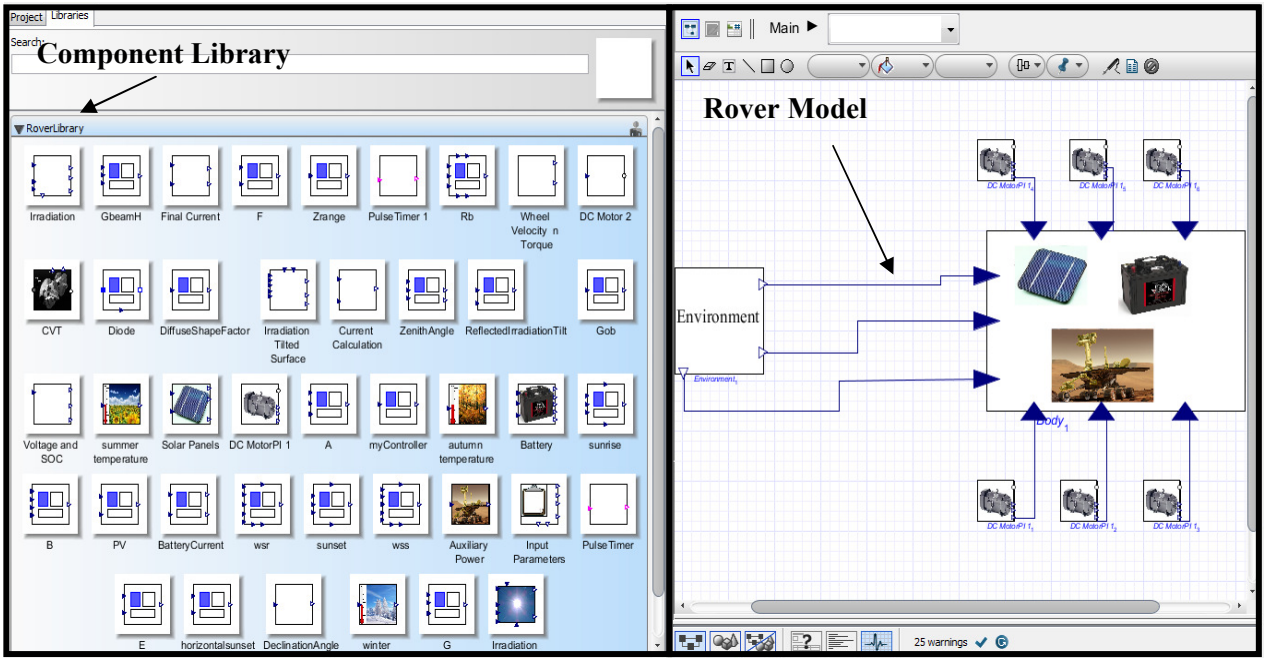

Figure 4-24 MapleSim Component Library and Rover Model

Chapter 5
Hardware-in-the-Loop Implementation

The framework of the hardware in the loop simulation is depicted in Figure 5-1. Using the path planning optimization and the rover dynamics model, the vehicle's position, orientation, tilt, speed and mobility power consumption were calculated. These were used as inputs to the models created within MapleSim (described in Chapter 4). To incorporate the hardware components, communication between the software and hardware has to be established thus the MapleSim models were imported individually within the Labview Real-Time environment. Labview Real-Time is crucial to this test platform as it has timing functions to precisely control the execution of loops and communicate data deterministically between parts of real time programs. Within LabView Real-Time, a program consisting of the rover's powertrain model, controls and sensor measurements for the hardware components, and a Graphical User Interface (GUI) for the HIL testing was created. This program was uploaded to the embedded computer within National Instruments PXI where the real time simulation is run and communication between the hardware components and the software model is established. The following sections describe the real time program within LabView as well as the GUI for the HIL testing.

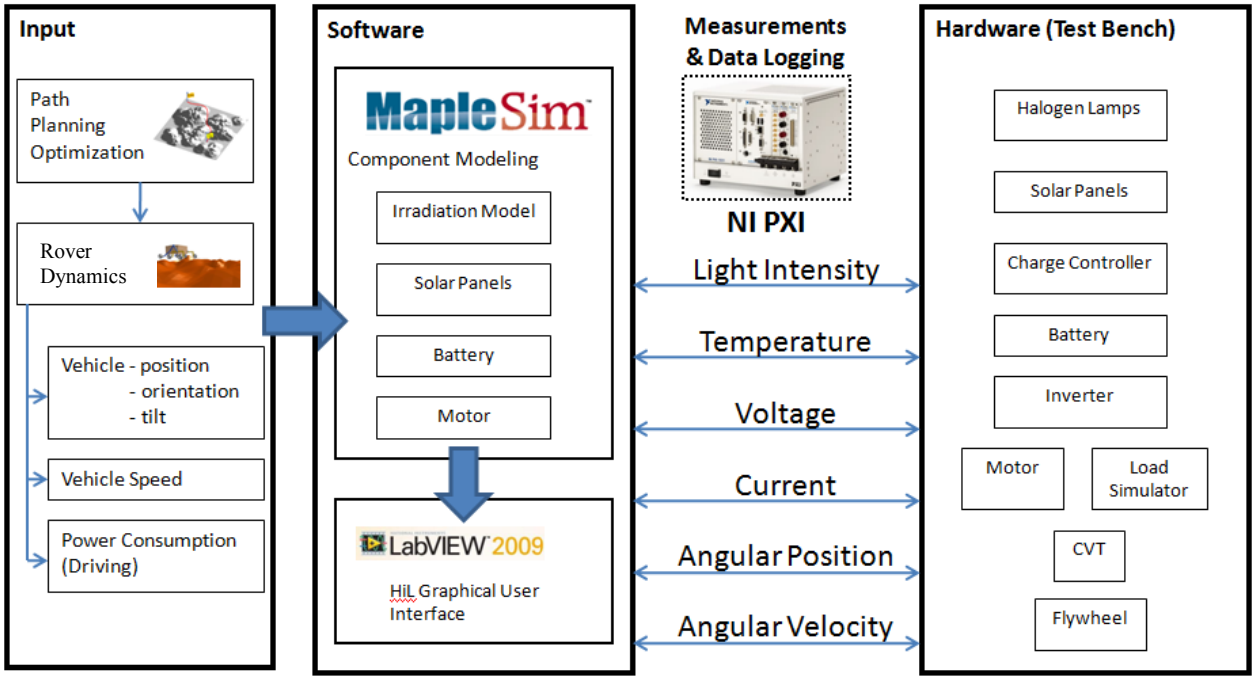

Figure 5-1 HIL simulation Framework

5.1 Vehicle Program

Every program written in LabView consists of two components; one being the Virtual Instrument (VI) block diagram where the source code is developed, the other being the front panel where the GUI for the program is developed. In this section, the block diagram of the program will be described. Section 5.2 will describe the GUI of the program.

The program consisted of two simulation loops. The purpose of the first loop was for input generation. Information regarding vehicle position, orientation, tilt and speed were stored as Excel files and were extracted in the form of lookup tables within the program. Vehicle position, orientation and tilt were used as inputs to the MapleSim irradiation model (as shown in Figure 5-2) to generate an irradiation profile for the simulation. A desired speed profile and an auxiliary load profile were also extracted from the Excel files. These generated profiles were stored in arrays to be used by the second loop. Since the first loop was used purely for generating inputs, it was not synchronized with a timing source. Running this loop without any timing restrictions allows for the fastest possible runtime. The second simulation loop, on the other hand, was used to perform real-time HIL testing and was thus synchronized with a 1 kHz clock.

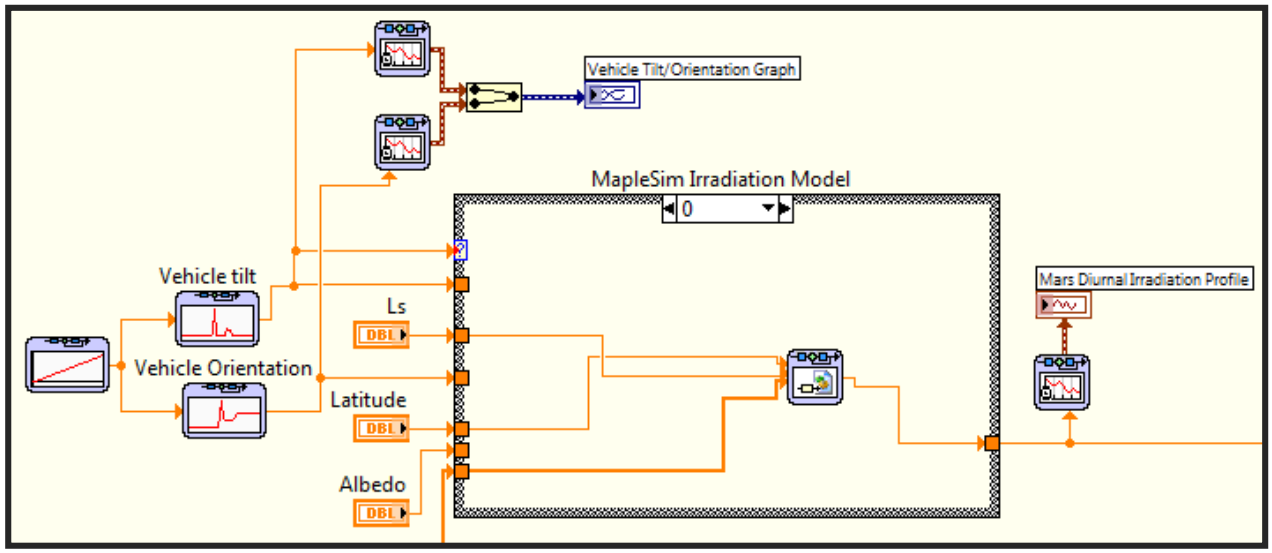

Figure 5-2 MapleSim Irradiation Model within Labview

The second loop contains all the MapleSim powertrain component models, controls the lighting and motor and performs all the data logging. The irradiation profile generated from the first loop was used to control the duty cycle for the PWM lighting control (Figure 5-3). Eqn. (3-1) was used to relate the

irradiation to the duty cycle. A PWM signal was created by producing a simple digital pulse train in terms of frequency and duty cycle. At the beginning of every iteration, the duty cycle was checked and if changed, the new duty cycle was set using the DAQmx Write VI function within LabView. Otherwise, the false case of the case structure executed and nothing was updated.

Eqn. (3-1) Relationship between
Irradiaition and Duty Cycle

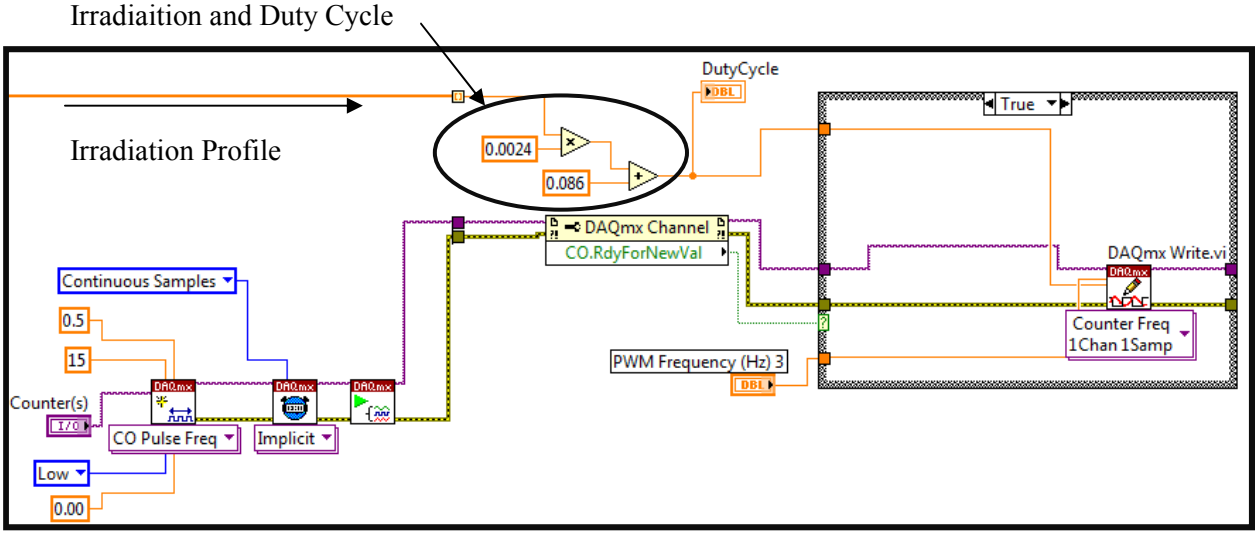

Figure 5-3 PWM Lighting Control in LabView

The irradiation profile was also used as an input to the solar array model. Figure 5-4 shows the MapleSim model of the solar array imported within LabView. The output of this model is the power generated signal. The auxiliary load profile from the first loop is used as an input to control the electronic load simulator. The control of the load simulator was done using a Labview VI which was supplied by the load simulator manufacturer Sorensen [27]. Figure 5-5 shows the portion of the program which controls the throttle for the DC motor. The angular position of the flywheel is recorded and the angular velocity is calculated. This is fed to Labview's Proportional-Integral Control SubVI which then outputs the necessary throttle signal.

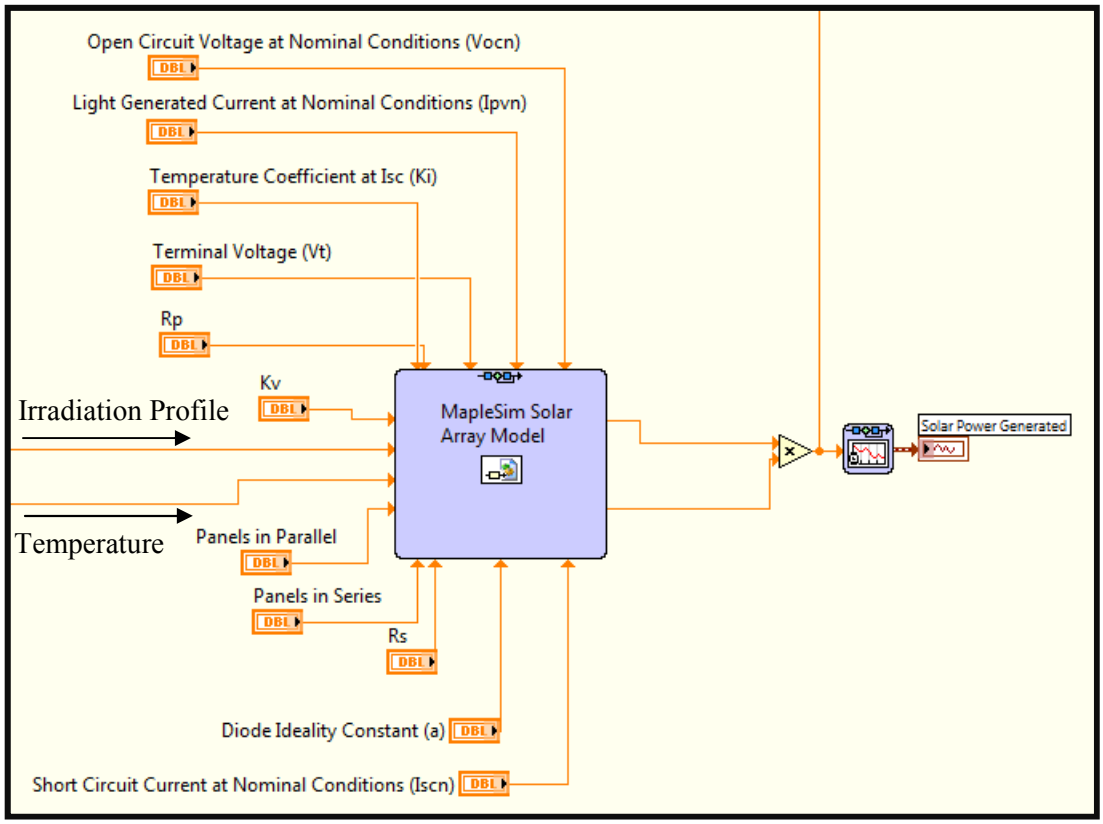

Figure 5-4 Maplesim Solar Array Model in LabView

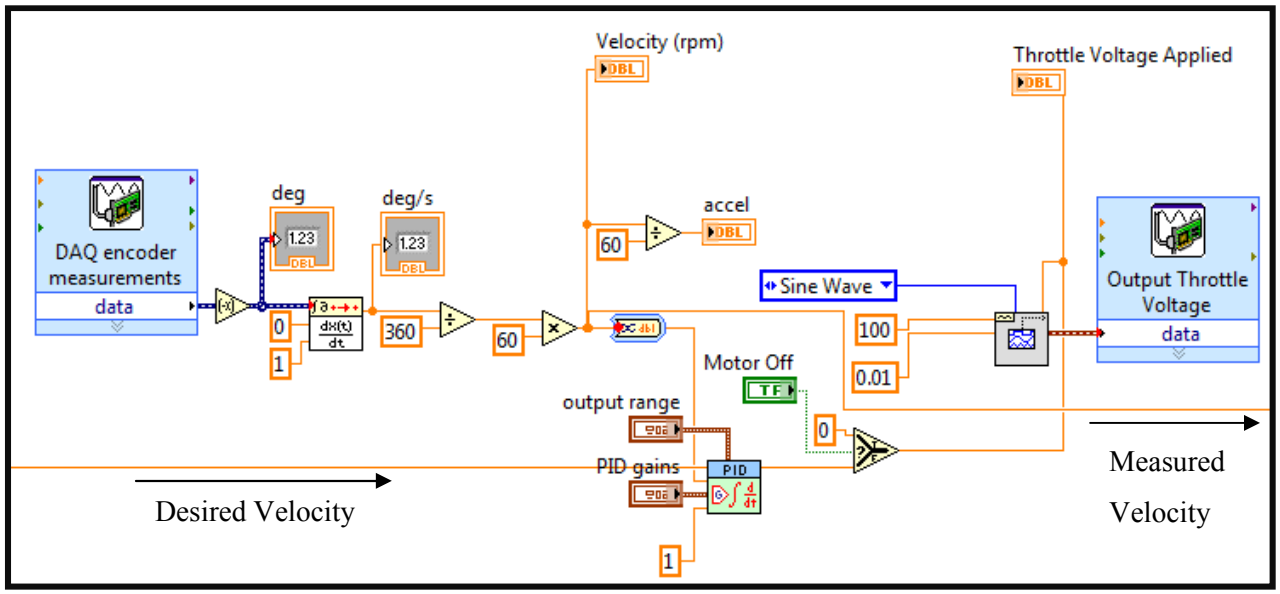

Figure 5-5 Motor Control in LabView

Like the previous components, the MapleSim battery model was imported within Labview. It takes the net current and ambient temperature and outputs the battery SOC, electrolyte temperature as well as current and voltage. Figure 5-6 shows the data acquisition portion of the program. Calibration factors discussed in Chapter 3 were applied here for each sensor.

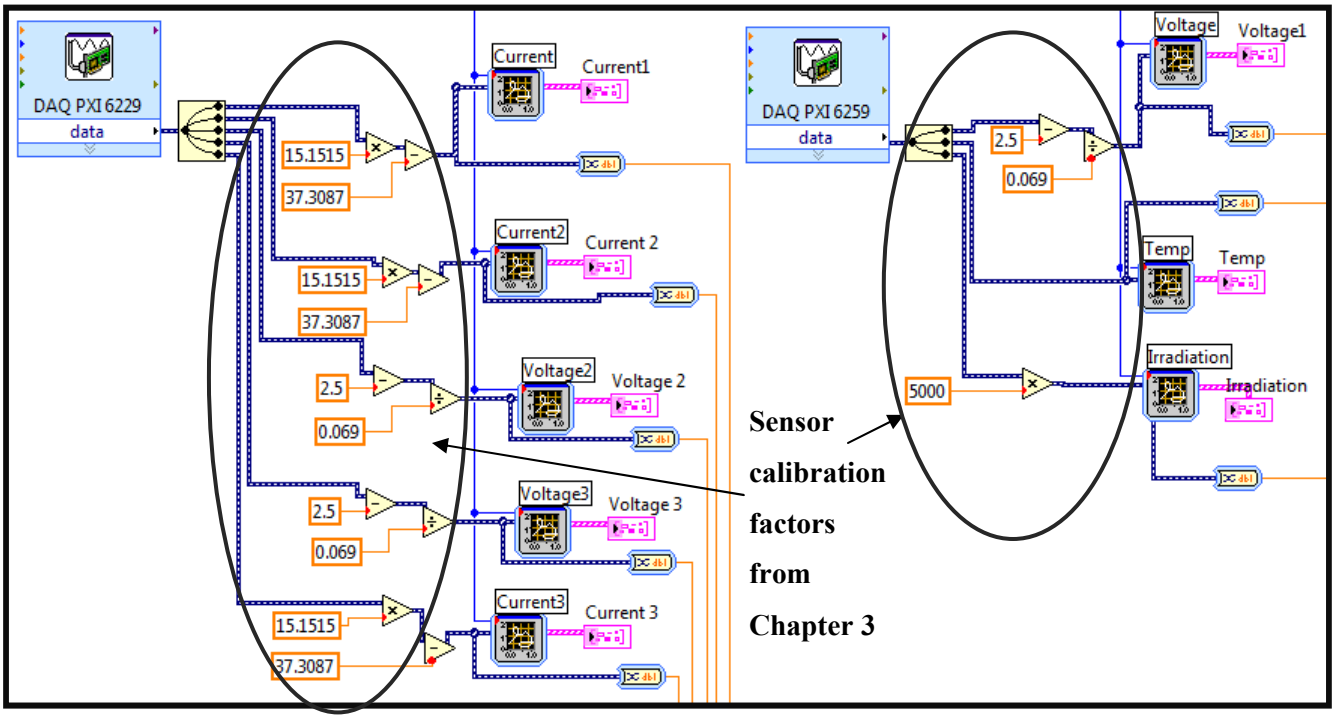

Figure 5-6 Data Acquisition in Labview

As hardware components become available, their models are replaced with the hardware as well as the associated sensors for data acquisitioning. Thus, depending on which hardware components are added to the simulation, different portions of the second loop are activated/ deactivated. This is done through a case structure within LabView. For example, if the solar arrays were available for testing , the irradiation profile from the environment loop was used to control the duty cycle of the PWM controlled lighting system, the solar array model was deactivated and corresponding sensors were activated to perform data acquisitioning from the hardware. On the other hand, if solar arrays were unavailable for testing, the solar array model were activated with its input being the generated irradiation profile and the corresponding

sensors were deactivated. When all hardware is available, all the models were deactivated while all sensors were activated.

5.2 LabView GUI

This program also provides a Graphical User Interface (GUI) where users can change any of the design parameters on each modeled component, define simulation parameters as well as view simulation results in real-time. The GUI (shown in Figure 5-7), was divided into 4 parts. The first plot in part 1 plots the vehicle's tilt and orientation while the second one plots the predicted irradiation (from irradiation model) as well as the real time information on the actual radiation level as measured by the pyranometer. The last plot shows the auxiliary power consumption which is either directly from a lookup table or from actual sensor measurements of the load simulator, depending on the test. By selecting the Test Parameter tab at the top, the simulation parameters are displayed and can be changed (Figure 5-8). In this section, the user can select which hardware component is connected for testing, information regarding the environment, hardware information regarding the lighting system and the load simulator as well as the output files of the simulation.

Section 2 shows the solar panel output (current and voltage) if solar panels are connected, otherwise it will display the solar panel model's outputs. If the solar panel model is used, parameters for the model are displayed and can be modified in the parameters section (Figure 5-8).

Section 3 shows the battery's state of charge, the charging or discharging current and a charging/discharging indicator if the battery's connected. Otherwise, the battery model is used and results from the model are displayed. If the model is used, parameters for the model are displayed and can be modified in the parameters section (Figure 5-8).

If the motor is connected, Section 4 shows the power consumed by the motor and its angular velocity otherwise it will display the motor model's outputs. If the motor model is used, parameters for the model are displayed and can be modified in the parameters section (Figure 5-8).

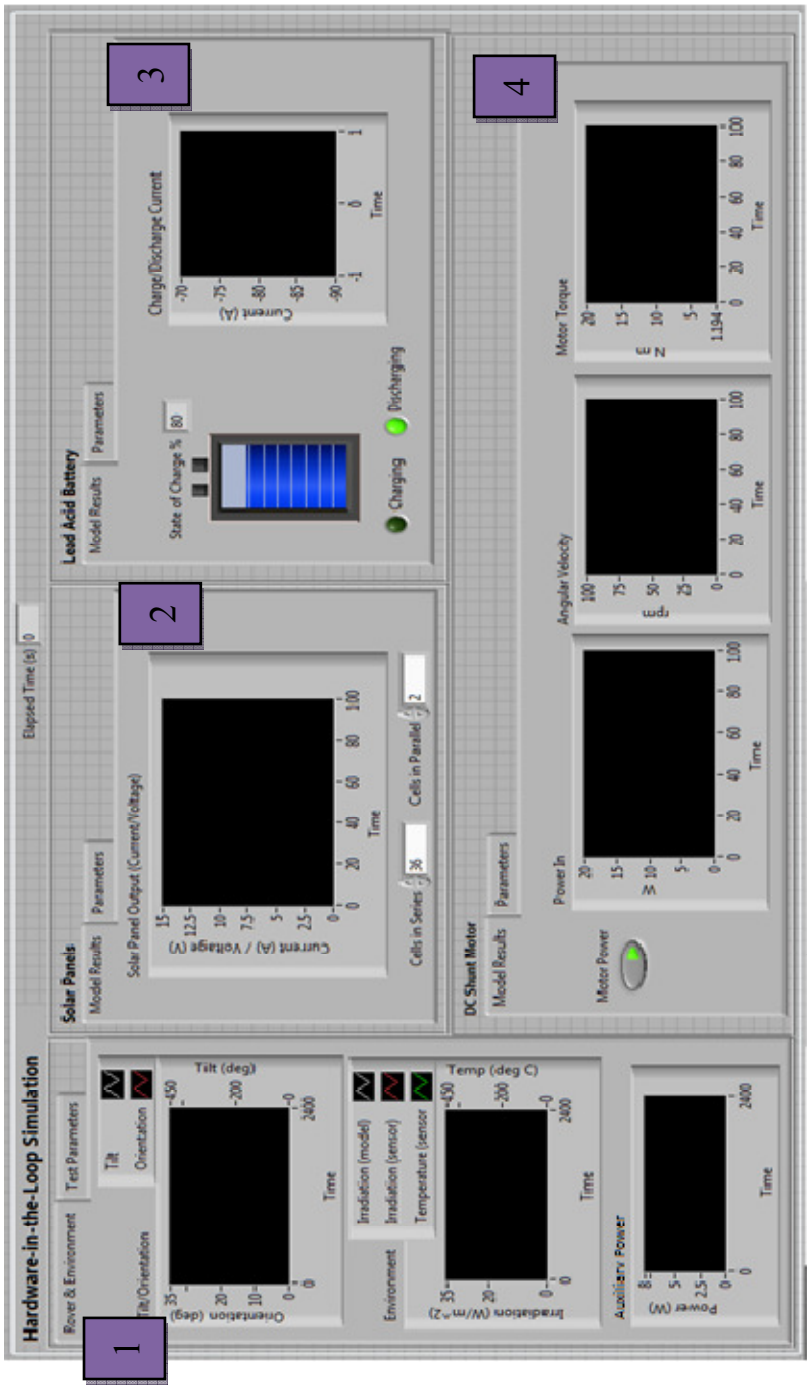

Figure 5-7 HIL GUI –Real Time Plots

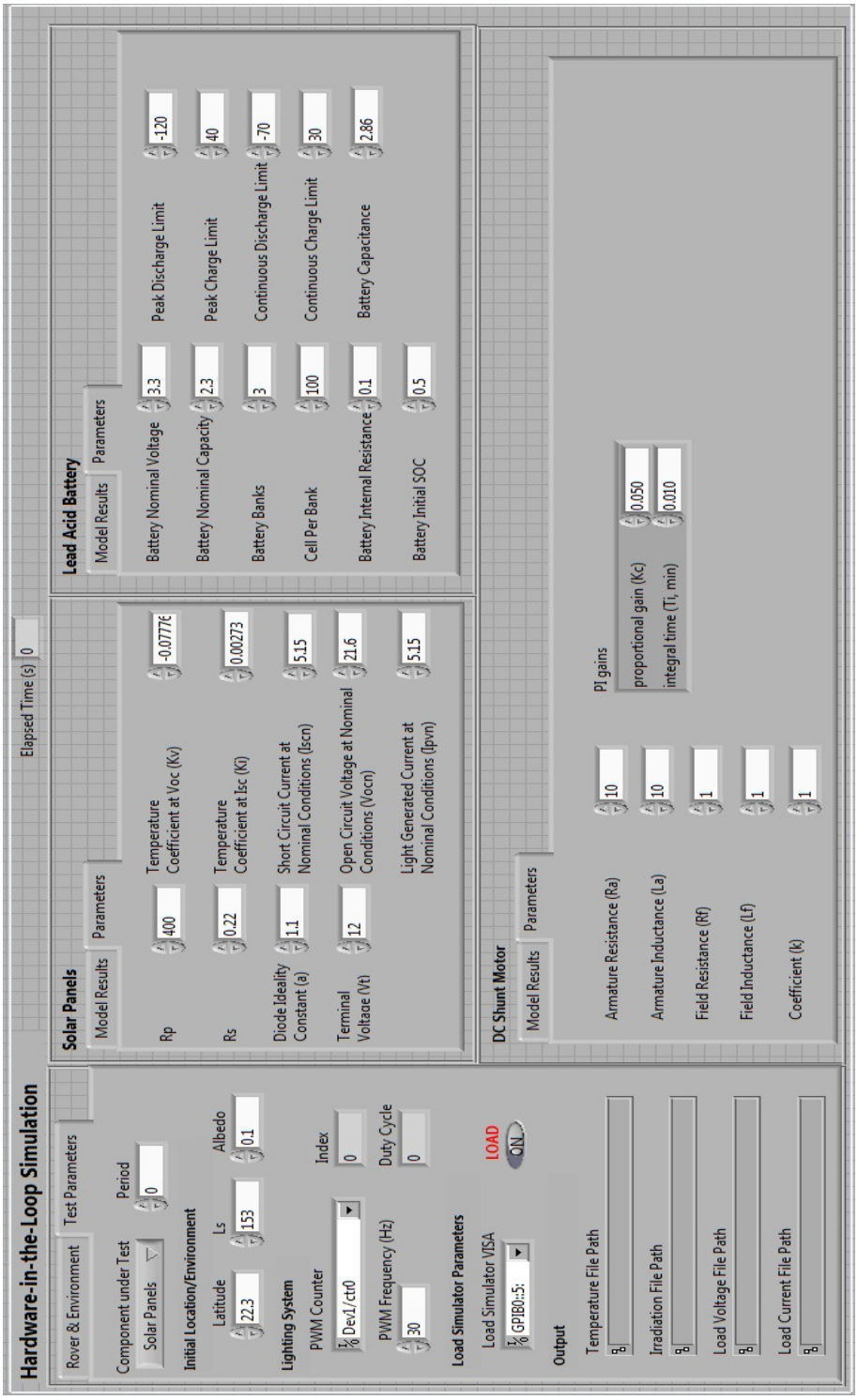

Figure 5-8 HIL GUI Parameter Inputs

5.3 Signal Scaling

The hardware components used on the test bench were selected based on the size of the system; however, in a real HIL testing application where novel or prototype hardware is being tested, it may be necessary to scale the signals in and out of the prototype system to represent the system's actual size. Especially in the space industry, construction of a full-sized prototype can be expensive (e.g. a triple junction solar cell vs. a triple junction solar array). A scaling technique based on Buckingham's Pi Theorem [28] can be used in a HIL application to obtain scaling factors which ensure dynamic similarity between systems. This technique was applied successfully in an HIL application for hybrid-electric vehicle powertrain components [29] as well as in other applications [30][31][32]. This technique will be explained in the following section.

Dimensional analysis, a technique used to find or verify relations of physical quantities by using their dimensions, has its roots in work by Euler, Newton, Fourier, Maxwell and Rayleigh. Their work led to the method of dimensional scaling which was formalized in the Buckingham Pi theorem. This theorem is based on the idea that if there is a physical process, such as $a + b = c$, where every term has the same units, then each term can be divided through to get an expression without any units, $\frac{a}{c} + \frac{b}{c} = 1$. The terms $\frac{a}{c}$ and $\frac{b}{c}$ are dimensionless and represent nothing in the real world, however it allows for a reduction in parameters to describe the physical process. These dimensionless terms are called pi groups. The steps to finding the pi groups are outlined in Appendix E.

If the pi groups used to describe the physical system are equivalent between two systems, then it is said that they are dynamically similar. In this manner, Buckingham's Pi Theorem can be used to obtain scaling factors which ensure dynamic similarity between systems. For example, one prototype solar cell can be tested in a HIL environment to estimate the performance of an entire solar array on a rover. The method of obtaining scaling factors to ensure dynamic similarity will be illustrated with a battery. The dynamic system equations of a battery using a simple lumped model are

$$V_T = n_{cells,s}(V_{OC} - I \times R_{int}) \quad \textbf{(5-1)}$$

$$\dot{SOC} = \frac{SOC}{\tau} = -\frac{1}{Q}I \quad \textbf{(5-2)}$$

To apply the dimensionless variable method, six steps are involved [28].

Step 1: determine the number of system parameters *n*

n=7 =>*Q, V_{oc}, R_{int}, I, V_t, τ, V_{nom}* (since $n_{cells,s}$ is already dimensionless, it is excluded in the list)

Step 2: List the dimensions of each parameter

Q	V_{oc}	R_{int}	I	V_t	τ	V_{nom}
sA	$m^2kgs^{-3}A^{-1}$	$m^2kgs^{-3}A^{-2}$	A	$m^2kgs^{-3}A^{-1}$	s	$m^2kgs^{-3}A^{-1}$

Step 3: Determine *m* and Q_{pi}.

m=3 => m^2kg, s, A (since m^2kg always appear together, the two can be combined into a new composite dimension)

Q_{pi}=*n-m* =7-3=4 => 4 pi groups

Step 4: Choose *m* scaling parameters, ensuring their product contains all the dimensions of the system.

$$Vnom * Rint * \tau = [m^2kgs^{-3}A^{-1}][m^2kgs^{-3}A^{-2}][s] = [m^2kg]^2[s]^{-5}[A]^{-3} \quad \textbf{(5-3)}$$

Step 5: Add one additional parameter to the *m* repeating parameters to form a power product. Algebraically find the exponents that make the product dimensionless. Repeat this Q_{pi} times to form Q_{pi} pi groups.

$$\pi_1 = QV_{nom}{}^a R_{int}{}^b \tau^c \quad \textbf{(5-4)}$$

$$[A]^0[m^2kg]^0[s]^0 = (sA)(m^2kgs^{-3}A^{-1})^a(m^2kgs^{-3}A^{-2})^b(s)^c$$

Solving for *a, b, c*, we obtain, *a*=-1, *b*=1, *c*=-1 and thus,

$$\pi_1 = \frac{QR_{int}}{V_{nom}\tau} \quad \textbf{(5-5)}$$

Continuing in a similar manner, we obtain the remaining pi groups (Appendix F for detail)

$\pi_2 = \frac{V_{OC}}{V_{nom}}$ $\pi_3 = \frac{IR_{int}}{V_{nom}}$ $\pi_4 = \frac{V_T}{V_{nom}}$

The resulting pi groups, including the number of cells $n_{cells,s}$ and the state of charge *SOC*, are given in Table 5-1.

Table 5-1 Scaling Pi Groups

Dimensionless variable	Variable grouping
π_1	$\frac{QR_{int}}{V_{nom}\tau}$
π_2	$\frac{V_{OC}}{V_{nom}}$
π_3	$\frac{IR_{int}}{V_{nom}}$
π_4	$\frac{V_T}{V_{nom}}$
π_5	$n_{cells,s}$
π_6	$S\dot{O}C\tau$

Step 6: Write the final dimensionless function

$$V_T = n_{cells,s}(V_{OC} - I \times R_{int})$$

$$\frac{V_T}{V_{nom}} = n_{cells,s}\left(\frac{V_{OC}}{V_{nom}} - \frac{I \times R_{int}}{V_{nom}}\right) \quad \textbf{(5-6)}$$

$$\pi_4 = \pi_5(\pi_2 - \pi_3)$$

$$S\dot{O}C = -\frac{1}{Q}I \quad \textbf{(5-7)}$$

$$\tau S\dot{O}C = -\frac{\tau v_{nom}}{QR_{int}}\frac{IR_{int}}{V_{nom}}$$

$$\pi_6 = -\frac{\pi_3}{\pi_1}$$

From Eqn. (5-6) and Eqn. (5-7), π_4 and π_6 are equivalent between two systems as long as π_1, π_2, π_3 and π_5 are equivalent. By definition, any ratio of dimensionless variables can also be defined as a pi group. Thus, we can define $\pi_7 = \frac{\pi_2}{\pi_5}$. For dynamic similarity, the following scaling equivalency

(Table 5-2) must be applied with the additional requirement of $\pi_{1,s} = \pi_{1,h}$. The subscripts *s* and *h* denotes software and hardware respectively.

Table 5-2 Scaling Equivalency

Hardware	Software
I_h	$I_s \frac{R_{int,s} \times V_{nom,h}}{R_{int,h} \times V_{nom,s}}$
V_s	$V_h \frac{V_{nom,s} \times n_{cells,s,s}}{V_{nom,h} \times n_{cells,s,h}}$

Figure 5-9 shows a schematic diagram showing how scaling would be used. The current signal generated from the software model would be multiplied by a scaling factor $\alpha = \frac{R_{int,s} \times V_{nom,h}}{R_{int,h} \times V_{nom,s}}$. This current would be applied from a programmable power supply to the physical battery. The voltage that is measured across the battery would be scaled by a factor of $\beta = \frac{V_{nom,s} \times n_{cells,s,s}}{V_{nom,h} \times n_{cells,s,h}}$. This scaled voltage signal would be fed back to the software model. Scaling can be easily applied to signals however, in an actual HIL application, scaling of parameters that are not inputs or outputs will be based on the construction of the HIL hardware component. In this example, on top of the scaling factors, the values for $\pi_1 = \frac{QR_{int}}{V_{nom}\tau}$ must also be equal. If both batteries had the exact same construction and chemistry then V_{nom} and τ should be equal. Therefore, in order for the two system's π_1 value to be equal, the ratio of Q must be the inverse of the ratio of R_{int}.

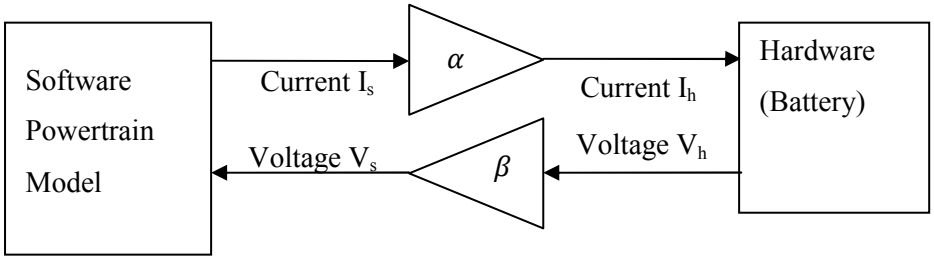

Figure 5-9 Schematic Diagram of Scaling Process (α and β are scaling factors)

Chapter 6
Simulations and HIL Experimental Results

Using the pure software powertrain model, simulation was run under full load in summer conditions. The result (Figure 6-1) shows the power generated by the solar panels given a reasonable vehicle orientation and tilt profile, the power consumed for instrumentation and mobility and the battery SOC throughout a Martian day. From midnight to sunrise, power is consumed while no sunlight is available. Accordingly, the battery's SOC is steadily decreasing. As the power generated overtakes the power consumed, the battery's SOC begins to dip and rise until an upper limit for charging is reached. As the sun sets, the power consumed is once again higher than the power generated and the battery's SOC begins to drop. Every time the power generated curve and power consumed curve intersect, the battery's SOC curve changes direction.

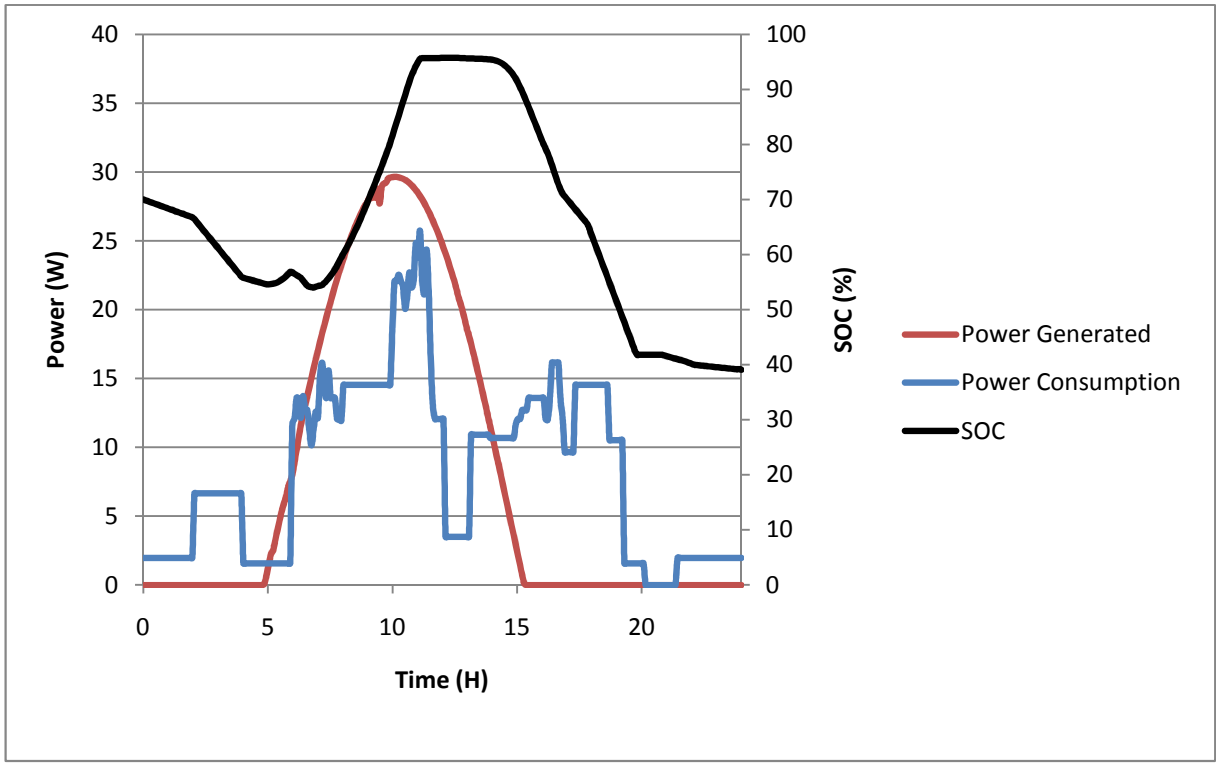

Figure 6-1 Summer Full Load - Pure Software

Next, a test was run using all the hardware on the test bench as described in Chapter 4 and the results are shown in Figure 6-2. We can see a similar general trend for the power generation, consumption and battery SOC between the software models and the hardware test results. However, at the end of the day, the software model estimated a battery SOC of 39% where in reality, the hardware shows a battery SOC of 24%. The discrepancy between the software simulation and the hardware test is evident and shows the importance of incorporating hardware in power level estimation as component modeling errors accumulate within a system.

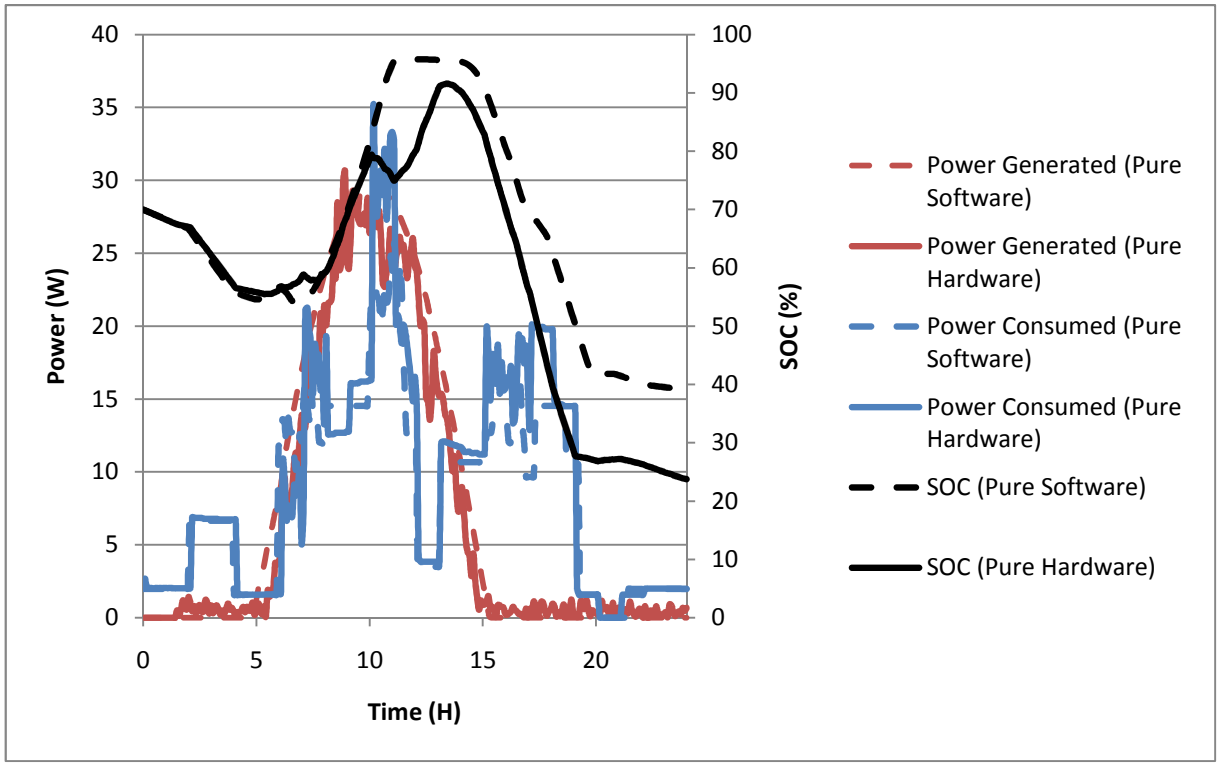

Figure 6-2 Summer Full Load - Pure Hardware vs. Pure Software

To demonstrate the ability to estimate power levels without all the hardware components, two more tests were run; first with solar arrays in the loop and the second with solar array, load simulator and motor in the loop.

In the first test, the solar array's output measurements (current and voltage) were fed in to the software powertrain model where $I_{solar}xV_{solar}$-$P_{loss\text{-}chargecontroller}$=$P_{generated}$. The solar array component within the software model has been deactivated. Also, the load simulator was used to absorb the power generated. The results are shown in Figure 6-3.

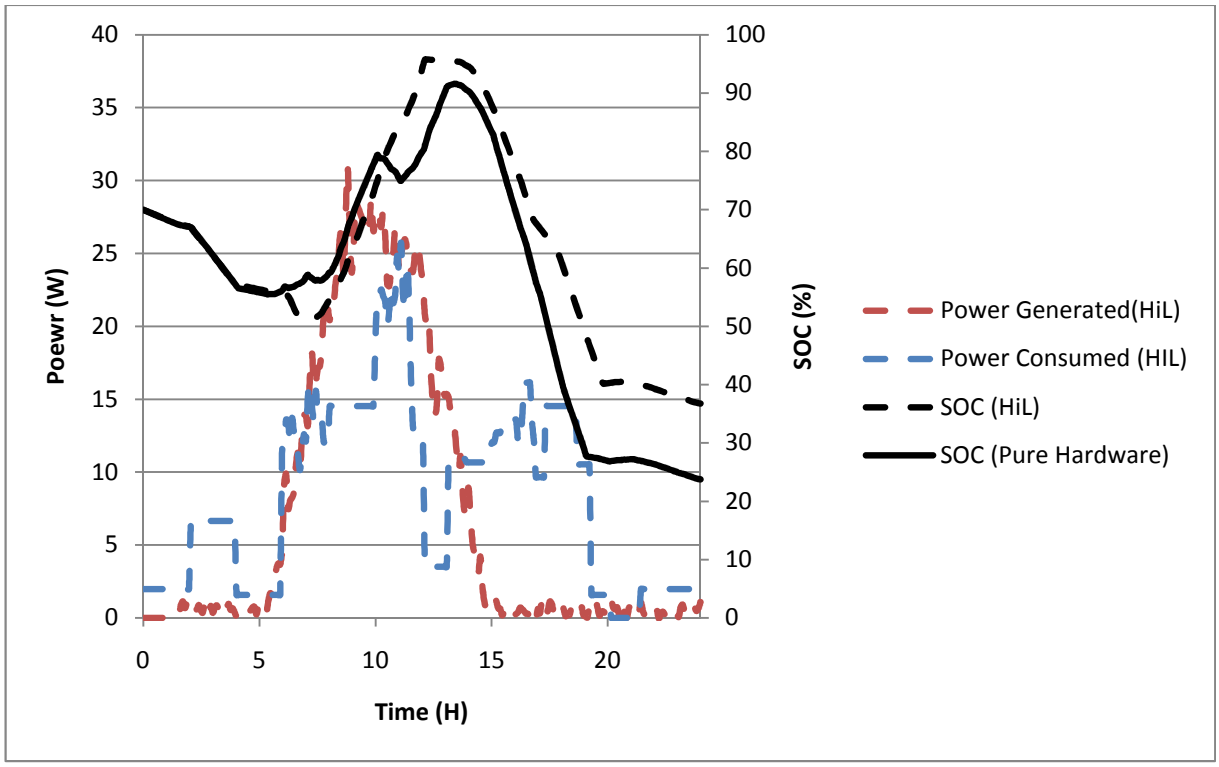

Figure 6-3 Summer Full Load - Pure Hardware vs. Solar Panel in the Loop

In the second test, the solar array's output measurements were used in the same manner as the first test. This time, it was connected to a battery through the charge controller for absorbing the power generated. The load simulator is programmed to draw the power used for instrumentation and other auxiliary devices while a constant power supply is used to power the motor connected to the flywheel. Again, the current and voltage measurements were fed in to the software powertrain model however this time, only the battery model is activated in the simulation. The results are shown in Figure 6-4.

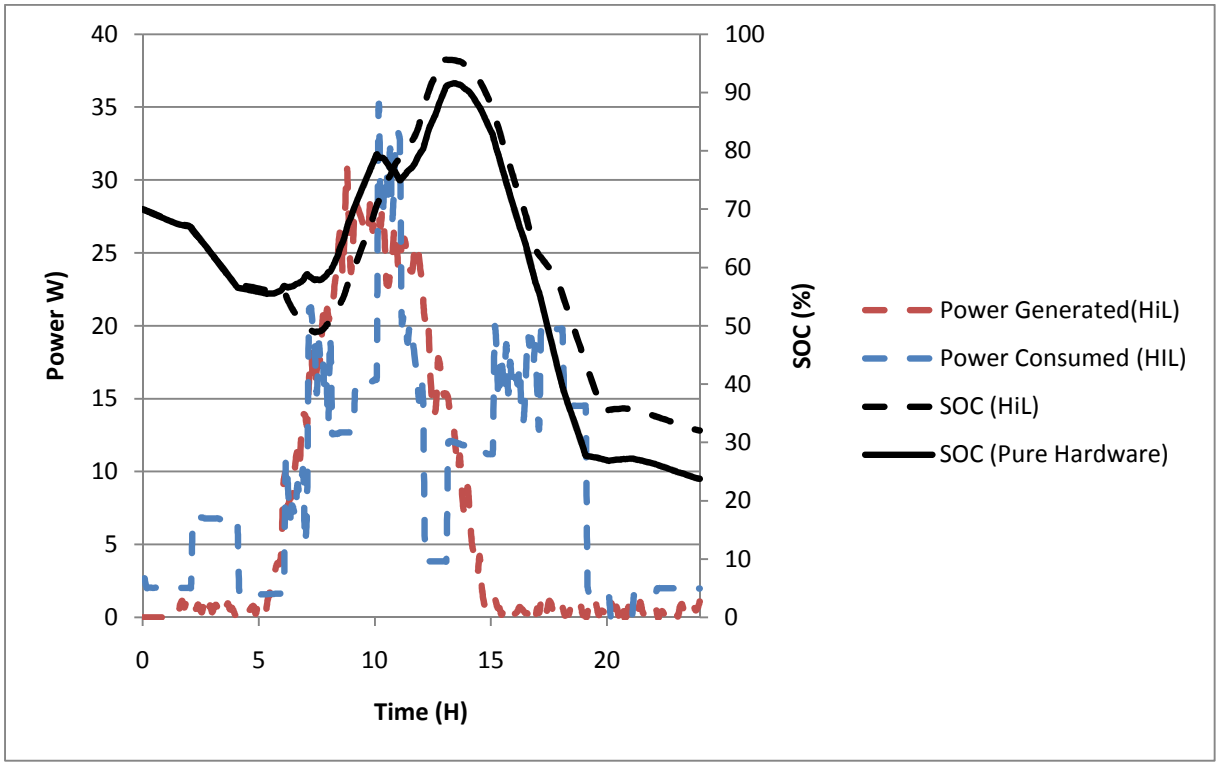

Figure 6-4 Summer Full Load - Pure Hardware vs. Solar Panel, Motor, Load Simulator in the loop

In both cases, the power level was compared to the pure hardware case by looking at the battery SOC. In Figure 6-4, only the battery was modeled and as expected, the results of this HIL testing matched more closely with the pure hardware test compared to the pure software simulation. The results show that as more hardware components are added, the power level estimation became more accurate.

To demonstrate the test bench's power estimation capabilities, several drive cycles and scenarios were created and tested. As mentioned, seasonal effects on the power generation of a solar powered rover can be significant. Thus, the winter and summer conditions were created where summer is expected to allow a much greater amount of power generated. For the winter scenario, the driving and communication loads are shifted to begin later in the day and end earlier in the day to accommodate for the change in hours of sunlight.

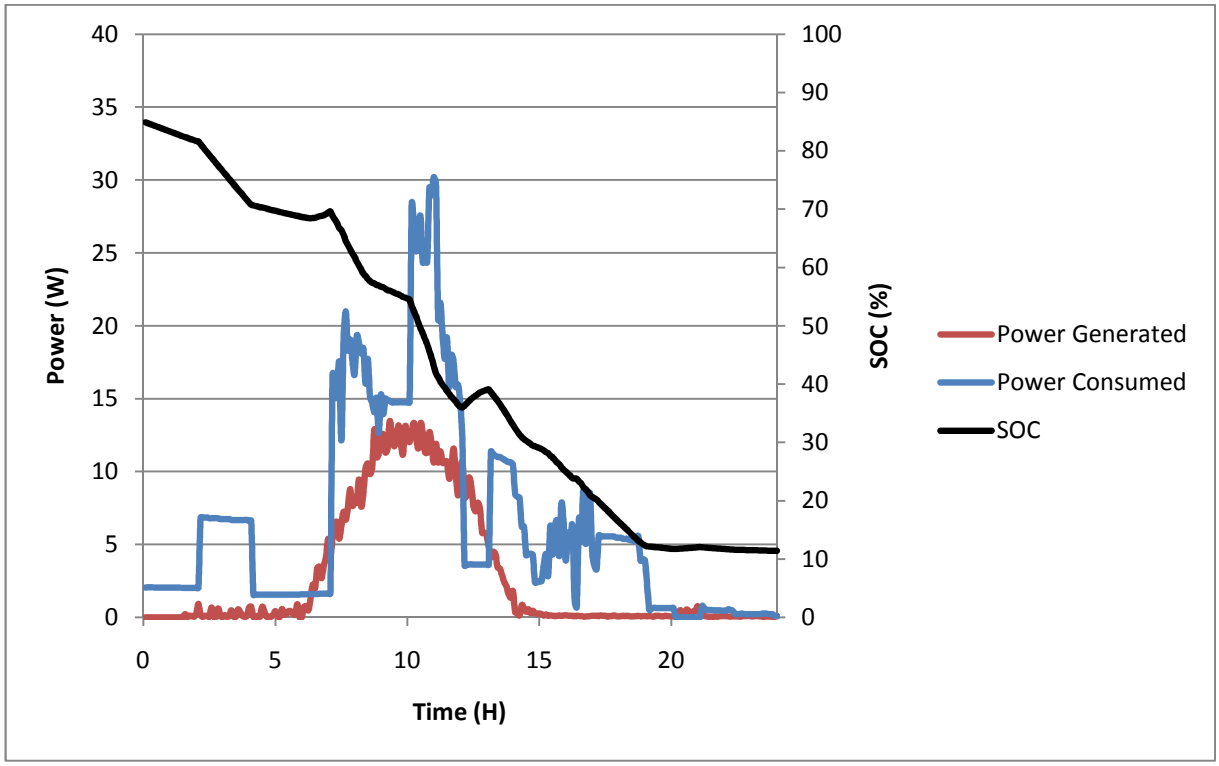

Figure 6-5 Winter Full Load (Pure Hardware)

Figure 6-5 shows that the state of charge of the battery drops off to about 10% by the end of the day and it is clear that the same tasks cannot be performed during the winter months compared to the summer months. At this point, the designer and/or mission planner will have a better idea of the rover's capabilities and may decide to create a different task list for the rover during winter months or make sizing changes to the components. A different drive cycle was created with reduced loads to demonstrate how the system behaves this time (Figure 6-6). With the reduced load, the state of charge of the battery at the end of the day is 44%.

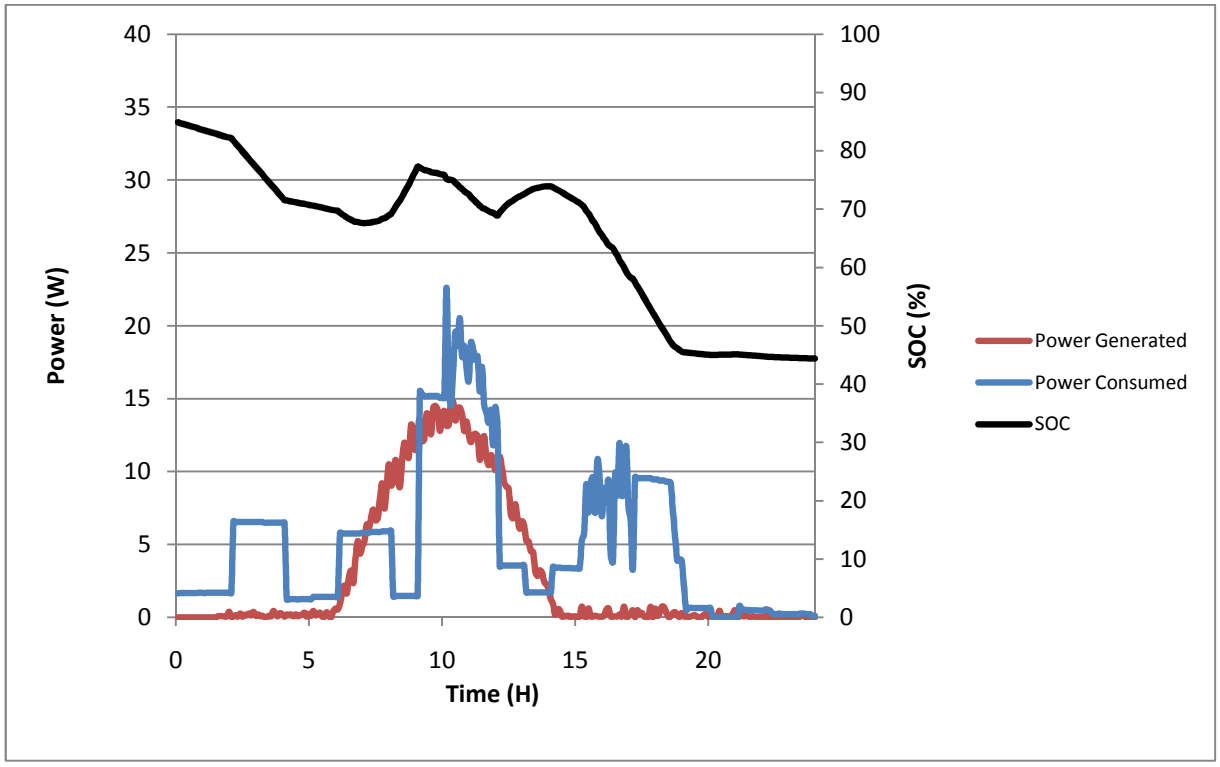

Figure 6-6 Winter Reduced Load (Pure Hardware)

At the time of experimentation, the rover dynamic model could not be executed together with the rover powertrain model because the two models were developed independently and used a different engine within MapleSim 4. The issue was resolved in the recent release of MapleSim 5 at which point it was possible to incorporate the dynamic model within the software library. It was mentioned that as the library of components expands, the accuracy of the simulations can be improved. This can be demonstrated by running a simulation which included the rover dynamic model. Incorporation of the rover dynamic model shows how the effects of the extra rolling resistance generated at the tire-soil interface as well as the elevation changes can affect the rover's overall power consumption. The results of this simulation are shown in Figure 6-7. The inclusion of the rover dynamic model within the simulation loop does not affect the power generation. However, when the rover is traveling, the power consumption is higher because the dynamic model considers the extra resistance that must be overcome at the tire-soil interface.

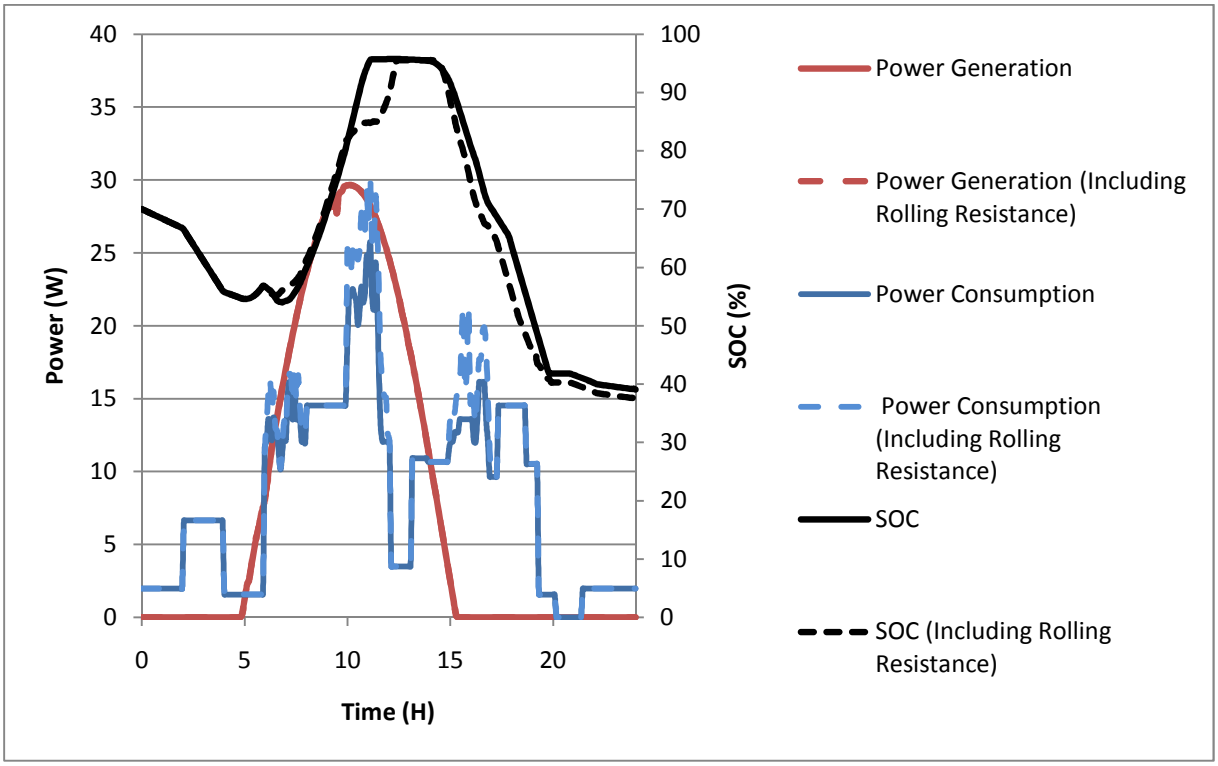

Figure 6-7 Summer Full Load Pure Software including Rover Dynamic Model

Chapter 7
Conclusions and Recommendations

A Hardware-in-the-Loop test platform for planetary rovers was designed, fabricated and tested. There are many applications for the test platform including power estimation, component testing and validation of the power management optimization algorithm as well as the path planning optimization algorithm. This test platform can be used for various types of rovers in different environments however for demonstrating the operation of the test platform, the power system operation of a solar powered rover on Mars was tested. A library of simple mathematical models of main powertrain components of a rover were created in MapleSim including the solar array, battery and motor. As well, a model was created to estimate the solar radiation as experienced by a tilted surface throughout a day. This takes into account the location of the rover on the planet, the day of the year as well as the vehicle's tilt and orientation.

On the hardware side, a test bench which consists of a lighting system, solar array, battery, motor, flywheel and load simulator was designed. The intensity of the light can be controlled to track the light level estimated for a Martian day. Sensors and data acquisition were set up to assess component performance throughout a drive cycle. To enable communication between hardware and software, the MapleSim models were imported within LabView where a complete rover powertrain model was created. Real time simulations were achieved using Labview Real-time in conjunction with National Instrument's PXI. Pure software simulations were run with the rover powertrain model. Subsequent tests were then run with additional hardware components replacing their respective models within the simulation loop.

Full simulations with all the hardware components on the test bed were run at different drive cycles. For each test, a different environment and load cycle was used to demonstrate the ability of the test platform to predict the power availability of the rover throughout a drive cycle. This was done by measuring input and outputs of each component to determine the level of power generation, power consumption by traction motor and auxiliary loads as well as the battery's state of charge. These tests showed the effectiveness of a HIL test platform in estimating the rover's power level.

Compared to pure software simulations, these tests have the advantage that the output actually indicates hardware performance as opposed to estimated performance and therefore provides a more accurate overall estimate of the system performance. These tests also show that one of the major benefits of the HIL test bench is the ability to evaluate the rover's performance without having a rover prototype

or even all the hardware components available. As well, these hardware components would be real hardware that will eventually be in a rover prototype and thus bridges the gap between design and implementation. Not only does the modularity of this test bench allow designers to quickly compare performance of different designs of a component or configurations, but it also allows the methodologies outlined in this paper to be extended to other types of vehicles.

Future work for implementing the test platform includes: 1) Implementing temperature control to the test bench since performance of powertrain components are affected by temperature changes; 2) Using six independently controlled motor to estimate actual power utilization of the wheel motors; 3) Expanding the component library such that different rovers can be modeled/ tested and also different aspects of the rover can be simulated. For example, various tire models can be added to the library to compare its effects on the rover's overall power consumption in different terrains. As well, effects of atmospheric dust accumulation, wind and storms all play an important role in the actual irradiation experienced by the solar panels. Adding these models in the library will also contribute to improved accuracy in simulating the environment. 4) Implementing a more sophisticated lighting system using xenon solar simulators with filters to shape the spectral output such that the solar spectrum as experienced on Mars can be more closely simulated; These amendments will allow for a realistic test platform with which accurate power level estimation can be performed.

Bibliography

[1] NASA-JPL. (2009, Jan) Mars Exploration Rover Mission -Summary. [Online]. http://marsrovers.jpl.nasa.gov/overview/

[2] NASA-JPL. (2009, Jan) Mars Exploration Rover Mission - Surface Operations. [Online]. http://marsrovers.jpl.nasa.gov/mission/spacecraft_surface_rover.html

[3] NASA-JPL. (2000, Sept) Power Management in Past and Present. Document.

[4] NASA. (2004, Feb) NASA Science News. [Online]. http://science.nasa.gov/science-news/science-at-nasa/2004/17feb_radiation/

[5] NASA. (2011, March) Solar System Exploration - Mars Facts and Figures. [Online]. http://solarsystem.jpl.nasa.gov/planets/profile.cfm?Object=Mars&Display=Facts

[6] NASA Goddard Institute for Space Studies. (2008, Aug) Technical Notes on Mars Solar Time as Adopted by the Mars24 Sunclock. [Online]. http://www.giss.nasa.gov/tools/mars24/help/notes.html

[7] NASA. (2010, Nov) Mars Fact Sheet. [Online]. http://nssdc.gsfc.nasa.gov/planetary/factsheet/marsfact.html

[8] B.V.Ratnakumar, R.C.Fwell, L.D.Whitcanack,K.B.Chin, S.Surampudi, F.Puglia, R. Gitzendanner M.C.Smart, "Testing of the Li-ion Batteries in Support of JPL's 2003 Mars Exploration Rover Mission," in *4th International Energy Conversion Engineering Conference and Exhibit*, June 2006, p. 16.

[9] Pete Theisinger. (2004, July) The Mars Exploration Rover Project - How Spirit and Opportunity Got to Mars. Video.

[10] A. Isaacs, H. Arya A. Gholkar, "Hardware-In-Loop Simulator for Mini Aerial Vehicle," *Industrial Electronics, IEEE Transactions on*, vol. 57, no. 4, pp. 1167-1174, April 2010.

[11] C.Pohl, M.Porrmann C.Paiz, "Hardware-in-the-Loop Simulations for FPGA-based Digital Control Design," *Industry Applications, IEEE transactions on*, vol. 47, no. 2, pp. 853-860, March 2011.

[12] C.Y.Tseng, T.W.Tseng C.F.Lin, "A hardware-in-the-loop dynamics simulator for motorcycle rapid," *Control Engineering Practice* , vol. 14, no. 12, pp. 1467-1476, Dec 2006.

[13] R.B.Prasad,E.Choi,D.Min V.K.Chandhrasekran, "Hardware-in-the-Loop Simulation of UAV Non-Linear Control System of Mini-Helicopter," in *International Conference on Hybrid Information*

Technology , New York, 2009.

[14] P.,Bigras, P., Beaudry, J., Lemieux, S., Blain, M. Hamelin, "Hardware-in-the-loop simulation of an impedance controlled robot using a direct-drive test bench," in *International Symposium on Industrial Electronics*, Cambridge, July 2008, pp. 1281 - 1286.

[15] Orang Vahid-Araghi, Amir Khajepour Saber Fallah, "A novel Feature-based Multidisciplinary Path Optimization for Planetary Rovers," *IEEE Transaction on Robotics*, (under review) 2011.

[16] Apogee Instruments. (2010, Feb) Apogee Instruments. [Online]. http://www.apogeeinstruments.com/manuals/SP-110manual.pdf

[17] D.J.Flood J. Appelbaum, "Solar Radiation on Mars," *Solar Energy*, vol. 45, no. 6, pp. 353-363, 1990.

[18] R.M.Harberle, J.Schaeffer,H.Lee J.B.Pollack, "Simulation of the general circulation of Martian atmosphere I: Polar Processes," *Journal of Geophysical Research*, vol. 95, no. B2, pp. 1447-1473, 1990.

[19] Green Rhino Energy. (2010, Feb) Radiation on Tilted Surface. [Online]. http://www.greenrhinoenergy.com/solar/radiation/tiltedsurface.php

[20] J.K.Nayak S.P. Sukhatme, *Solar Energy: Principles of Thermal Collection and Storage*, 3rd ed. New Delhi: Tata Mcgraw-Hill, 2008.

[21] J. R. Gazoli, E. R. Filho [5] M. G. Villalva, "Comprehensive Approach to Modeling and Simulation of Photovoltaic Arrays," *IEEE Transactions on Power Electronics*, vol. 24, no. 5, 2009.

[22] W.A.SHURCLIF, "TRANSMITTANCE AND REFLECTION LOSS OF MULTI-PLATE PLANAR WINDOW OF A SOLAR-RADIATION COLLECTOR: FORMULAS AND TABULATIONS OF RESULTS FOR THE CASE n=1.5," *Solar Energy*, vol. 16, pp. 149-154, June 1974.

[23] R. Santbergen, "Optical Absorption Factor of Solar Cells," Eindhoven University of Technology, Ph.D. Thesis 2008.

[24] J.Nelson, *The Physics of Solar Cells*. London: Imperial College Press, 2003.

[25] National Instruments. (2009, Oct) Photovoltaic Cell I-V Characterization Theory. [Online]. http://zone.ni.com/devzone/cda/tut/p/id/7230

[26] Robyn A.Jackey, "A Simple, Effective Lead-Acid Battery Modeling Process for Electrical System Component Selection," in *Photovoltaic Specialists Conference, 2008. PVSC '08. 33rd IEEE*, San

Diego, 2009, pp. 1-6.

[27] Sorensen. (2010) Sorensen:SL Electronic Load Series: Downloads. [Online]. http://www.sorensen.com/products/SL/SL_Downloads.htm

[28] F. M. White, *Fluid Mechanics*, 6th ed. New York, NY: The McGraw-Hill, 2008.

[29] S.N.Brennan M.D.Petersheim, "Scaling of hybrid-electric vehicle powertrain components," in *IEEE International Conference on Control Applications*, San Antonio, Sept 2008, pp. 720-726.

[30] DWL Wang, GR. Heppler M. Ghanekar, "Scaling laws for linear controllers of flexible link manipulators characterized by nondimensional groups.," *IEEE Trans Rob Automat*, vol. 13, no. 1, pp. 117-127, 1997.

[31] A Alleyne M Polley, "Dimensionless analysis of tire characteristics for vehicle dynamics studies," in *American Control Converence*, Boston, 2004, pp. 3411-3416.

[32] DS Berstein, R Venugopal HJ Palanthandalam-Madapusi, "Dimensional analysis of matrices: state-space models and dimensionless units," *IEEE Contr Syst Mag*, vol. 27, no. 6, pp. 100-109, 2007.

[33] N.C.Johnson J.E.Tillman. (1998, Sept) Mars Meteorology Data, Viking Lander. [Online]. http://www-k12.atmos.washington.edu/k12/resources/mars_data-information/data.html

[34] R.H. Bube A.L.Fahrenbruch, *Fundamentals of Solar Cells*. San Francisco, CA: Academic, 1983.

[35] Optics.org. (2010, Oct) Spire pushes solar cell record to 42.3%. [Online]. http://optics.org/news/1/5/5

[36] Newport Corporation. (2010, Feb) Low Cost Solar Simulators 150W. [Online]. http://search.newport.com/i/1/x1/pageType/q1/Products/q2/Light%20Sources/q3/Solar%20Simulators/q4/Low%20Cost%20Solar%20Simulators,%20150%20W/x2/section/x3/chapter/x4/family/nav/1/#

[37] Newport Corporation. (2010, Feb) Simulation of Solar Radiation. [Online]. http://www.newport.com/Simulation-of-Solar-Irradiation/411986/1033/content.aspx

[38] H.J.Moller, *Semiconductors for Solar Cells*. Norwood, MA: Artech House, 1993.

[39] N.V.Yastrebova. (2007, April) SUNLAB. [Online]. http://sunlab.site.uottawa.ca/pdf/whitepapers/HiEfficMjSc-CurrStatus&FuturePotential.pdf

Appendix A

Hardware Data Sheets

Solar Panels Technical Specifications

ELECTRICAL CHARACTERISTICS	
Maximum Power (Pmax)*	80 W
Tolerance of Pmax	+10%/-5%
Type of Cell	Polycrystalline silicon
Cell Configuration	36 in series
Open Circuit Voltage (Voc)	21.6 V
Maximum Power Voltage (Vpm)	17.3 V
Short Circuit Current (Isc)	5.15 A
Maximum Power Current (Ipm)	4.63 A
Module Efficiency (%)	12.41%
Maximum System (DC) Voltage	600 V
Series Fuse Rating	10 A
NOCT	47.5°C
Temperature Coefficient (Pmax)	-0.485%/°C
Temperature Coefficient (Voc)	-0.36%/°C
Temperature Coefficient (Isc)	0.053%/°C

*Measured at (STC) Standard Test Conditions: 25°C, 1 kW/m² insolation, AM 1.5

MECHANICAL CHARACTERISTICS	
Dimensions (A x B x C below)	21.1" x 47.2" x 1.8"/537 x 1200 x 46 mm
Type of Output Terminal	Junction Box
Weight	20.9 lbs / 9.5 kg
Max Load	50 psf (2400 Pascals)

QUALIFICATIONS	
UL Listed	UL 1703
Fire Rating	Class C
FM	NI CL1 DIV2 GPS A, B, C, D

WARRANTY

25-year limited warranty on power output
Contact Sharp for complete warranty information

Design and specifications are subject to change without notice.
Sharp is a registered trademark of Sharp Corporation. All other trademarks are property of their respective owners. Contact Sharp to obtain the latest product manuals before using any Sharp device. Cover photo: Solar installation by Hudson Valley Clean Energy, Rhinebeck, NY.

IV CURVES

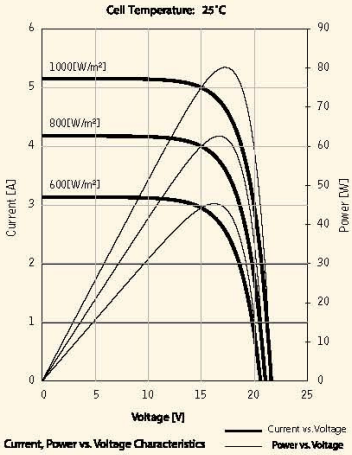

DIMENSIONS

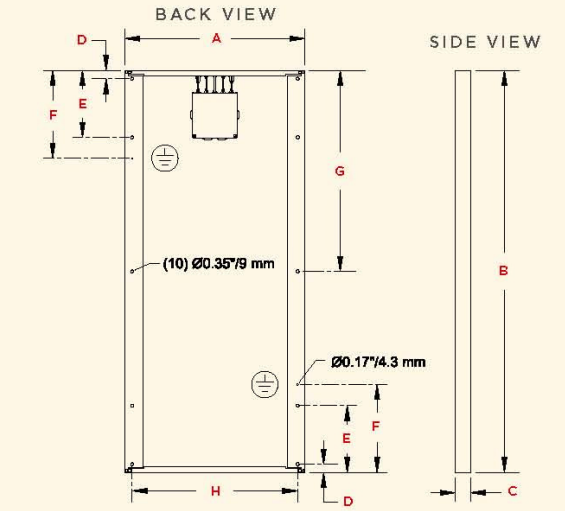

A	B	C	D	E
21.1"/537 mm	47.2"/1200 mm	1.8"/46 mm	0.98"/25 mm	7.9"/200 mm

F	G	H
10.3"/263 mm	23.6"/600 mm	19.4"/494 mm

Contact Sharp for tolerance specifications

12V 30A Solar Charge Controller Technical Specifications

Technical Specifications	
Parameters	**Data**
Electrical	
Normal Input (Solar Cell Array voltage)	17-22 volts
Maximum Input	25 volts
Maximum charging current	30 amps
Current Consumption when connected to 15 volt array (battery not present)	maximum 35mA
Current consumption when connected to a 12 volt battery (array not present)	Maximum 25mA
PWM constant voltage for Gel Cell battery	14.1 volts +/-0.4
PWM constant voltage for Lead Acid battery	14.5 +/-0.4
Float mode voltage	13.4 +/-0.4
Battery Condition Display:	
LED light indicated range	
LOW (red)	<11.5 +/-0.4
FAIR (yellow)	11.5 to 12.5 +/-0.4
GOOD (green)	>12.5+/-0.4
LCD Meter Accuracy DC voltage	1.25%
LCD Meter Accuracy DC current	3%
Protection:	
Over temperature protection engages at (stop charging)	>80°C (176°F)
Over temperature protection resets at (restart charging)	<65°C (149°F)
Operation Temperature	from -5° to 50°C (23° to 122°F)
Storage Temperature	from -10° to 70° C (14° to 158°F)
Operation Humidity Range	0 to 80% RH

Lead Acid Battery Technical Specifications

MotoMaster Battery	Value	
Rated Capacity	10Ah	
Nominal Voltage	12V	
Operating Temperature Range	charge	10 - 45C
	discharge	-20 - 55C
Storage Temperature Range	1 year	-20 - 25C
	3 month	25 - 40C
	1 week	40 - 60C

DC Shunt Motor Technical Specifications

24 Volt Shunt Wound Drive Motor (ES-71A-52)		
Armature Resistance	0.009	ohms at 25C
Field Resistance	0.98	ohms at 25C
Max Armature Current	300	amps
Max Field Current	25	amps
Continuous Armature Current	50	amps
Continuous Field Current	8	amps

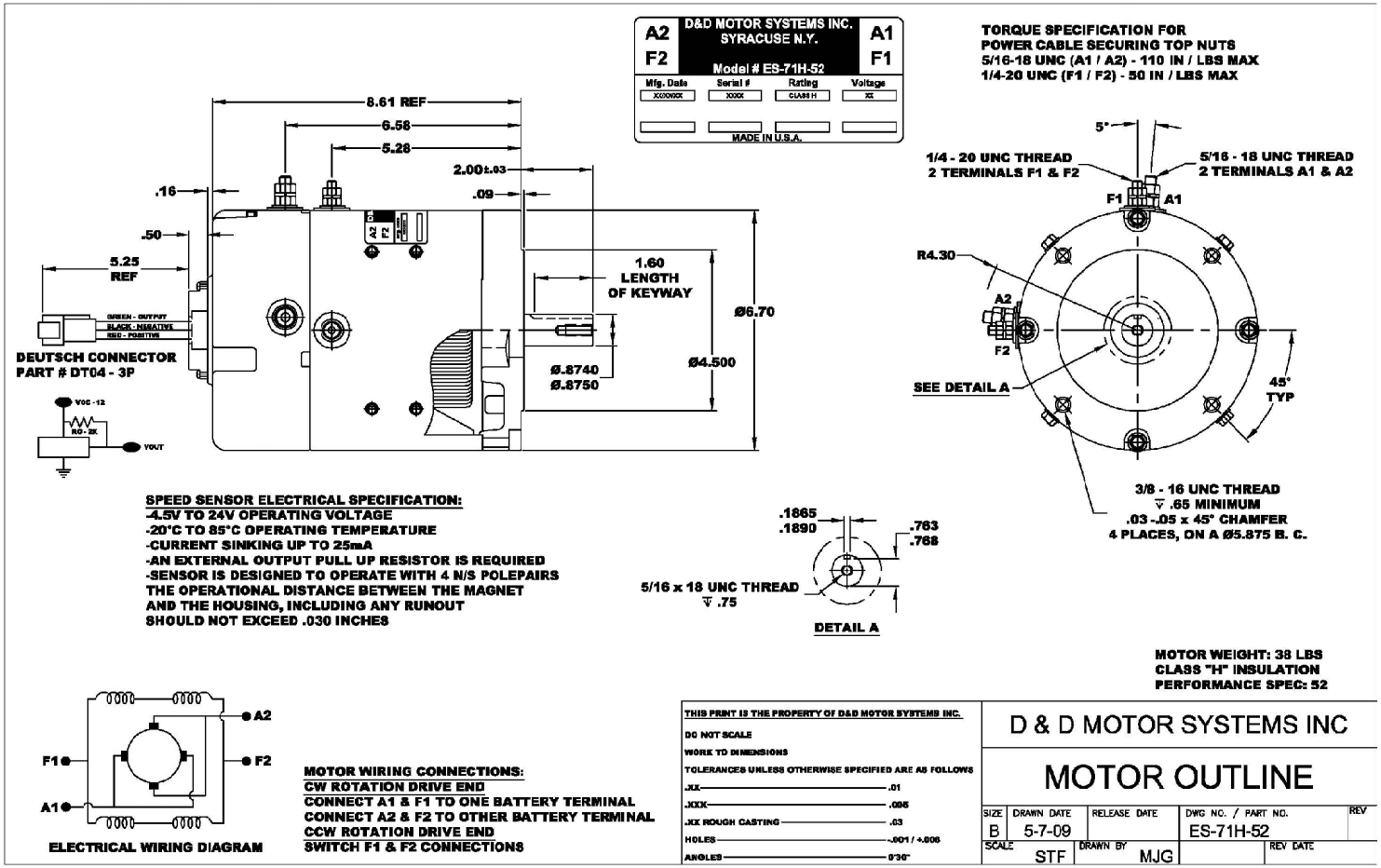
A2
F2
D&D MOTOR SYSTEMS INC.
SYRACUSE N.Y.
A1
F1
Model # ES-71H-52
Mfg. Date
Serial #
Rating
Voltage
XX/XX/XX
XXXX
CLASS H
XX
MADE IN U.S.A.
TORQUE SPECIFICATION FOR
POWER CABLE SECURING TOP NUTS
5/16-18 UNC (A1 / A2) - 110 IN / LBS MAX
1/4-20 UNC (F1 / F2) - 50 IN / LBS MAX
8.61 REF
6.58
5.28
2.00±.03
.16
.09
.50
5.25
REF
1.60
LENGTH
OF KEYWAY
Ø6.70
Ø4.500
Ø.8740
Ø.8750
GREEN - OUTPUT
BLACK - NEGATIVE
RED - POSITIVE
DEUTSCH CONNECTOR
PART # DT04 - 3P
VCC - 12
RO - 2K
VOUT
5°
1/4 - 20 UNC THREAD
2 TERMINALS F1 & F2
5/16 - 18 UNC THREAD
2 TERMINALS A1 & A2
F1
A1
R4.30
A2
F2
SEE DETAIL A
45°
TYP
3/8 - 16 UNC THREAD
↧ .65 MINIMUM
.03 -.05 x 45° CHAMFER
4 PLACES, ON A Ø5.875 B. C.
SPEED SENSOR ELECTRICAL SPECIFICATION:
-4.5V TO 24V OPERATING VOLTAGE
-20°C TO 85°C OPERATING TEMPERATURE
-CURRENT SINKING UP TO 25mA
-AN EXTERNAL OUTPUT PULL UP RESISTOR IS REQUIRED
-SENSOR IS DESIGNED TO OPERATE WITH 4 N/S POLEPAIRS
THE OPERATIONAL DISTANCE BETWEEN THE MAGNET
AND THE HOUSING, INCLUDING ANY RUNOUT
SHOULD NOT EXCEED .030 INCHES
.1865
.1890
.763
.768
5/16 x 18 UNC THREAD
↧ .75
DETAIL A
MOTOR WEIGHT: 38 LBS
CLASS "H" INSULATION
PERFORMANCE SPEC: 52
A2
F1
F2
A1
ELECTRICAL WIRING DIAGRAM
MOTOR WIRING CONNECTIONS:
CW ROTATION DRIVE END
CONNECT A1 & F1 TO ONE BATTERY TERMINAL
CONNECT A2 & F2 TO OTHER BATTERY TERMINAL
CCW ROTATION DRIVE END
SWITCH F1 & F2 CONNECTIONS
THIS PRINT IS THE PROPERTY OF D&D MOTOR SYSTEMS INC.
DO NOT SCALE
WORK TO DIMENSIONS
TOLERANCES UNLESS OTHERWISE SPECIFIED ARE AS FOLLOWS
.XX .01
.XXX .005
.XX ROUGH CASTING .03
HOLES -.001 / +.005
ANGLES 0°30"
D & D MOTOR SYSTEMS INC
MOTOR OUTLINE
SIZE
B
DRAWN DATE
5-7-09
RELEASE DATE
DWG NO. / PART NO.
ES-71H-52
REV
SCALE
STF
DRAWN BY
MJG
REV DATE

Motor Controller (TSX500-416NI)

The TSX 500-48 comes supplied with a low current control wire harness. The drawing below shows the pin configuration for the Ampseal 23 pin I/O connector:

The pin functions are as shown in the chart below:

Pin Number	Input/Output	Function	Wire Color
1	input	Key	red
2	input	Forward Enable	white/yellow
3	input	Reverse Enable	white/grey
4	input	Digital Input 3	white/black
5	input	SRO/Seat Switch	white/red
6	input	Digital input 2	white/purple
7	input	Battery Negative	black
8	input	Battery Positive (pre-charge)	orange
9	input	Primary Throttle	white
10	***	***	***
11	***	***	***
12	***	***	***
13	input	Speed Sensor	white/brown
14	input	Digital input 1	white/orange
15	input	Auxiliary Throttle	white/green
16	input	Battery Negative (poly fused)	white/blue
17	output	+12 VDC	yellow
18	output	Line Contactor Driver	grey
19	output	Aux 3 Output Driver	brown
20	output	Aux 4 Output Driver	blue
21	output	Aux 1 Output Driver	green
22	output	Aux 2 Output Driver	purple
23	input	Battery Positive	orange

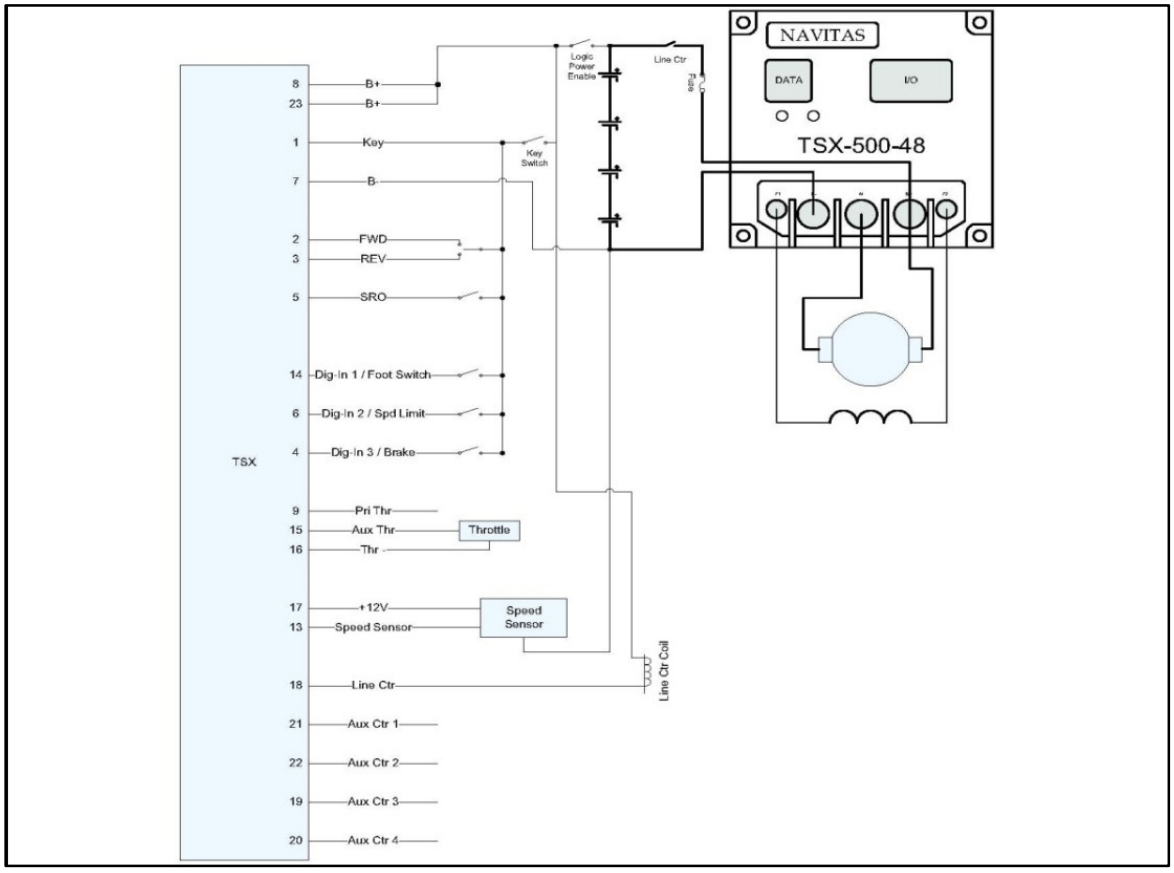
NAVITAS
DATA
I/O
TSX-500-48
Logic Power Enable
Line Ctr
Fuse
Key Switch
TSX
8 B+
23 B+
1 Key
7 B-
2 FWD
3 REV
5 SRO
14 Dig-In 1 / Foot Switch
6 Dig-In 2 / Spd Limit
4 Dig-In 3 / Brake
9 Pri Thr
15 Aux Thr
16 Thr -
Throttle
17 +12V
13 Speed Sensor
Speed Sensor
18 Line Ctr
Line Ctr Coil
21 Aux Ctr 1
22 Aux Ctr 2
19 Aux Ctr 3
20 Aux Ctr 4

NOTE: Before making any high current connections, make sure the battery is disconnected from battery +, battery -, or both. Only reconnect the battery after all connections are complete and double checked.

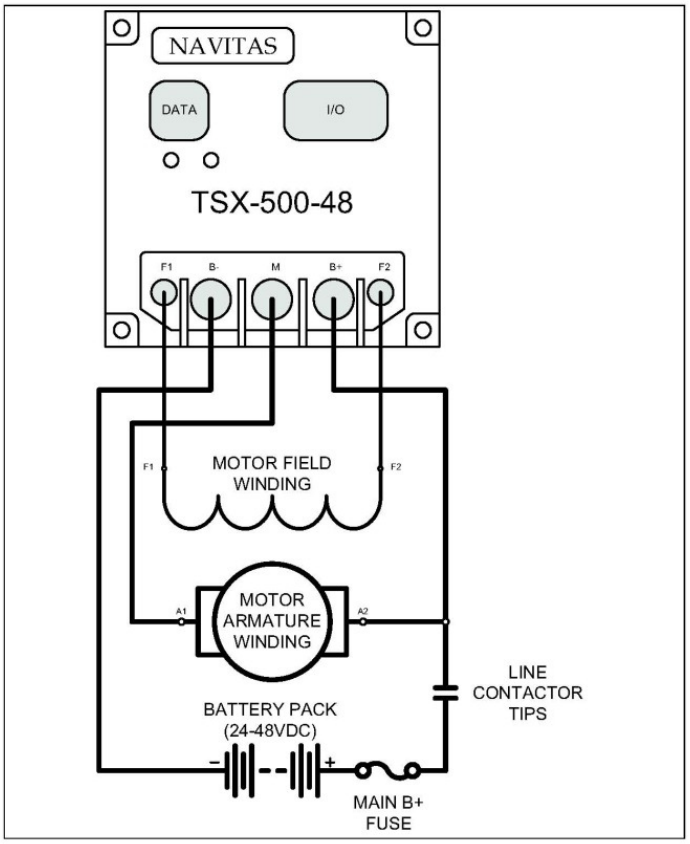

Load Simulator Technical Specifications (SLH 300-18-1800)

NOTE: The following specifications apply 25°±5°:

MODEL	SLH-500-4-1200	SLH-500-6-1800	SLH-300-12-1200/1800	SLH-300-18-1800
INPUT RATINGS				
Power (VA)	1200 VA	1800 VA	1200/1800 VA	1800 VA
Current (Ampere)	4 Arms	6 Arms	12 Arms	18 Arms
Voltage (Volt)	300 Vrms/500 Vdc	300 Vrms/500 Vdc	300Vrms	300Vrms
Frequency	DC, 40 - 70Hz (CC Mode) ; DC - 70Hz (CR Mode)			
CC MODE				
Range	0-2 / 2-4 A	0-3 / 3-6 A	0-6 / 6-12 A	0-9 / 9-18 A
Resolution	0.5 / 1 mA	0.75 / 1.5 mA	1.5 / 3 mA	2.25 / 4.5 mA
Accuracy	±0.5% of (setting + range)			
Low Current Range	0 - 0.2 A	0 - 0.3 A	0 - 0.6 A	0 - 0.9 A
Accuracy	± 2% of (setting + range)			
Crest Factor	√2 - 3.5 (Maximum current = 2 x Rated Current)			
Maximum Peak Current	8A	12A	24A	18A
CR MODE				
Range 1 (I>0.5% of rating)	50 - 200,000 Ω	33.33 - 133,000 Ω	20 - 80,000 Ω	13.3 - 53,333 Ω
Range 2 (I>50% of rating)	12.5 - 50 Ω	8.33 - 33.33 Ω	5 - 20 Ω	3.33 - 13.33 Ω

4-1/2 DVM					
Range	0-500V	0-500V	300 V	300 V	300 V
Resolution	0.1 V	0.1 V	0.1 V	0.1 V	0.1 V
Accuracy	±(0.5% of reading + 0.2% of range)				
4-1/2 DAM					
Range	0-4 A	0-6 A	0-12 A	0-12 A	0-18 A
Resolution	1 mA	1 mA	1 mA	1 mA	1 mA
Accuracy	±(0.5% of reading + 2% of range) ; ±0.5% of (reading + range) @ 50/60Hz				
4-1/2 WATT METER					
Range	0-1200W	0-1800 W	0-1200W	0-1800 W	0-1800 W
Resolution	0.1 W				
Accuracy	± (0.5% of reading)± 3W				
VA METER	Vrms×Arms				

Table 1-1 SLH-series AC/DC Specifications

NI-PXI 8187 real time controller: www.ni.com

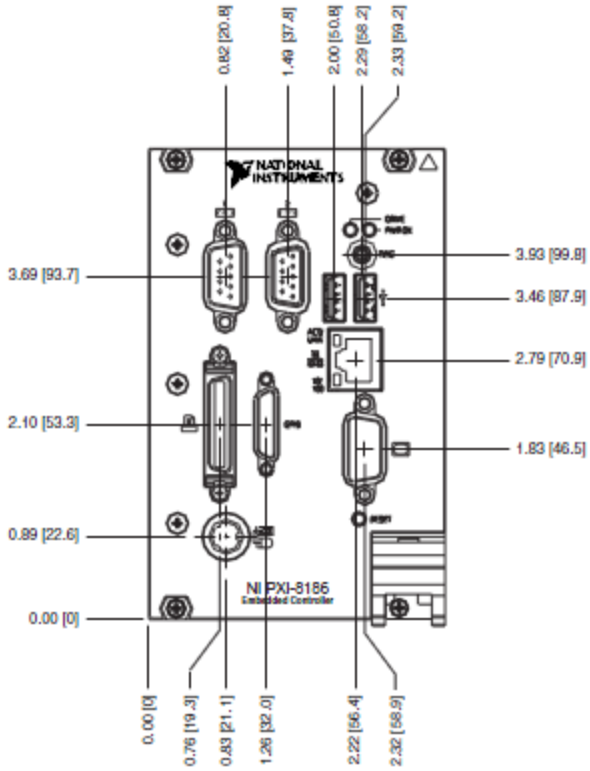

PXI 6229 Low cost M-series DAQ: www.ni.com

Low-Cost M Series Multifunction DAQ – 16-Bit, 250 kS/s, up to 80 Analog Inputs

NI M Series – Low-Cost

- NI recommends high-speed M Series for 5X faster sampling rates or high-accuracy M Series for 4X higher resolution
- 16, 32, or 80 analog inputs at 16-bit, 250 kS/s
- Up to 4 analog outputs at 16 bits, 833 kS/s/ch 6 µs full-scale settling time
- Programmable input range (±1.0, ±5, ±1, ±0.2 V) per channel
- Up to 48 TTL/CMOS digital I/O lines (up to 32 hardware-timed at 1 MHz)
- Two 32-bit, 80 MHz counter/timers
- Digital triggering
- NI-MCal calibration technology for improved measurement accuracy
- 6 DMA channels for fast data throughput
- Available lifetime warranty and calibration services

Operating Systems

- Windows 2000/XP
- Mac OS X
- Linux®

Recommended Software

- LabVIEW
- LabWindows/CVI
- Measurement Studio

Other Compatible Software

- SignalExpress
- VI Logger
- Visual Studio .NET
- C/C++/C#

Measurement Services

Software (included)[1]

- NI-DAQmx driver software
- Measurement & Automation Explorer configuration utility
- VI Logger Lite data-logging software

[1]Mac OS X users must download NI-DAQmx Base driver.

Lifetime Warranties ***NEW!***

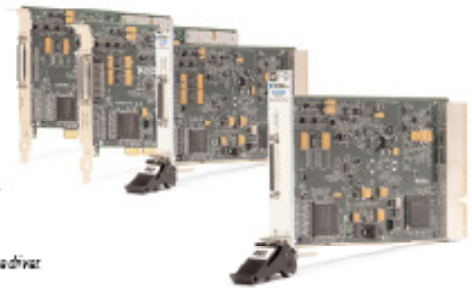

Family	Bus	Analog Inputs	Analog Input Resolution (bits)	Analog Outputs	Output Resolution (bits)	Max Output Rate (kS/s)	Analog Output Range (V)	Digital I/O	Correlated (clocked) DIO
NI 6220	PCI, PXI	16	16	–	–	–	–	24	8, up to 1 MHz
NI 6221	PCI, PXI	16	16	2	16	833	±10	24	8, up to 1 MHz
NI 6221 (37-Pin)[1]	PCI	16	16	2	16	833	±10	24	8, up to 1 MHz
NI 6224	PCI, PXI	32	16	–	–	–	–	48	32, up to 1 MHz
NI 6225	PCI, PXI	80	16	2	16	833	±10	24	8, up to 1 MHz
NI 6229	PCI, PXI	32	16	4	16	833	±10	48	32, up to 1 MHz

[1] 37-Pin multifunction DAQ devices are not compatible with NI SCC or SCXI platforms.

Table 1. Low-Cost M Series Selection Guide

PXI 6259 High speed M-series DAQ

High-Speed M Series Multifunction DAQ – 16-Bit, up to 1.25 MS/s, up to 32 Analog Inputs

NI M Series – High-Speed

- NI recommends high-accuracy M Series for 5X more measurement sensitivity and lowpass filtering
- 16 or 32 analog inputs at 16 bits, 1.25 MS/s (1 MS/s scanning)
- Up to 4 analog outputs at 16 bits, 2.8 MS/s (2 µs full-scale settling)
- 7 programmable input ranges (±100 mV to ±10 V) per channel
- Up to 48 TTL/CMOS digital I/O lines (up to 32 hardware-timed at 10 MHz)
- Two 32-bit, 80 MHz counter/timers
- Analog and digital triggering
- NI-MCal calibration technology for improved measurement accuracy
- 6 DMA channels for high-speed data throughput
- 4 USB signal streams for high-speed data transfer
- Available lifetime warranty and calibration services

Operating Systems

- Windows 2000/XP
- Mac OS X
- Linux®

Recommended Software

- LabVIEW
- LabWindows/CVI
- Measurement Studio

Other Compatible Software

- SignalExpress
- VI Logger
- Visual Studio .NET
- C/C++/C#

Measurement Services Software (included)[2]

- NI-DAQmx driver software
- Measurement & Automation Explorer configuration utility
- VI Logger Lite data-logging software

[1] USB devices supported only in Windows 2000/XP.

[2] Mac OS X users must download NI-DAQmx Base driver.

Lifetime Warranties *NEW!*

Family	Bus	Analog Inputs	Analog Input Resolution (bits)	Analog Outputs	Analog Output Resolution (bits)	Max Output Rate (MS/s)	Analog Output Range (V)	Digital I/O	Correlated (clocked) DIO
NI 6250	PCI, PXI	16	16	0	–	–	–	24	8, up to 10 MHz
NI 6251[1]	USB, PCI Express, PCI, PXI	16	16	2	16	2.8	±10, ±5, exact mA	24	8, up to 10 MHz[2]
NI 6254	PCI, PXI	32	16	0	–	–	–	48	32, up to 10 MHz
NI 6259[1]	USB, PCI Express, PCI, PXI	32	16	4	16	2.8	±10, ±5, exact mA	48	32, up to 10 MHz[2]

[1] USB devices are not compatible with SCC or SCB signal conditioning.
[2] USB devices can clock DIO up to 1 MHz across the bus and up to 10 MHz using onboard regeneration.

Table 1. High Speed M Series Selection Guide

DCDC Converter

	DCDC12/24/300	Units	
Operating Temperature Range:	-40 to +60	degrees Centigrade	
Efficiency:	93	%	
Recommended Input Voltage:	10-20	Volts	
Standby Current - No Load at 12V in	130	mA	
Input Current is internally limited to:	29	Amps	
Input Fuse:	external(50)	Amps	
Output Voltage:	20 to 30	Volts (Adjustable)	
Output Power:	300 (note 1)	Watts	.
Output Current:	12.5 (note 2)	Amps	
Output Fuse:	15	Amps	
Output Ripple, max:	0.25	Volts, RMS	
Switching Frequency:	54,000	Hertz	
Model Number:	DCDC12/24/300	.	.
Wiring Dia.:	CLICK HERE	.	.
Mech. Install:	CLICK HERE	.	.
To Order, Call 262 835 9200. Price:	$169, small qtys		(note 3)

(note 1). The output power, depends on the input voltage. 247W at 10Vin, 370W at 20V in.
(note 2). The output current, depends on the input voltage, and the output voltage.
Determine the output power from (note 1), then calculate output current.
(note 3). Prices can change without notice.

Pyranometer

SPECIFICATIONS

COSINE RESPONSE
- 45° zenith angle: ± 1%
- 75° zenith angle: ± 5%

ABSOLUTE ACCURACY
- ± 5%

REPEATABILITY
- ± 1%

LONG-TERM DRIFT
- Less than 3% per year

OPERATING ENVIRONMENT
- -40 to 55° C
- 0 to 100% relative humidity
- Designed for continuous outdoor use
- Can be submerged in water

CURRENT DRAW
- 285 µA

2.5 V OPTION
- Output: 0 to 2.5 V (2.2 V = full sunlight 1100 W m^{-2})
- Input Power: 2.5 to 5.5 VDC
- Sensitivity: Custom calibrated to exactly 0.5 W m^{-2} per mV

5.0 V OPTION
- Output: 0 to 5 V (4.4 V = full sunlight 1100 W m^{-2})
- Input Power: 5 to 5.5 VDC
- Sensitivity: Custom calibrated to exactly 0.25 W m^{-2} per mV

MATERIALS
- Anodized aluminum with cast acrylic lens

MASS
- 70 g (with 5 m lead wire)

CABLE
- 5 meters of twisted-pair wire
- Shielded w/ Santoprene casing
- Ending in pigtail leads
- Additional cable is available in multiples of 5 meters

WARRANTY
- 1 year against defects in materials and workmanship

Thermocouple (CO3-K)

Model No.	Price	Style	Thermocouple Type	Length	Maximum Temperature °C (°F)*		
					Continuous	600 hr	10 hr
CO1-K	$62	1	K CHROMEGA®-ALOMEGA®	1 m (40")	260 (500)	315 (600)	370 (700)
CO1-E	62		E CHROMEGA®-Constantan	1 m (40")	260 (500)	315 (600)	370 (700)
CO1-T	62		T Copper - Constantan	1 m (40")	150 (300)	205 (400)	260 (500)
CO2-K	$62	2	K CHROMEGA®-ALOMEGA®	150 mm (6")	540 (1000)	540 (1000)	650 (120)
CO2-E	62		E CHROMEGA®-Constantan	150 mm (6")	425 (800)	425 (800)	540 (1000)
CO2-T	62		T Copper-Constantan	150 mm (6")	150 (300)	150 (300)	260 (500)
CO3-J	$42	3	J Iron - Constantan	1 m (40")	260 (500)	370 (700)	370 (700)
CO3-K	42		K CHROMEGA®-ALOMEGA®	1 m (40")	260 (500)	370 (700)	370 (700)
CO3-E	42		E CHROMEGA®-Constantan	1 m (40")	260 (500)	370 (700)	370 (700)
CO3-T	42		T Copper-Constantan	1 m (40")	205 (400)	260 (500)	370 (700)

Current Sensor

Device Specifications

Characteristic	Value
Active Current Consumption	10mA
Output Impedance	1K ohms
Minimum Measurable AC Current	75mA
Minimum Measurable DC Current	±75mA
Maximum Measurable AC Current	30A
Maximum Measurable DC Current	±30A
Maximum Measurable AC Frequency	10kHz
Current Conductor Resistance	1.5mΩ
Maximum Supply Voltage	5.5VDC
Minimum Supply Voltage	4.5VDC
Terminal Block Recommended Wire Size	10 - 26 AWG
Wire Stripping Length	6-7mm
Total Output Error [1]	±5% Max between -40°C to +85°C
Total Output Error (Typical)	±1.5% @ 25°C

Voltage Sensor

Device Specifications

Characteristic	Value
Current Consumption	3.6mA
Input Impedance	1MegaOhm
Recommended Max Difference between Vin+ and Vin-	30V
Absolute Maximum Difference between Vin+ and Vin-	35V
Input CMR	40V
Ouput Range	0 to 5V
Min/Max Error	±2.0%
Typical Error	±0.7%
Maximum Offset at 0V input	±100mV

Encoder

Single-ended Electrical

- Specifications apply over entire operating temperature range.
- Typical values are specified at Vcc = 5.0Vdc and 25 ° C.
- For complete details see the EM1 and HEDS product pages.

	Supply Current	Output voltage low	Output voltage high	
Resolution	Typ / Max	Max	Min	Based on
1000, 1024 CPR, non-index	17 / 40 mA	0.4 volts @ 3.2mA	2.4 volts @ -200uA	Low-res HEDS
2000, 2048 CPR, non-index	57 / 85 mA	0.5 volts @ 8mA	2.4 volts @ -40uA	High-res HEDS
64 CPR, with index	27 / 30 mA	0.5 volts @ 8mA	2.0 volts @ -8mA	EM1
1000, 1024 CPR, with index	57 / 85 mA	0.5 volts @ 8mA	2.4 volts @ -40uA	High-res HEDS
2000, 2048 CPR, with index	57 / 85 mA	0.5 volts @ 8mA	2.4 volts @ -40uA	High-res HEDS
2500 CPR, with index	55 / 57 mA	0.5 volts @ 8mA	2.0 volts @ -8mA	EM1

Differential Electrical

Specification	Min.	Typ.	Max.	Units	Notes
Supply	4.5	5.0	5.5	Volts	
Current Consumption					
Index: 64 CPR	-	28	53	mA	No load
Index: 1800, 2500 CPR	-	56	59	mA	No load
Index: All Other Resolutions	-	58	88	mA	No load
Non-index: <2000 CPR	-	18	43	mA	No load
Non-index: >=2000	-	58	88	mA	No load
Non-index: 2500	-	56	59	mA	No load
Output Voltage					
Sourcing to +5	2.4	3.4	-	Volts	@ -20mA
Sinking to Ground	-	0.2	0.4	Volts	@ 20mA

For complete details see the EM1 / HEDS page.

Pin-outs

5-pin Single-ended:

Pin	Description	
1	Ground	BL
2	Index	G
3	A channel	W
4	+5VDC power	R
5	B channel	BR

PWM Solid State Relay (18A)

OUTPUT SPECIFICATIONS (1)

Description	5 A	12 A	18 A	12 A	18 A
Operating Voltage (47-63Hz) [Vrms]	24-280	24-280	24-280	48-660	48-660
Transient Overvoltage [Vpk]	600	600	600	1200	1200
Maximum Off-State Leakage Current @ Rated Voltage [mArms](5)	0.1	0.1	0.1	0.1	0.1
Minimum Off-State dv/dt @ Maximum Rated Voltage [V/µsec] (2)	500	500	500	500	500
Maximum Load Current (4) [Arms]	5	12	18	12	18
Minimum Load Current [mArms]	150	150	150	150	150
Maximum Surge Current (16.6ms) [Apk]	40	150	200	150	200
Maximum On-State Voltage Drop @ Rated Current [Vpk]	1.5	1.5	1.5	1.5	1.5
Thermal Resistance Junction to Case (Rjc) [°C/W]	2	2	1.1	2	1.1
Maximum I^2t for Fusing (8.3 msec) [A^2 sec]	95	95	170	95	170
Minimum Power Factor (with Maximum Load)	0.5	0.5	0.5	0.5	0.5

GENERAL SPECIFICATIONS

Description	Parameters
Dielectric Strength, Input/Output/Base (50/60Hz)(3)	4000 Vrms *
Minimum Insulation Resistance (@ 500 V DC)	10^9 Ohm
Maximum Capacitance, Input/Output	8 pF
Ambient Operating Temperature Range	-40 to 80 °C
Ambient Storage Temperature Range	-40 to 125 °C
Weight (typical)	1.5 oz (43 g)
Encapsulation	Thermally conductive Epoxy
Terminals	0.25 Inch Faston

GENERAL NOTES

1) All parameters at 25°C unless otherwise specified.
2) Off-State dv/dt test method per EIA/NARM standard RS-443, paragraph 13.11.1
3) 240V, DC control models only, all others 2500VRMS
4) Heat sinking required, for derating curves see page 2.
5) Off- state leakage for snubbered version (suffix S) is 10.0mArms
6) Turn-on time for random turn-on versions is 0.1 msec (DC Control Models).

Lighting Control Circuit Diagram

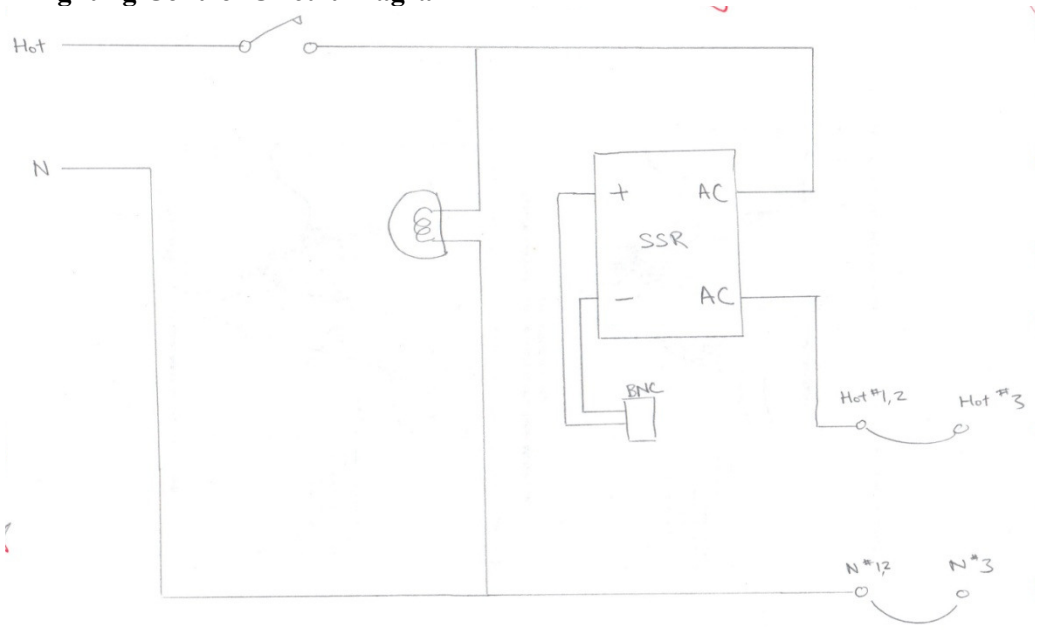

Appendix B

Martian Environment

Mars Surface Albedo [17]

Longi-tude	Latitude, ϕ, deg																				
	-90	-80	-70	-60	-50	-40	-30	-20	-10	0	10	20	30	40	50	60	70	80	90
E 180	0.375	0.245	0.230	0.175	0.200	0.200	0.200	0.225	0.255	0.275	0.275	0.275	0.265	0.255	0.235	0.210	0.230	0.340	0.400
170	.375	.245	.230	.175	.200	.200	.195	.210	.250	.270	.270	.270	.270	.260	.235	.200	.230	.340	.400
160	.375	.245	.230	.175	.205	.200	.190	.195	.240	.265	.270	.270	.270	.265	.235	.200	.230	.340	.400
150	.375	.245	.230	.180	.210	.210	.185	.180	.225	.255	.265	.265	.275	.270	.235	.200	.230	.340	.400
140	.375	.245	.230	.185	.220	.225	.185	.175	.200	.250	.260	.260	.275	.270	.235	.210	.235	.365	.410
130	.375	.245	.230	.185	.225	.230	.190	.175	.190	.235	.250	.255	.265	.265	.230	.200	.250	.425	.425
120	.375	.245	.230	.190	.240	.235	.195	.175	.185	.225	.240	.240	.250	.260	.225	.190	.250	.430	.425
110	.375	.245	.230	.190	.240	.235	.195	.175	.180	.220	.235	.235	.250	.255	.220	.185	.250	.430	.425
100	.375	.245	.230	.195	.230	.225	.190	.175	.175	.210	.230	.235	.255	.250	.205	.180	.250	.430	.425
90	.375	.245	.230	.195	.230	.225	.190	.175	.175	.200	.225	.230	.250	.248	.190	.175	.250	.430	.425
80	.375	.245	.230	.200	.245	.250	.200	.175	.170	.175	.175	.210	.240	.245	.200	.175	.250	.430	.425
70	.375	.245	.230	.200	.250	.265	.225	.175	.160	.150	.150	.185	.230	.248	.210	.185	.250	.430	.425
60	.375	.245	.230	.200	.250	.265	.225	.180	.170	.175	.180	.210	.245	.250	.225	.190	.250	.425	.425
50	.400	.245	.230	.195	.240	.250	.200	.180	.185	.220	.240	.250	.255	.255	.227	.200	.235	.400	.420
40	.450	.250	.230	.190	.225	.225	.190	.180	.200	.250	.265	.270	.260	.250	.230	.210	.230	.365	.410
30	.450	.300	.230	.185	.215	.220	.190	.190	.210	.250	.275	.275	.265	.250	.230	.210	.230	.340	.400
20	.450	.300	.230	.180	.205	.215	.195	.200	.210	.245	.270	.275	.265	.250	.230	.210	.230	.340	.400
10	.450	.300	.230	.175	.200	.210	.195	.205	.200	.220	.250	.265	.252	.250	.225	.210	.230	.340	.400
0	.450	.300	.230	.175	.200	.205	.190	.190	.185	.200	.230	.245	.235	.220	.200	.200	.230	.340	.400
10	.450	.300	.230	.175	.200	.205	.185	.182	.180	.200	.220	.230	.220	.185	.160	.175	.230	.340	.400
20	.450	.300	.230	.180	.200	.200	.180	.175	.175	.200	.220	.210	.185	.150	.135	.160	.230	.340	.400
30	.450	.300	.230	.180	.205	.200	.175	.170	.175	.200	.225	.210	.175	.135	.125	.150	.230	.340	.400
40	.450	.300	.230	.180	.205	.200	.170	.170	.175	.210	.230	.225	.185	.150	.135	.150	.230	.340	.400
50	.400	.250	.230	.180	.205	.200	.175	.170	.175	.215	.240	.225	.210	.200	.175	.170	.230	.340	.400
60	.375	.245	.230	.175	.200	.195	.175	.175	.190	.225	.245	.235	.230	.235	.225	.190	.230	.340	.400
70	.375	.245	.230	.175	.190	.195	.185	.180	.205	.250	.260	.255	.255	.265	.250	.210	.230	.340	.400
80	.375	.245	.230	.175	.185	.195	.185	.180	.215	.270	.285	.277	.277	.275	.255	.225	.235	.340	.400
90	.375	.245	.230	.175	.180	.190	.185	.190	.225	.285	.300	.285	.280	.275	.262	.230	.235	.340	.400
100	.375	.245	.230	.175	.175	.190	.185	.200	.250	.300	.300	.290	.287	.275	.270	.235	.235	.340	.400
110	.375	.245	.230	.175	.175	.190	.185	.200	.260	.295	.295	.288	.285	.275	.275	.240	.235	.340	.400
120	.375	.245	.230	.175	.175	.190	.180	.215	.270	.290	.290	.285	.282	.275	.270	.235	.230	.340	.400
130	.375	.245	.230	.175	.185	.200	.190	.230	.275	.280	.285	.280	.280	.275	.262	.225	.230	.340	.400
140	.375	.245	.230	.175	.195	.200	.200	.240	.275	.280	.280	.280	.277	.275	.255	.220	.230	.340	.400
150	.375	.245	.230	.175	.200	.200	.200	.235	.275	.275	.280	.280	.272	.270	.250	.220	.230	.340	.400
160	.375	.245	.230	.175	.200	.200	.200	.225	.265	.275	.275	.275	.265	.265	.250	.215	.230	.340	.400
170	.375	.245	.230	.175	.200	.200	.200	.225	.260	.275	.275	.275	.265	.260	.240	.210	.230	.340	.400
W 180	.375	.245	.230	.175	.200	.200	.200	.225	.255	.275	.275	.275	.265	.255	.235	.210	.230	.340	.400

Optical Depth as measured by Viking Lander 1[17]

The two peaks were two global dust storms observed during the year.

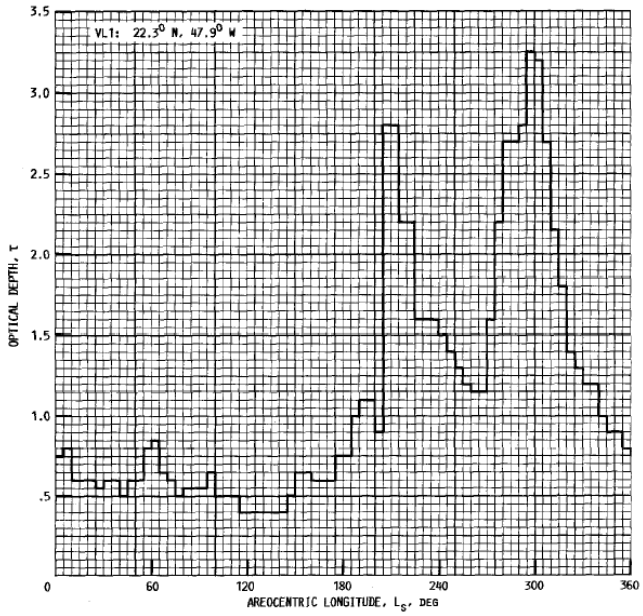

Optical Depth as measured by Viking Lander 2 [17]

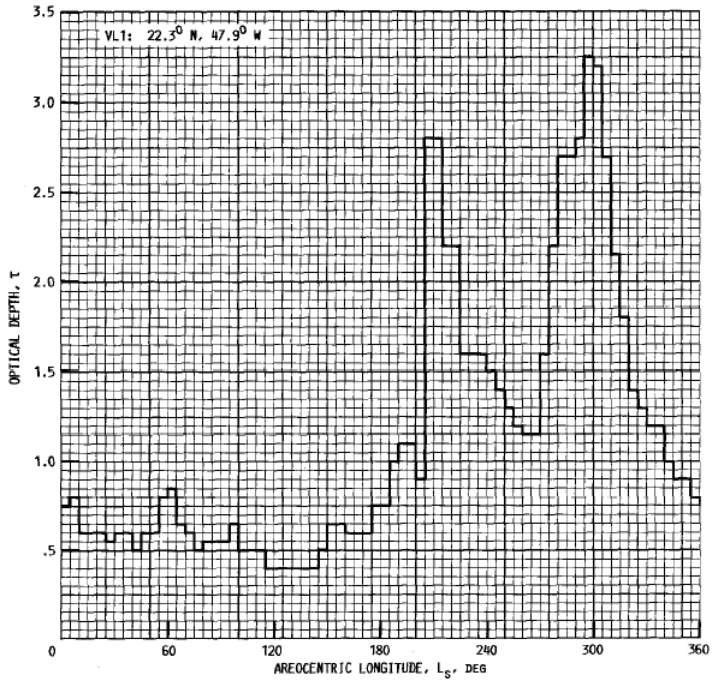

Normalized Net Flux Function f(z,tau,al=0.1) at the Martian surface [18]

Albedo 0.1									
Optical depth, τ	Zenith angle z, deg								
	0	5	10	15	20	25	30	35	40
0.10	0.883	0.883	0.883	0.882	0.881	0.880	0.879	0.877	0.875
.15	.875	.875	.874	.873	.872	.870	.868	.866	.862
.20	.866	.866	.865	.864	.862	.860	.857	.854	.850
.25	.857	.857	.856	.854	.852	.849	.846	.842	.838
.30	.848	.848	.847	.845	.842	.839	.835	.831	.826
.35	.839	.839	.838	.836	.833	.829	.824	.819	.813
.40	.830	.830	.829	.826	.823	.819	.814	.808	.801
.45	.822	.821	.820	.817	.814	.809	.804	.797	.790
.50	.813	.813	.811	.808	.804	.799	.793	.786	.778
.55	.805	.804	.802	.799	.795	.789	.783	.775	.767
.60	.796	.795	.793	.790	.785	.779	.772	.764	.755
.65	.787	.786	.784	.780	.775	.769	.762	.754	.743
.70	.778	.777	.775	.771	.766	.759	.752	.743	.732
.75	.770	.768	.766	.762	.757	.750	.742	.733	.721
.80	.761	.760	.757	.753	.748	.741	.732	.722	.711
.85	.752	.751	.748	.744	.739	.731	.722	.712	.701
.90	.744	.743	.740	.736	.730	.722	.713	.703	.690
.95	.736	.735	.732	.727	.721	.713	.703	.693	.680
1.00	.728	.727	.724	.719	.712	.704	.694	.683	.669
1.05	.720	.719	.716	.711	.704	.695	.685	.673	.659
1.10	.712	.711	.708	.703	.696	.687	.676	.664	.649
1.15	.704	.703	.700	.695	.688	.678	.667	.655	.640
1.20	.695	.694	.691	.686	.679	.669	.658	.645	.630
1.25	.687	.686	.683	.678	.670	.660	.649	.636	.621
1.30	.679	.678	.675	.670	.662	.652	.640	.627	.611
1.35	.672	.671	.668	.662	.654	.644	.632	.619	.602
1.40	.664	.663	.660	.654	.646	.636	.624	.611	.594
1.45	.657	.655	.652	.646	.638	.627	.615	.602	.585
1.50	.649	.648	.644	.638	.630	.619	.607	.593	.576
1.55	.642	.640	.637	.631	.622	.612	.599	.585	.568
1.60	.634	.633	.629	.623	.615	.604	.591	.577	.559
1.65	.627	.625	.621	.615	.607	.596	.583	.568	.551
1.70	.619	.618	.614	.608	.599	.588	.575	.560	.542
1.75	.612	.611	.607	.601	.592	.581	.568	.553	.534
1.80	.605	.604	.600	.594	.585	.574	.561	.546	.527
1.85	.598	.597	.593	.587	.578	.567	.553	.538	.520
1.90	.591	.590	.586	.580	.571	.559	.546	.531	.513
1.95	.584	.583	.579	.573	.564	.552	.539	.524	.506
2.00	.578	.576	.572	.566	.557	.546	.532	.517	.498
2.10	.564	.563	.558	.552	.543	.532	.518	.502	.483
2.20	.551	.549	.545	.539	.530	.518	.504	.489	.469
2.30	.538	.537	.533	.526	.517	.505	.492	.476	.457
2.40	.526	.524	.520	.514	.505	.493	.479	.464	.444
2.50	.514	.512	.508	.502	.493	.481	.467	.451	.432
2.60	.501	.499	.496	.489	.480	.468	.454	.438	.420
2.70	.489	.487	.483	.477	.468	.456	.441	.426	.407
2.80	.478	.477	.473	.466	.456	.445	.431	.415	.395
2.90	.467	.466	.462	.455	.446	.435	.421	.405	.385
3.00	.457	.456	.452	.445	.436	.425	.411	.395	.376
3.20	.436	.435	.431	.425	.416	.405	.391	.375	.357
3.40	.415	.414	.410	.404	.395	.384	.371	.356	.338
3.60	.395	.393	.389	.384	.376	.365	.352	.337	.319
3.80	.378	.376	.372	.367	.359	.349	.336	.321	.304
4.00	.363	.361	.357	.352	.344	.334	.321	.307	.290
4.50	.325	.323	.320	.315	.307	.297	.286	.272	.257
5.00	.289	.288	.285	.280	.273	.264	.253	.241	.227
5.50	.257	.256	.253	.249	.242	.234	.225	.213	.201
6.00	.229	.227	.224	.220	.215	.209	.200	.189	.178

Albedo 0.1									
Optical depth, τ	Zenith angle z, deg								
	45	50	55	60	65	70	75	80	85
0.10	0.872	0.868	0.862	0.855	0.844	0.830	0.804	0.757	0.640
.15	.858	.852	.844	.834	.819	.798	.762	.700	.566
.20	.844	.836	.826	.813	.794	.768	.724	.651	.508
.25	.831	.821	.808	.793	.770	.739	.688	.608	.466
.30	.818	.806	.791	.773	.747	.712	.656	.571	.433
.35	.804	.791	.774	.754	.726	.687	.627	.539	.407
.40	.790	.776	.758	.736	.706	.663	.599	.510	.385
.45	.778	.762	.742	.718	.686	.641	.575	.485	.367
.50	.765	.748	.727	.701	.667	.619	.551	.462	.351
.55	.753	.734	.712	.684	.648	.598	.528	.440	.337
.60	.741	.721	.697	.668	.631	.579	.508	.422	.325
.65	.728	.708	.683	.653	.615	.562	.491	.407	.315
.70	.716	.695	.669	.638	.600	.546	.474	.393	.306
.75	.705	.682	.655	.623	.585	.530	.457	.379	.297
.80	.693	.670	.642	.609	.570	.514	.442	.366	.288
.85	.682	.658	.630	.596	.556	.500	.429	.356	.281
.90	.671	.646	.617	.583	.543	.486	.416	.345	.274
.95	.660	.634	.605	.570	.528	.472	.403	.335	.267
1.00	.649	.623	.593	.557	.514	.459	.392	.324	.261
1.05	.638	.613	.582	.546	.503	.448	.382	.316	.255
1.10	.628	.602	.571	.535	.492	.438	.374	.309	.250
1.15	.618	.592	.561	.524	.480	.427	.364	.302	.245
1.20	.608	.581	.550	.513	.469	.416	.355	.295	.240
1.25	.598	.570	.539	.502	.457	.405	.346	.287	.235
1.30	.588	.560	.528	.491	.446	.395	.337	.280	.230
1.35	.579	.551	.519	.482	.437	.387	.331	.275	.226
1.40	.571	.542	.510	.473	.429	.379	.324	.270	.222
1.45	.562	.533	.501	.464	.420	.372	.318	.265	.219
1.50	.553	.524	.492	.455	.412	.364	.312	.260	.215
1.55	.544	.515	.483	.446	.403	.356	.305	.255	.211
1.60	.535	.506	.474	.437	.394	.348	.298	.249	.207
1.65	.527	.497	.465	.428	.385	.340	.292	.244	.203
1.70	.518	.489	.457	.420	.378	.333	.286	.240	.200
1.75	.511	.482	.450	.413	.371	.327	.281	.236	.197
1.80	.504	.475	.443	.406	.364	.321	.276	.232	.194
1.85	.496	.468	.436	.399	.358	.316	.272	.228	.191
1.90	.489	.460	.428	.392	.352	.310	.267	.225	.188
1.95	.482	.453	.421	.385	.345	.304	.262	.221	.185
2.00	.474	.445	.413	.377	.338	.298	.257	.217	.182
2.10	.459	.431	.339	.364	.325	.287	.248	.210	.176
2.20	.446	.417	.386	.352	.314	.276	.239	.203	.170
2.30	.433	.405	.374	.341	.304	.268	.232	.197	.166
2.40	.421	.393	.362	.330	.295	.260	.226	.192	.161
2.50	.409	.381	.351	.319	.285	.252	.219	.187	.157
2.60	.396	.369	.339	.308	.276	.243	.212	.181	.153
2.70	.384	.357	.328	.298	.266	.235	.205	.176	.148
2.80	.373	.347	.318	.289	.258	.228	.199	.171	.144
2.90	.363	.338	.310	.281	.251	.222	.193	.166	.140
3.00	.354	.329	.301	.273	.244	.216	.188	.162	.137
3.20	.336	.311	.285	.258	.231	.205	.179	.154	.131
3.40	.317	.294	.268	.243	.218	.193	.169	.146	.124
3.60	.299	.277	.253	.230	.206	.182	.160	.138	.117
3.80	.284	.263	.241	.218	.196	.174	.153	.132	.112
4.00	.271	.251	.229	.208	.187	.166	.146	.127	.107
4.50	.240	.222	.203	.184	.166	.148	.131	.114	.096
5.00	.212	.196	.179	.162	.146	.131	.116	.101	.086
5.50	.187	.173	.158	.143	.130	.116	.103	.090	.077
6.00	.166	.154	.141	.128	.116	.104	.093	.081	.069

Normalized Net Flux Function f(z,tau,al=0.4) at the Martian surface

Albedo 0.4									
Optical depth, τ	Zenith angle z, deg								
	0	5	10	15	20	25	30	35	40
0.10	0.596	0.595	0.594	0.593	0.592	0.591	0.590	0.589	0.588
.15	.592	.590	.590	.589	.588	.586	.585	.583	.582
.20	.587	.586	.585	.584	.583	.581	.579	.577	.575
.25	.583	.582	.581	.579	.578	.576	.574	.571	.569
.30	.578	.577	.576	.575	.573	.571	.568	.565	.562
.35	.574	.573	.572	.570	.568	.565	.563	.559	.556
.40	.569	.568	.567	.565	.563	.560	.557	.553	.549
.45	.565	.564	.563	.560	.558	.555	.552	.547	.542
.50	.560	.559	.558	.556	.553	.550	.546	.541	.535
.55	.555	.555	.553	.551	.548	.544	.540	.535	.529
.60	.550	.549	.548	.546	.543	.539	.534	.529	.522
.65	.545	.544	.543	.541	.538	.533	.528	.522	.516
.70	.540	.540	.538	.536	.532	.527	.522	.516	.509
.75	.535	.535	.533	.531	.527	.522	.516	.510	.503
.80	.531	.530	.528	.526	.522	.517	.511	.504	.496
.85	.526	.525	.523	.520	.517	.511	.505	.498	.490
.90	.521	.520	.518	.515	.511	.505	.499	.492	.483
.95	.516	.515	.514	.510	.506	.500	.494	.486	.476
1.00	.511	.511	.509	.506	.501	.495	.488	.480	.470
1.05	.506	.506	.504	.500	.496	.489	.482	.474	.464
1.10	.501	.501	.499	.495	.490	.483	.476	.468	.458
1.15	.497	.496	.494	.490	.485	.478	.471	.462	.452
1.20	.492	.491	.489	.485	.480	.473	.465	.456	.446
1.25	.487	.486	.484	.480	.475	.467	.460	.450	.439
1.30	.482	.481	.479	.475	.469	.462	.454	.445	.433
1.35	.477	.476	.474	.470	.464	.457	.449	.439	.428
1.40	.472	.471	.469	.465	.459	.452	.444	.434	.422
1.45	.467	.467	.465	.460	.455	.447	.438	.429	.417
1.50	.463	.462	.460	.456	.450	.442	.433	.423	.411
1.55	.458	.457	.455	.451	.445	.437	.428	.418	.406
1.60	.453	.452	.450	.446	.440	.432	.423	.413	.400
1.65	.449	.448	.445	.441	.435	.427	.418	.407	.395
1.70	.444	.443	.440	.436	.430	.422	.413	.402	.389
1.75	.440	.438	.435	.431	.425	.418	.408	.397	.384
1.80	.435	.434	.431	.427	.421	.413	.403	.392	.379
1.85	.431	.429	.427	.422	.416	.408	.398	.388	.375
1.90	.426	.425	.422	.417	.411	.403	.394	.383	.370
1.95	.422	.420	.418	.413	.406	.398	.389	.378	.365
2.00	.417	.416	.413	.408	.402	.394	.384	.373	.360
2.10	.408	.407	.404	.399	.393	.385	.375	.364	.350
2.20	.399	.398	.395	.391	.384	.376	.366	.355	.341
2.30	.391	.390	.387	.382	.376	.368	.358	.346	.332
2.40	.383	.382	.379	.374	.368	.359	.349	.338	.324
2.50	.375	.374	.371	.367	.360	.351	.341	.330	.316
2.60	.367	.365	.363	.358	.352	.343	.333	.321	.308
2.70	.358	.357	.354	.350	.343	.334	.324	.313	.299
2.80	.350	.349	.346	.342	.335	.326	.316	.305	.291
2.90	.343	.342	.339	.334	.328	.320	.310	.298	.284
3.00	.336	.335	.332	.327	.321	.313	.303	.291	.277
3.20	.322	.321	.318	.314	.307	.299	.289	.277	.264
3.40	.308	.307	.304	.300	.293	.285	.275	.264	.251
3.60	.294	.293	.290	.286	.280	.271	.262	.251	.238
3.80	.282	.281	.278	.274	.268	.260	.251	.239	.227
4.00	.271	.270	.267	.263	.257	.249	.240	.229	.217
4.50	.244	.243	.241	.237	.231	.224	.215	.205	.194
5.00	.219	.218	.216	.212	.207	.200	.192	.183	.173
5.50	.196	.196	.194	.190	.185	.179	.172	.163	.154
6.00	.176	.175	.173	.170	.166	.161	.154	.146	.137

Albedo 0.4									
Optical depth, τ	Zenith angle z, deg								
	45	50	55	60	65	70	75	80	85
0.10	0.586	0.583	0.579	0.575	0.568	0.558	0.540	0.509	0.430
.15	.579	.575	.569	.563	.553	.539	.514	.473	.382
.20	.571	.566	.559	.551	.538	.520	.490	.441	.344
.25	.564	.558	.549	.539	.524	.502	.467	.413	.316
.30	.557	.549	.539	.527	.509	.485	.447	.389	.295
.35	.549	.541	.529	.515	.496	.469	.428	.368	.278
.40	.542	.532	.519	.504	.483	.454	.411	.350	.264
.45	.534	.524	.510	.494	.471	.440	.394	.333	.252
.50	.526	.515	.501	.483	.459	.426	.379	.318	.242
.55	.519	.507	.491	.473	.448	.413	.365	.304	.233
.60	.512	.498	.482	.462	.437	.401	.352	.292	.225
.65	.505	.490	.473	.452	.427	.390	.340	.282	.219
.70	.498	.483	.465	.443	.417	.379	.329	.273	.213
.75	.491	.475	.456	.434	.407	.368	.318	.264	.207
.80	.483	.467	.448	.425	.397	.358	.308	.256	.202
.85	.476	.459	.440	.416	.389	.349	.300	.249	.198
.90	.470	.452	.432	.408	.380	.341	.292	.242	.193
.95	.463	.445	.424	.400	.371	.332	.283	.235	.189
1.00	.456	.438	.417	.392	.362	.323	.276	.228	.184
1.05	.450	.431	.410	.384	.354	.316	.270	.223	.180
1.10	.443	.424	.402	.377	.347	.309	.264	.219	.177
1.15	.437	.417	.396	.370	.339	.302	.258	.214	.174
1.20	.431	.411	.389	.363	.332	.295	.252	.209	.171
1.25	.424	.404	.382	.356	.324	.288	.246	.204	.167
1.30	.417	.398	.376	.349	.317	.281	.240	.200	.164
1.35	.412	.392	.370	.343	.311	.276	.236	.197	.162
1.40	.406	.386	.363	.337	.306	.271	.232	.193	.159
1.45	.400	.380	.357	.331	.300	.265	.227	.190	.157
1.50	.395	.374	.351	.325	.294	.260	.223	.186	.154
1.55	.389	.368	.346	.319	.288	.255	.219	.183	.152
1.60	.384	.363	.340	.313	.283	.250	.215	.180	.149
1.65	.378	.357	.334	.307	.277	.245	.211	.176	.147
1.70	.372	.352	.329	.302	.272	.240	.206	.173	.144
1.75	.367	.347	.324	.297	.267	.236	.203	.171	.142
1.80	.363	.342	.319	.292	.263	.232	.200	.168	.140
1.85	.358	.337	.314	.287	.258	.228	.197	.166	.138
1.90	.353	.332	.309	.283	.254	.224	.193	.163	.136
1.95	.348	.327	.304	.278	.250	.220	.190	.161	.134
2.00	.343	.322	.299	.273	.245	.217	.187	.158	.133
2.10	.333	.312	.289	.264	.237	.209	.181	.153	.129
2.20	.323	.303	.281	.256	.229	.202	.175	.149	.126
2.30	.315	.295	.273	.248	.222	.196	.170	.145	.122
2.40	.307	.287	.265	.241	.216	.191	.166	.142	.119
2.50	.299	.279	.257	.234	.209	.185	.161	.138	.116
2.60	.291	.271	.249	.227	.203	.179	.156	.134	.113
2.70	.283	.263	.242	.220	.197	.174	.151	.130	.110
2.80	.275	.255	.234	.213	.191	.169	.147	.127	.107
2.90	.268	.249	.228	.207	.186	.165	.144	.124	.104
3.00	.261	.243	.223	.202	.182	.161	.141	.121	.102
3.20	.249	.231	.211	.192	.172	.153	.134	.115	.097
3.40	.235	.218	.200	.181	.163	.145	.127	.110	.093
3.60	.223	.207	.189	.171	.154	.137	.121	.104	.089
3.80	.213	.197	.181	.164	.147	.131	.115	.100	.086
4.00	.204	.189	.173	.157	.141	.125	.110	.096	.082
4.50	.182	.168	.154	.140	.126	.112	.099	.087	.074
5.00	.161	.149	.136	.124	.113	.101	.090	.078	.066
5.50	.143	.133	.121	.110	.100	.091	.080	.070	.059
6.00	.128	.119	.109	.099	.090	.081	.072	.063	.054

Mars Temperature [33]

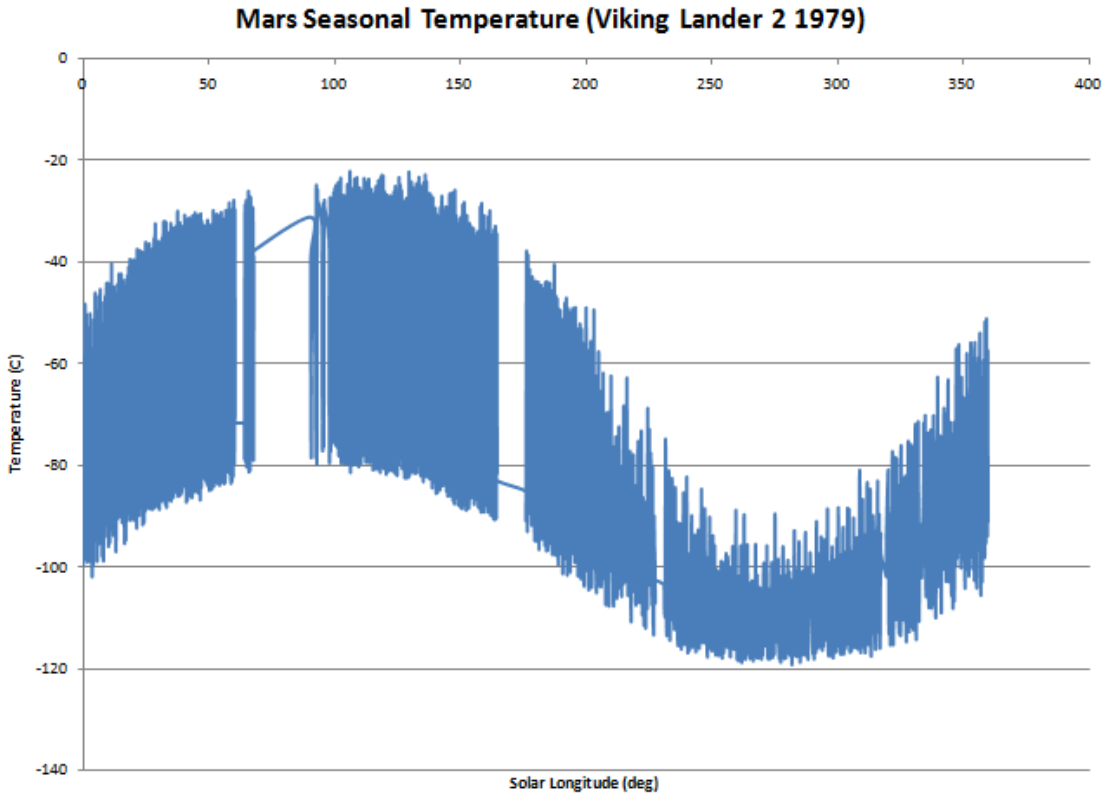

Appendix C

Irradiation Model in MapleSim

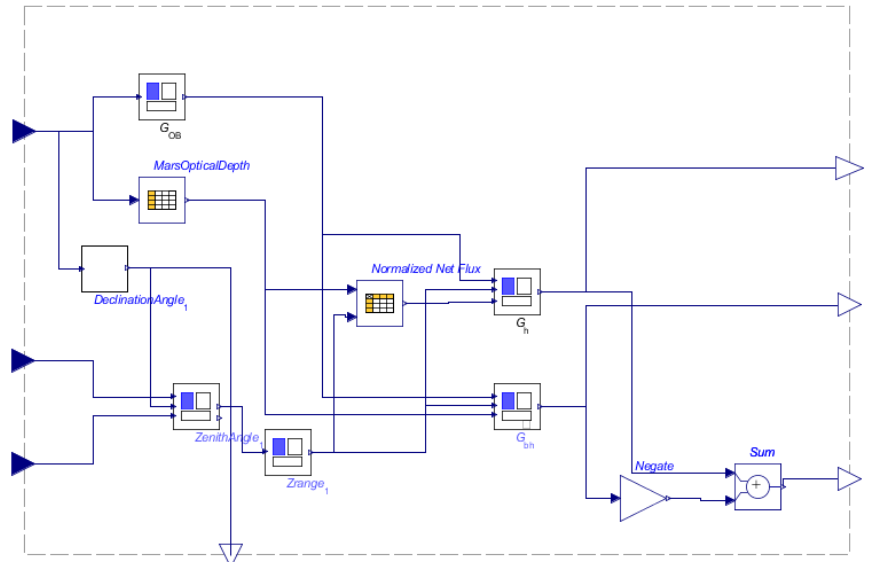

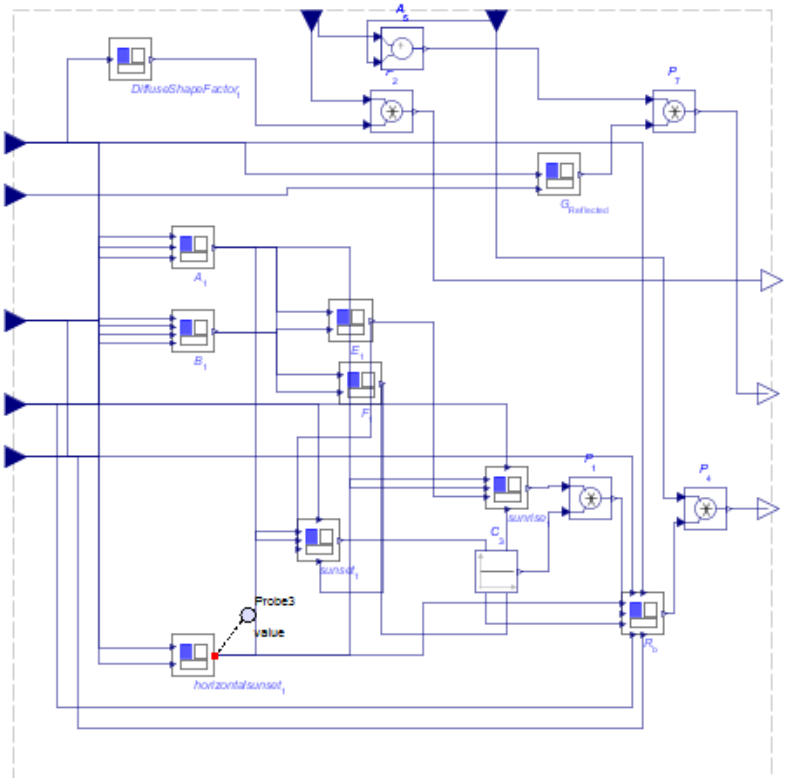

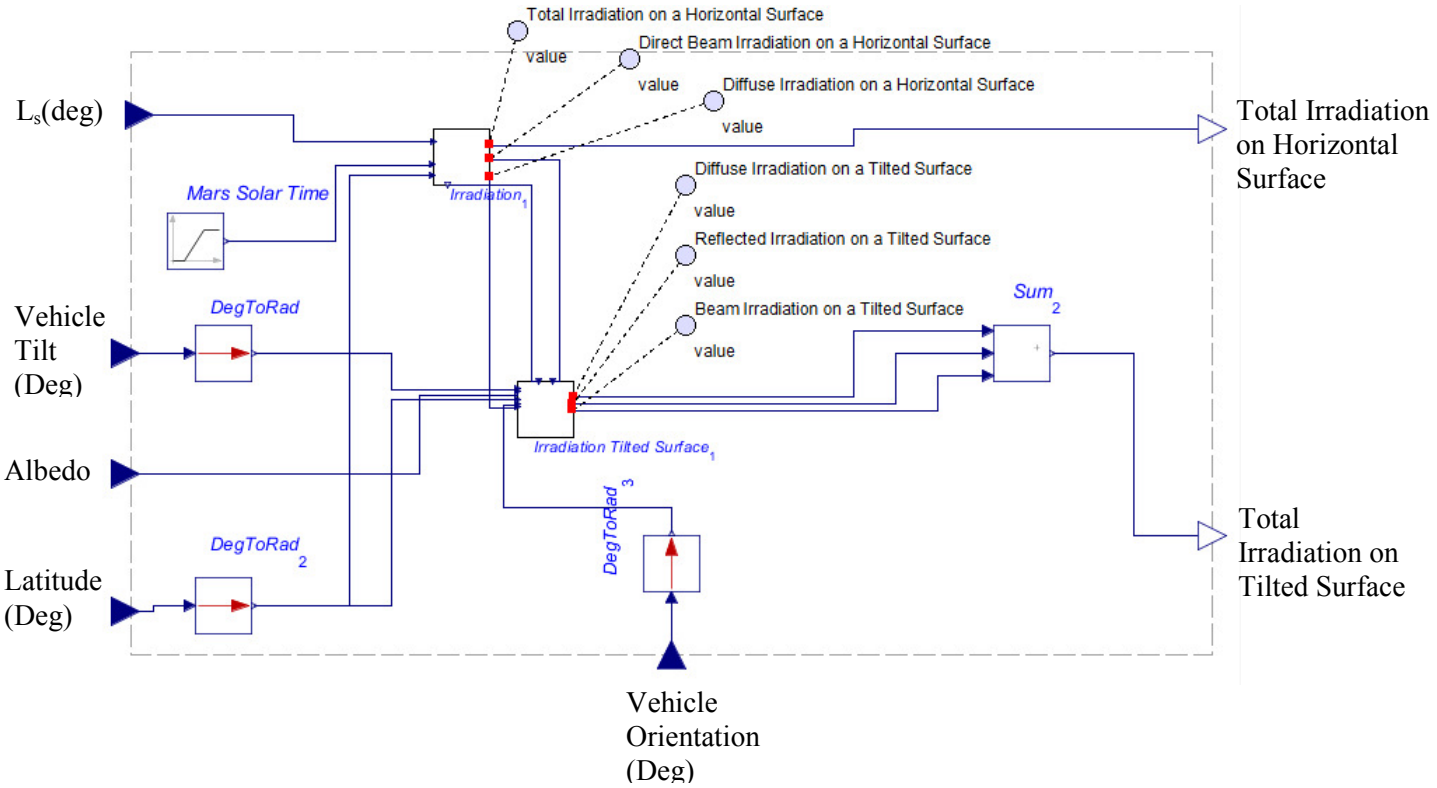
Total Irradiation on a Horizontal Surface
value
Direct Beam Irradiation on a Horizontal Surface
value
Diffuse Irradiation on a Horizontal Surface
value
Diffuse Irradiation on a Tilted Surface
value
Reflected Irradiation on a Tilted Surface
value
Beam Irradiation on a Tilted Surface
value
Irradiation1
Mars Solar Time
DegToRad
DegToRad2
DegToRad3
Irradiation Tilted Surface1
Sum2
Ls(deg)
Vehicle Tilt (Deg)
Albedo
Latitude (Deg)
Vehicle Orientation (Deg)
Total Irradiation on Horizontal Surface
Total Irradiation on Tilted Surface

Appendix D

HIL Input/Output Pin out

	Device Type	Physical Channel		Ch+	Ch-	A	B	Z	Ctr	GND	+5V	Connector Block	Terminal Configuration
Temperature	pXI 6229	PXI Slot 3	ai1	33	62							SCB-68 (A)	RSE
Irradiation	pXI 6229	PXI Slot 3	ai5	60	26					27		SCB-68(A)	Differential
Voltage 1 (Solar)	pXI 6229	PXI Slot 3	ai11	63						29	14	SCB-68(A)	RSE
Current 1 (Solar)	PXI 6259	PXI Slot 4	ai11	63						29	14	SCB-68(B)	RSE
Current 2 (Charge Controller)	PXI 6259	PXI Slot 4	ai2	65						32	14	SCB-68(B)	RSE
Voltage 2 (Charge Controller)	PXI 6259	PXI Slot 4	ai6	25						59	8	SCB-68(B)	RSE
Speed Control	PXI 6259	PXI Slot 4	ao0	22						55		SCB-68(B)	RSE
Lighting PWM 1	PXI 6229	PXI Slot 3	ctr0						2	35		SCB 68(A)	RSE
Lighting PWM 2	PXI 6229	PXI Slot 3	ctr0						2	36		SCB 68(A)	RSE
Lighting PWM 3	PXI 6229	PXI Slot 3	ctr0						2	35		SCB 68(A)	RSE
Lighting PWM 4	PXI 6229	PXI Slot 3	ctr0						2	36		SCB 68(A)	RSE
Angular Position	PXI 6259	PXI Slot 4	ctr1			42	46	41		7	8	SCB-68(B)	RSE
Voltage 3	PXI 6259	PXI Slot 4	ai0	68						67		SCB-68(B)	RSE
Current 3	PXI 6259	PXI Slot 4	ai 4	28						29		SCB-68(B)	RSE

Appendix E
Buckingham Pi Theorem

The Buckingham Pi Theorem states that every physically meaningful equation involving n parameters can be equivalently rewritten as an equation of Q_{pi} pi groups, where $Q_{pi} = n - m$, and m is the number of fundamental dimensions used [28]. The second part of the theorem shows how to find the pi groups which typically involves six steps:

1) List and count the n parameters involved in the problem. If any important parameters are missing, dimensional analysis will fail.
2) List the fundamental dimensions of each variable.
3) Find Q_{pi} and m where m is the number of dimensions and Q_{pi} is the number of pi groups to be formed, $Q_{pi} = n - m$.
4) Choose m scaling parameters that do not form a pi product. The scaling parameters should be selected with some generality because they will appear in every one of the pi groups.
5) Add one additional parameter to the m repeating parameters to form a power product. Algebraically find the exponents that make the product dimensionless. Do this sequentially, adding one new variable each time for Q times to form Q pi groups.
6) Write the final dimensionless function and check the terms to make sure all pi groups are dimensionless.

Appendix F

Scaling Pi Groups

$$\pi_1 = QV_{nom}{}^a R_{int}{}^b \tau^c$$

$$= [sA][m^2 kg s^{-3} A^{-1}]^a [m^2 kg s^{-3} A^{-2}]^b [s]^c$$

$$= [A]^{1-a-2b} [m^2 kg]^{a+b} [s]^{1-3a-3b+c}$$

$$\left(\begin{array}{ccc|c} -1 & -2 & 0 & -1 \\ 1 & 1 & 0 & 0 \\ -3 & -3 & 1 & -1 \end{array}\right)$$

$$a = -1\,, b = 1\,, c = -1$$

$$\pi_1 = \frac{QR_{int}}{V_{nom}\tau}$$

$$\pi_2 = V_{OC} V_{nom}{}^a R_{int}{}^b \tau^c$$

$$\left(\begin{array}{ccc|c} -1 & -2 & 0 & 1 \\ 1 & 1 & 0 & -1 \\ -3 & -3 & 1 & 3 \end{array}\right)$$

$$a = -1\,, b = 0\,, c = 0$$

$$\pi_2 = \frac{V_{OC}}{V_{nom}}$$

$$\pi_3 = IV_{nom}{}^a R_{int}{}^b \tau^c$$

$$\left(\begin{array}{ccc|c} -1 & -2 & 0 & -1 \\ 1 & 1 & 0 & 0 \\ -3 & -3 & 1 & 0 \end{array}\right)$$

$$a = -1\,, b = 1\,, c = 0$$

$$\pi_3 = \frac{IR_{int}}{V_{nom}}$$

$$\pi_4 = VV_{nom}{}^a R_{int}{}^b \tau^c$$

$$\left(\begin{array}{ccc|c} -1 & -2 & 0 & 1 \\ 1 & 1 & 0 & -1 \\ -3 & -3 & 1 & 3 \end{array}\right)$$

$$a = -1\,, b = 0\,, c = 0$$

$$\pi_3 = \frac{V}{V_{nom}}$$